N° d'ordre : 3677

THÈSE

PRÉSENTÉE A

L'UNIVERSITÉ BORDEAUX 1

ÉCOLE DOCTORALE DES SCIENCES DE LA VIE ET DE LA SANTÉ

par **KATIA WEHBE**

POUR OBTENIR LE GRADE DE

DOCTEUR

SPÉCIALITÉ : BIOLOGIE CELLULAIRE ET PHYSIOPATHOLOGIE

UTILISATION DE LA SPECTRO-IMAGERIE IR-TF POUR LE DÉVELOPPEMENT D'UNE ANATOMO-PATHOLOGIE MOLÉCULAIRE DES TUMEURS CÉRÉBRALES

Soutenue le 17 Novembre 2008

Après avis de :

M. Augusto Marcelli	Directeur de Recherche, INFN-LN Frascati	*Rapporteur*
M. Ganesh Sockalingum	Maître de Conférences, HDR, Université de Reims	*Rapporteur*

Devant la commission d'examen formée de :

M. Gérard Déléris	Professeur, Université Bordeaux 2	*Président*
M. Augusto Marcelli	Directeur de Recherche, INFN-LN Frascati	*Rapporteur*
M. Ganesh Sockalingum	Maître de Conférences, HDR, Université de Reims	*Rapporteur*
M. Bernard Desbat	Directeur de Recherche CNRS, Bordeaux	*Examinateur*
M. Michel Moenner	Professeur, Université Bordeaux 1	*Examinateur*
M. Cyril Petibois	Maître de Conférences, HDR, Université Bordeaux 2	*Directeur de thèse*

- 2008 -

N° d'ordre : 3677

THÈSE

PRÉSENTÉE A

L'UNIVERSITÉ BORDEAUX 1

ÉCOLE DOCTORALE DES SCIENCES DE LA VIE ET DE LA SANTÉ

par **KATIA WEHBE**

POUR OBTENIR LE GRADE DE

DOCTEUR

SPÉCIALITÉ : BIOLOGIE CELLULAIRE ET PHYSIOPATHOLOGIE

USAGE OF FTIR SPECTRO-IMAGING FOR THE DEVELOPMENT OF A MOLECULAR ANATOMO-PATHOLOGY OF CEREBRAL TUMORS

Soutenue le 17 Novembre 2008

Après avis de :

M. Augusto Marcelli	Directeur de Recherche, INFN-LN Frascati	*Rapporteur*
M. Ganesh Sockalingum	Maître de Conférences, HDR, Université de Reims	*Rapporteur*

Devant la commission d'examen formée de :

M. Gérard Déléris	Professeur, Université Bordeaux 2	*Président*
M. Augusto Marcelli	Directeur de Recherche, INFN-LN Frascati	*Rapporteur*
M. Ganesh Sockalingum	Maître de Conférences, HDR, Université de Reims	*Rapporteur*
M. Bernard Desbat	Directeur de Recherche CNRS, Bordeaux	*Examinateur*
M. Michel Moenner	Professeur, Université Bordeaux 1	*Examinateur*
M. Cyril Petibois	Maître de Conférences, HDR, Université Bordeaux 2	*Directeur de thèse*

- 2008 -

Dédicaces

A ma Mère et mon Père

Pour tous vos sacrifices, pour votre confiance et pour votre soutien que vous m'avez apporté depuis si longtemps, cette thèse est aussi la vôtre.

Avec mon plus grand respect et toute mon admiration

A ma Soeur et mes Frères

Pour votre présence, pour votre gentillesse et pour vos encouragements durant toutes ces longues années, cette thèse est aussi la vôtre.

Je serai toujours là pour vous

Je dédie cette thèse à ma famille et aux personnes

- ✓ *qui ont marqué ma vie d'une façon ou d'une autre,*
- ✓ *qui m'ont fait voir le bon côté des choses quand je ne voyais que le pire,*
- ✓ *qui m'ont fait sourire quand j'avais le plus besoin,*
- ✓ *et à qui je veux dire combien j'apprécie leur amitié*

Remerciements

Les travaux réalisés dans le cadre de cette thèse sous la direction du Docteur Cyril PETIBOIS, se sont déroulés au sein du Groupe de Chimie Bio-Organique de l'UMR 5084 du CNRS dirigé par le Professeur Gérard DELERIS. Ce laboratoire fait partie de l'unité de recherche de Chimie Nucléaire Analytique et Bio-environnementale, anciennement dirigée par Madame Monique SIMONOFF et actuellement par Monsieur Bernard LAVIELLE.

Je tiens tout d'abord à remercier profondément Madame M. SIMONOFF et Monsieur B. LAVIELLE de m'avoir accueillie chaleureusement au sein de l'unité.

Monsieur G. DELERIS, Professeur à l'Université Bordeaux 2, m'a accueillie dans son laboratoire en m'accordant sa confiance, son aide scientifique, son soutien et ses encouragements tout au long de ce travail. Je tiens donc à lui exprimer ma respectueuse reconnaissance pour m'avoir donné la chance de réaliser cette thèse et de m'avoir prodigué de précieux conseils durant ces trois années.

Je suis très reconnaissante à Monsieur C. PETIBOIS, Maître de Conférences à l'Université Bordeaux 2, pour avoir dirigé ce travail et pour m'avoir laissé une grande liberté d'opinion, d'expression et de décision dans la manière de mener ce travail aussi innovant que passionnant. Je le prie de bien vouloir trouver ici le témoignage de ma profonde gratitude pour cette grande confiance qui m'a permis d'acquérir l'autonomie nécessaire pour arriver à ce stade et sans laquelle aucun progrès n'est possible.

Je tiens à remercier chaleureusement Monsieur Michel MOENNER, Professeur à l'Université Bordeaux 1, pour sa précieuse collaboration, son implication et son aide pour la finalisation de ce projet. Ses encouragements, dans les pires moments de découragement, et son soutien ont été essentiels à l'aboutissement de ce travail. Pour tout cela et pour sa disponibilité dont il a fait preuve malgré son activité intense, je lui prie de croire ma respectueuse reconnaissance.

Je tiens à exprimer ma reconnaissance à Monsieur Augusto MARCELLI, Directeur de Recherche à INFN-LN Frascati, et à Monsieur Ganesh SOCKALINGUM, Maître de Conférences à l'Université de Reims, qui ont accepté la charge d'être rapporteurs et pour le temps consacré à l'évaluation de ce travail.

J'exprime également mes remerciements à Monsieur Bernard DESBAT, Directeur de Recherche au CNRS à Bordeaux, pour avoir accepté d'être membre de mon jury de thèse.

Je remercie également le Professeur Andréas BIKFALVI, Directeur de Recherche de l'unité INSERM U920 "Laboratoire des Mécanismes Moléculaires de l'Angiogenèse" de

m'avoir ouvert les portes de son laboratoire où j'ai pu effectuer tous les tests biologiques essentiels au déroulement de ce travail. J'associe à ces remerciements tous les membres de son laboratoire pour leur aide et leur sympathie, et en particulier Monsieur Raphael Pineau pour son aide technique.

Je tiens à exprimer ma sincère gratitude à l'équipe du service anatomo-pathologie au CHU Pellegrin, en particulier Madame le professeur Anne VITAL et Madame le Docteur Sandrine EIMER pour leur collaboration et leur aide pour les examens histopathologiques.

J'adresse également tous mes remerciements aux personnes que j'ai pu côtoyer et "tutoyer" pendant ces trois années au sein du laboratoire de Chimie Bio-Organique :

✓ *A tout le personnel, enseignants, chercheurs et ingénieurs pour leur soutien, leur encouragement, leur sympathie et leur bonne humeur : Karine, Sandra, Annie, Annie-Claude, Joe, Victor et Arnaud avec une attention particulière à Mireille pour ses précieux conseils.*

✓ *A tous les étudiants en Master et en Thèse pour avoir su conjuguer travail et bonne humeur au quotidien : Anne-Laure, Asma, Yan, Firmin, Seydou, Gilles, Stéphanie, Karima, Razia, Mous, Anis, et enfin mon ange gardien Sébastien. Bon courage et bonne continuation à tous.*

✓ *Ainsi que les anciens voisins : Sandra, Magali, Cyril, Jacques, Carlos, Mario et Nicolas.*

A tous ces gens je dis que je me rends compte combien d'amis j'ai pu me faire et avec qui j'ai partagé des moments de bonheur et des soirées de détente inoubliables. Que cette amitié perdure. Merci d'avoir toujours été là dans les bons et les mauvais moments.

J'exprime aussi mes remerciements à mes amis hors du laboratoire qui m'ont aussi encouragée et soutenue tout au long de ces années par leur présence et l'amitié qu'ils m'ont témoignées : Lara, Saloua, Marie-Paule, Marina, Mélanie, Emilie, Aleca, Sandrine, Alain et Moustapha.

Je voudrais enfin remercier très chaleureusement mes parents et ma famille pour leur confiance, leur soutien et leur considération, sans eux cette thèse ne serait pas. C'est grâce à leur amour et leur sacrifice que j'ai pu réaliser ce rêve. Aucun mot ne sera capable de transmettre tout ce que je leur dois. Que ce travail qui est le fruit de leurs encouragements soit une expression de ma plus grande affection envers eux.

Table of Contents

PART- II: RESULTS AND DISCUSSION

Glossary

Ang	Angiopoietin
ATP	Adenosine triphosphate
ATR	Attenuated total reflection
BBB	Blood brain barrier
BM	Basement membrane
BV	Blood vessel
CaF_2	Calcium Fluoride
CAM	Chorio-allantoïc membrane
CBO	Chimie Bio-Organique
CBO-P11	Vascular endothelial growth inhibitor cyclic peptide
CCD	Charge coupled device
CNS	Central nervous system
DMEM	Dulbecco's modified eagle medium
DNA	Deoxyribonucleic acid
DTGS	Deuterated triglycine sulfate
ECM	Extracellular matrix
ECs	Endothelial cells
EGF	Epidermal growth factor
EGFR	Epidermal growth factor receptor
EGM-2	Endothelial growth medium
FBS	Fetal bovine serum
FDG	Fluoro-deoxy-glucose
FGF	Fibroblast Growth Factor
FPA	Focal Plane Arrays
FT-IR	Fourier transform infrared
GB	Glioblastoma
GBM	Glioblastoma multiforme

Gd-DTPA	Gadolinium diethyltriamine pentaacetetic acid
GDMEC	Glioblastoma derived microvessel endothelial cells
H&E	Hematoxylin and eosin
HA	Hierarchical analysis
HCMEC	Human cerebral microvascular endothelial cells
HGF / SF	Hepatocyte growth factor / scatter factor
HIFs	Hypoxia-inducible factors
HSPG	Heparan Sulfate Proteoglycan
HUVEC	Human umbilical vein endothelial cells
IGF-1	Insulin-like growth factor
IHC	Immunohistochemistry
IL	Interleukine
IR	Infrared
IRTF	Infrarouge à Transformée de Fourier
KBr	Potassium Bromide
LA	Linear Arrays
MAP kinase	Mitogen activated protein kinase
MCs	Mural cells
MCT	Mercury cadmium telluride
MIR	Mid-infrared
MMPs	Matrix metalloproteinases
MRI	Magnetic resonance imaging
MVD	Microvessel density
PDGF	Platelet-derived growth factor
PDGFR-β	Platelet derived growth factor B receptor
PECAM	Platelet endothelial cell adhesion molecule
PET	Positron emission tomography
PF	Platelet factor
PF-4/CTF	C-terminal PF-4 fragment
PMT	Photomultiplier tube
RNA	Ribonucleic acid
RTKs	Receptor tyrosine kinases
S/N ratio	Signal/ noise ratio

Si	Silicon
SMCs	Smooth muscle cells
SPECT	Single Photon Emission Computed Tomography
TGF-β1	Transforming Growth Factor-β1
TNF-α	Tumor necrosis factor-α
UV	Ultraviolet
VBM	Vascular basement membrane
VEGF	Vascular endothelial growth factor
VEGFR	Vascular endothelial growth factor receptor
Vis	Visible
VSMCs	Vascular smooth muscle cells
WHO	World Health Organization
ZnSe	Zinc Selenide
α-SMA	α-smooth muscle actin


Introduction

Introduction
(Français)

Les travaux de recherche réunis dans cette thèse de doctorat ont été effectués dans l'unité de recherche de Chimie Nucléaire Analytique et Bio-environnementale UMR CNRS 5084 CNAB, et plus particulièrement au sein du Groupe de Chimie Bio-organique situé sur le campus de l'université *Victor Segalen* Bordeaux 2. Les trois thèmes essentiels de recherche de cette unité sont : Chimie pour le Vivant, Cosmochimie/Géochimie Environnementale, et Environnement/Chimie Nucléaire. L'équipe de Chimie Bio-organique conçoit et applique de nouveaux outils chimiques pour aborder l'imagerie cellulaire et tissulaire (analyses par spectro-imagerie Infrarouge et par faisceaux d'ions), et la synthèse de molécules permettant le ciblage biologique. Un processus biologique est plus particulièrement privilégié, l'angiogenèse qui est capitale pour le développement des tumeurs solides tels les gliomes.

Les gliomes sont les tumeurs cérébrales primaires les plus fréquentes, classifiées en quatre grades cliniques (I à IV, selon l'OMS). Cette classification histologique est basée sur des critères de densité cellulaire, d'atypies nucléaires, de mitose, de prolifération microvasculaire et de nécrose. Les gliomes de grade I correspondent essentiellement à l'astrocytome pilocytique, circonscrit, bénin. Les gliomes infiltrants sont de bas grade (II) ou de haut grade (III ou IV). Les astrocytomes de grade IV, appelés glioblastomes multiformes (GBM), forment des tumeurs richement vascularisées, plus agressives et présentant une organisation hétérogène avec des zones nécrotiques et hémorragiques. En plus de leur dimension réduite, de quelques mm^3 en général, leur forte propension infiltrante rend difficile l'exérèse complète de la tumeur. D'ailleurs, les solutions d'imagerie actuellement utilisées en clinique souffrent d'une sensibilité et/ou d'une résolution trop faibles pour espérer en délimiter les contours exacts. Un examen anatomopathologique est donc nécessaire mais il ne repose actuellement que sur l'étude visuelle des coupes histologiques de la tumeur et donc sur l'expérience des

praticiens. 20 à 30% des analyses extemporanées de glioblastomes restent ainsi sans résultat pour le neurochirurgien, ce qui limite fortement la prise en charge des patients.

Nous proposons donc d'utiliser la spectro-imagerie Infrarouge à Transformée de Fourier (IRTF) comme une imagerie fonctionnelle permettant de déterminer des marqueurs chimiques de la progression tumorale, la finalité étant d'en faire une aide au diagnostic. Cette technique apporte une information moléculaire globale des contenus d'un échantillon avec une résolution par pixel de l'image visible de 6*6 µm environ, ce qui en fait une modalité d'imagerie *ex vivo* très performante et à même d'améliorer l'examen pathologique des tumeurs. Nos travaux ont été basés sur la recherche de paramètres moléculaires permettant de discriminer les vaisseaux sanguins sains et tumoraux, notamment sur la base des contenus moléculaires de leur membrane basale, laquelle subit des altérations liées aux facteurs angiogéniques de la tumeur.

La première partie de ce travail de recherche est une synthèse bibliographique sur la pathophysiologie des gliomes, l'angiogenèse physiologique et pathologique et le rôle de l'angiogenèse dans les gliomes. Les moyens analytiques actuels sont ensuite abordés, plus particulièrement pour ce qui concerne les différentes techniques d'imagerie, et l'exposé bibliographique se termine sur la place que pourrait y prendre la spectro-imagerie IRTF. La seconde partie du document est consacrée aux différents résultats obtenus lors de ce travail qui sont présentés sous la forme de trois articles et deux rapports d'activités, et sont discutés globalement dans une conclusion générale. Nous avions tout d'abord utilisé la spectroscopie IRTF pour déterminer les différences de structure secondaire entre les collagènes des types I et IV, qui sont les principaux constituants des membranes basales des capillaires sanguins. Nous avons ensuite voulu vérifier si ces différences de structure secondaire pouvaient être utilisées pour discriminer les capillaires sanguins sains et tumoraux, aussi bien sur modèles animaux que sur des gliomes humains. Nos résultats ont alors été comparés à ceux de l'immunohistochimie utilisée lors de l'examen anatomopathologique. D'autres marqueurs spectraux ont aussi été envisagés, concernant notamment les contenus lipidiques et glucidiques des cellules de la membrane vasculaire, pericytes et cellules endothéliales.

Introduction
(English)

This work was conducted in the research unit of “Chimie Nucléaire Analytique et Bio-environnementale” UMR CNRS 5084 CNAB, in particularly within the Bio-organic Chemistry Group situated at the campus of the University of *Victor Segalen* Bordeaux 2. The three main themes of this research unit are: Chemistry in Life Science, Cosmochemistry/Environmental Geochemistry, and Environment/ Nuclear Chemistry. The Bio-organic Chemistry team designs and implements new chemical tools addressed to the cell and tissue imaging (analyses by Infrared spectro-imaging and ion beams), and to the synthesis of molecules for biological targeting. A biological process is particularly privileged, angiogenesis, which is vital for the development of solid tumors such as gliomas.

Gliomas, the most frequent primary brain tumors, are classified according to the World Health Organization (WHO) classification into four grades with increasing malignancy: pilocytic astrocytoma (grade I), diffuse astrocytoma (grade II), anaplastic astrocytoma (grade III), and glioblastoma multiforme (grade IV). The histological classification is based on some criteria such as: cellular density, nuclear atypia, mitotic activity, necrosis and microvascular proliferation. Glioblastoma multiforme (GBM) are the most aggressive and present a high heterogeneity with hemorrhagic and necrotic areas. Besides their small size, generally a few mm^3, their high degree of infiltration and invasiveness makes it difficult to complete excision of the tumor. Moreover, the current imaging techniques used clinically suffer from a sensitivity and / or resolution too much weak to expect defining the tumor margins. A classical pathological examination is thus necessary but it is currently based on the visual study of histological sections of the tumor and therefore the experience of pathologists. As a consequence, 20 to 30% of extemporaneous analyses of glioblastomas are not sufficiently informative and remain without result for the neurosurgeon, which severely limits the care of patients.

In this project we have proposed the use of Fourier Transform Infrared (FTIR) spectro-imaging as a functional imaging to identify chemical markers of tumor progression in order to help neurosurgeons in the diagnosis during surgery. This technique provides comprehensive molecular information of sample content with a resolution per image pixel of 6*6 µm approximately, making it a powerful modality of *ex vivo* imaging which may be able to improve the pathological examination of tumors. Our work was based on research of molecular parameters to discriminate between healthy and tumor blood vessels, especially on the molecular basis of the contents of their basement membrane, which undergoes alterations related to angiogenic factors of the tumor.

In the first part of this study, the statement literature addresses generalities on gliomas, the physiological and pathological angiogenesis and the role of angiogenesis in gliomas. Then, the current analytical techniques are discussed, especially for the various imaging techniques to end with FTIR spectro-imaging. The second part is devoted to the different results of this work which are presented in the form of three publications and two research reports, and are globally discussed in a general conclusion. First, we used the FTIR spectroscopy to determine the differences between the secondary structure of types I and IV collagen, which are the main constituents of basal membranes of capillary blood vessels. We then wanted to check whether these differences in secondary structure could be used to discriminate between healthy and tumor capillary blood vessels, in animal models as well as in human gliomas. Our results were then compared with those of the immunohistochemistry used in the pathological examination. Other spectral markers were also considered, including fat and carbohydrate contents of cell vascular membrane, pericytes and endothelial cells.

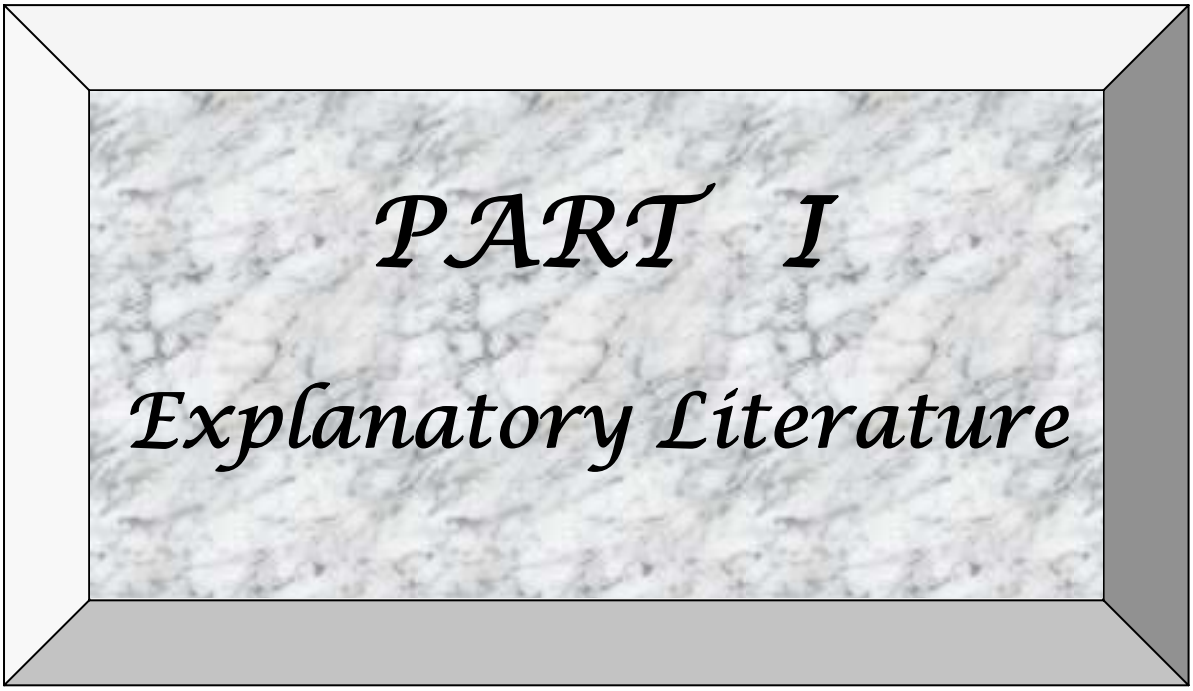
PART I
Explanatory Literature

Chapter I

Gliomas and Angiogenesis

Gliomas and Angiogenesis

I – GLIOMAS

I.1. Generalities

Tumors of the central nervous system (CNS) have specific criteria that make them different from other neoplasms in the body. We can cite: the distinction between benign and malignant tumors which is less evident in the CNS; and that they rarely metastasize outside the CNS, although their infiltration into the surrounding brain parenchyma. The incidence of intracranial neoplasms is ~10–20 per 100,000, and they account for ~2% of deaths in Western countries. In adults, 50% of the brain tumors are primary and the other 50% are metastatic, also called secondary brain tumors. The majority of these tumors appear after the fifth decade of life, and they are slightly predominant (55%) in males with the exception of meningiomas, which are twice as common in females [1].

I.2. Classification

Primary brain tumors are classified according to their predominant cell type. Tumors arising from glial cells, called gliomas, represent the most common group of primary brain tumors, and are among the two most lethal cancers for the human body with pancreatic tumors. They are classified by their cell type, their grade, and their location. The main types of gliomas are ependymomas (ependymal cells), astrocytomas (astrocytes), and oligodendrogliomas (oligodendrocytes). Four malignancy grades are recognized by the World Health Organization (WHO) grading system, with grade I tumors being the least aggressive and grade IV the most aggressive tumors. Astrocytic tumors are classified into pilocytic astrocytomas (grade I), diffuse or low-grade astrocytomas (grade II), anaplastic astrocytomas (grade III), and glioblastomas (grade IV). Grade I astrocytomas are most commonly seen in children and are not considered to be malignant. To the opposite, grades II to IV

tumors are malignant. More than 50% of the primary neoplasms are gliomas and 65% of these gliomas are the most malignant variety, glioblastoma (GB) [1-3].

I.3. Etiology and Clinical presentation

The etiology of primary brain tumors is unknown and data on risk factors is unclear. Several molecular mechanisms may be involved in the development of gliomas and their progression to more malignant tumors. The progression to high grade glioma is associated with inactivation of the p53 tumor suppressor gene, as well as with the over expression of many growth factors such as platelet-derived growth factor (PDGF), epidermal growth factor receptor (EGFR) gene, and also angiogenic factors such as vascular endothelial growth factor (VEGF) [1, 4].

The clinical presentation of brain tumors depends on the location of the tumor. Patients may present symptoms either due to focal tissue destruction or because of edema and raised intracranial pressure. Brain gliomas can cause headaches, nausea and vomiting, epilepsy, and intracranial pressure. Glioma of the optic nerve may cause visual loss. Glioblastoma is usually centered in the deep white matter of the cerebral hemispheres, most frequently in the frontal lobe. The frontal lobe tumors commonly manifest with mental and personality changes as an early symptom [1, 5].

I.4. Prognosis and survival

The infiltrating adult astrocytic tumors occur commonly in the cerebral hemispheres. The diffuse astrocytomas have a peak incidence between 25 and 50 years, the glioblastomas have a peak incidence between 45 and 70 years, while the peak incidence for the anaplastic astrocytomas is in between, around the age of 45. Survival is generally related to tumor histopathology, anatomic location, and age of patient. Patients with grade II tumors typically survive more than 5 years [1, 5]. The median survival of patients with anaplastic astrocytomas (grade III) is about 2–3 years after surgery. If the recurrent anaplastic astrocytoma is subjected to a second surgery, more than 50% of cases will show glioblastoma. Glioblastomas may develop de novo (primary glioblastoma) or through progression from the low-grade or anaplastic astrocytomas (secondary glioblastoma) [2, 3, 6]. Glioblastomas are highly

invasive, very aggressive, and often infiltrate critical neurological areas within the brain, thus their prognosis is very poor. The mean survival time after diagnosis of GB has remained unchanged during the last few decades, in spite of advances in surgical techniques, radiotherapy, and also chemotherapy; patients' survival still ranges from 9 to 12 months after initial diagnosis [1, 5, 7].

I.5. Diagnostic tools

While a careful history and physical examination are the first step in diagnosis of gliomas, imaging is the next important step. However, the management of gliomas is still a challenging task because current imaging techniques do not always differentiate them from non-tumoral lesions (such as inflammation) or high grade tumors from low grade lesions. Imaging techniques, such as magnetic resonance imaging (MRI), positron emission tomography (PET), and Single Photon Emission Computed Tomography (SPECT) used for the diagnosis of malignant gliomas have their limitations.

Although MRI is the imaging modality of choice for brain tumors and has improved visualization of these tumors, there are a number of areas where it fails to provide sufficient information. Some of these areas are: the inability of this conventional imaging to show tumor infiltration, the deficient classification of tumor grading, and insensitivity to detect subtle changes in tumors due to the effects of treatment. MRI has a spatial resolution between 0.5 and 1.5 mm. The most widely used contrast agent for MRI is Gadolinium diethyltriamine pentaacetetic acid (Gd-DTPA). Because Gd-DTPA leaves the vasculature and rapidly extravasates into the tissue, the changes in signal intensity do not adequately reflect tumor perfusion [8-10].

PET has a spatial resolution limited to 3-4 mm. PET uses positron-emitting radionucleides to label molecules, which can then be imaged inside the body. Although its spatial resolution is lower than that of MRI, it has better specificity and sensitivity in the field of *in vivo* imaging modalities. Fluoro-deoxy-glucose (FDG) labeled with the positron emitter ^{18}F (half life of 110 minutes) can be used to localize

primary tumors. SPECT (with a resolution of 5-6 mm) is another nuclear imaging modality sensitive to very low concentrations of tracer molecules, although one order of magnitude less sensitive than PET. However, the radionucleides used for SPECT are easier to prepare and present longer periods than those used for PET (e.g. 13.2 hours for ^{123}I) [10-13].

If diagnosis is unsuccessful by using *in vivo* imaging techniques, biopsies are necessarily performed to provide more information. Stereotactic biopsy is one of the safest methods [14]. Furthermore, during brain tumor surgery, since imaging modalities are not sufficiently efficient for determining the tumor margin accurately, rapid assessment of cryostat sections of biopsies are performed to obtain pathological diagnoses and to help determining tumor margins. Microscopic examination relies on these histological tissue sections from tumor biopsies to identify the morphological aspects in gliomas and to help determine the grade of the tumor which is not evident in most of cases. *(Microscopic techniques will be further detailed in section IV)*. Moereover, cytotoxic or radiation therapy prior to histological diagnosis may make classification and malignancy grading extremely difficult or impossible.

I.6. Treatments

Surgery, radiotherapy and chemotherapy are the main treatments for malignant or high grade gliomas but they are limited for many reasons. Even when treated with combined surgery, chemotherapy, and radiotherapy, patients with high-grade malignant glioma present cancer recurrence between 6 and 12 months, and for anaplastic astrocytoma between 18 and 36 months. Surgery involves removing as much of the glioma as possible, while trying to minimize damage to healthy tissue. Several reports have assessed the effect of surgery on survival, showing that to a more extensive resection was associated a longer survival. However, glioblastoma tumors can be difficult to resect due to the lack of a defined tumor edge as the tumor may extend into normal brain tissue. It is thought that even a partial resection is beneficial to the patient, as it improves body functions and diminishes the pressure in the brain. The goal is to maximize tumor removal and, where possible, remove a margin of surrounding brain without removing tissue that would cause a new deficit

[1, 14]. External beam radiation is often administered after surgery to destroy any remaining tumor cells, but unfortunately this exposes the healthy brain tissue to damage. Chemotherapy may not be efficient because of the high heterogeneity of these tumors which may have more than one kind of cells. Moreover, the effectiveness of chemotherapy critically depends upon the successful transvascular delivery of small and large molecules through the blood brain barrier.

I.7. Notions on the blood brain barrier

The blood brain barrier (BBB) separates the brain from blood to help regulating brain functions and metabolism. It is composed of continuous tight junctions of endothelial cells lining blood vessels in the brain and forms a barrier between the circulation and the brain parenchyma (astrocytes, microglia) ***(Figure 1)***. A basement membrane composed of proteins, surrounds the endothelial cells and associated pericytes, and provides mechanical support and a barrier function. This physical barrier restricts the passage of various chemical substances and protects the brain from bacterial infections. BBB is less intact in brain tumors compared with the normal brain vasculature. BBB at sites of tumor undergoes alterations such as increased level of permeability. *(More details in section III paragraph III.1.1).*

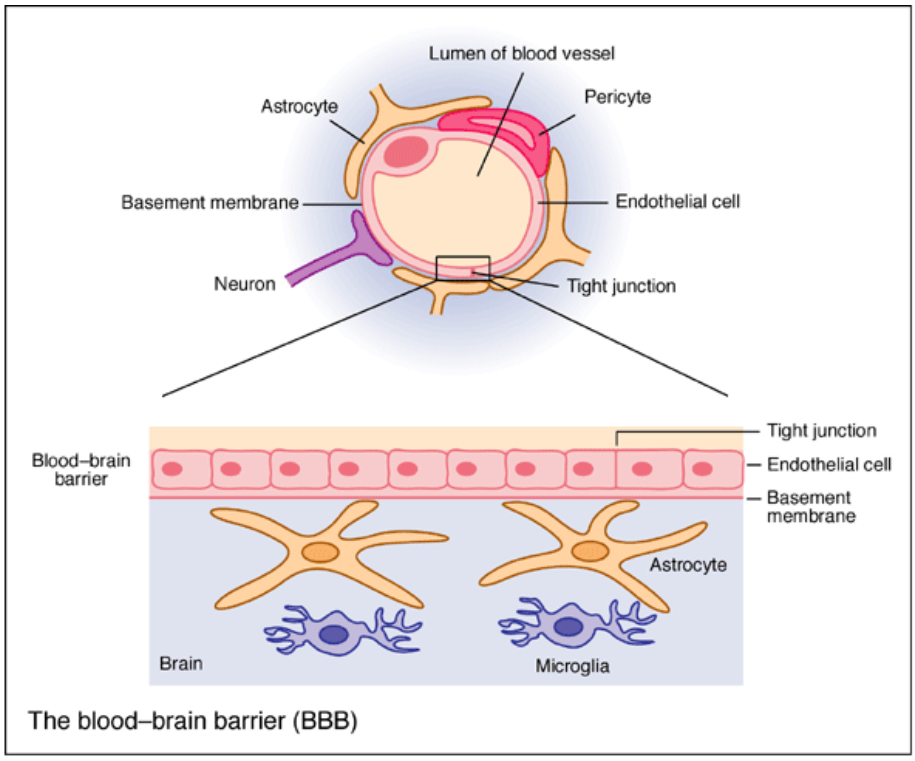

Figure 1. The blood brain barrier (BBB). (Modified, based on Francis et al 2003) [15] .

I.8. The vascular microenvironment in gliomas

Like any other neoplasic tissue, gliomas are constituted of three compartments, classified as cellular, interstitial, and vascular in nature. Normal brain vasculature is highly specialized. It is composed of three cell types: endothelial cells, pericytes, and astrocytes ***(Figure 2)*** [16].

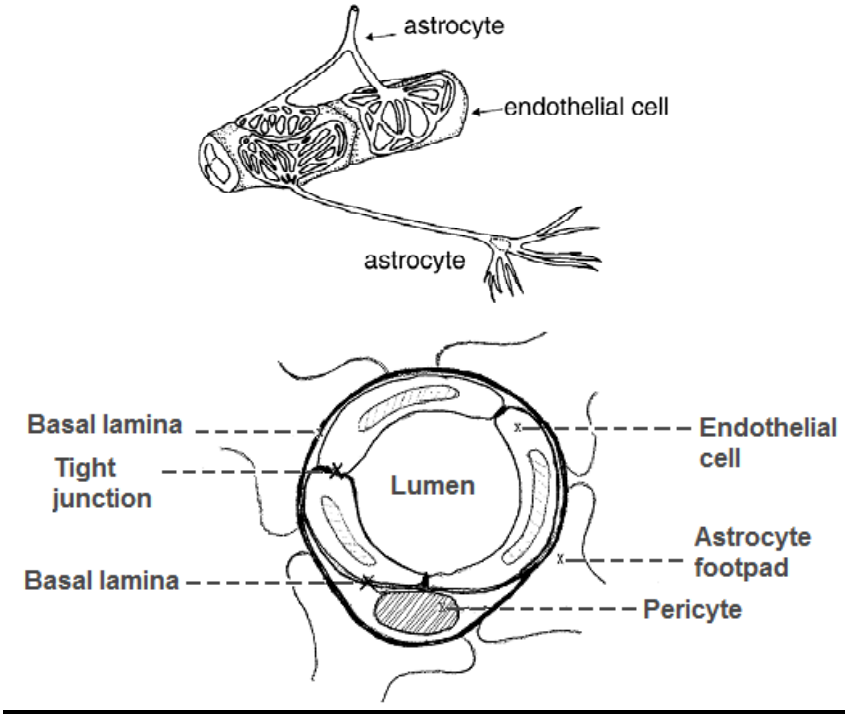

Figure 2. A global view and a cross section of a CNS blood vessel. The pericyte is located at the abluminal side of the microvessel. A duplicature of the basement membrane (BM) separates the pericyte from the endothelial cell and the astrocyte footpads. (Based on Kacem et al. 1998 [17] and Balabanov et al. 1998 [18])

The microvascular micro-environment determines the pathophysiological characteristics of gliomas, such as edema formation, tumor cell invasiveness, or selective permeability for large molecules. Clinically, the vascular microenvironment in gliomas is of diagnostic, therapeutic, and prognostic significance. Today, the radiological diagnosis and detection of gliomas is primarily based on its vascularity and permeability. Since the tumor causes alterations in tight junctions, BBB in tumor sites has higher permeability than into the normal brain tissue. As a consequence, endothelial cells, pericytes, and the basement membrane of tumor vessels reveal significant abnormalities when compared to cerebral vessels [1, 19].

II – ANGIOGENESIS

II.1. Angiogenesis and vasculogenesis

II.1.1. Blood vessel formation

Growth of a vascular system is one of the earliest events in organogenesis. Development of new blood vessels occurs during embryonic development and during normal and pathologic periods of tissue growth. New vessels can form via distinct processes, namely vasculogenesis and angiogenesis. Angiogenesis, defined as the development of new blood vessels from preexisting vascular network, is one of several mechanisms that build and maintain the blood supply in the body's tissues. As such, it can be distinguished from arteriogenesis and vasculogenesis. Arteriogenesis is a repair mechanism whereby bridging collateral arterioles are remodeled and grow to compensate for arterial occlusions in major vessels [20-23].

Vasculogenesis, which involves the differentiation of vascular cells from undifferentiated precursors, forms the initial vascular network during early embryonic development and contributes to the vascularization of tissues. In this process, mesodermal cells differentiate into angioblasts which then give rise to the endothelial cells assembling into a first vascular network. Because vasculogenesis only leads to an immature, poorly functional vasculature in the embryo, angiogenesis is essential for the subsequent development of the vascular network of arteries, veins, arterioles, venules and capillary blood vessels ***(Figure 3)*** [22, 24].

During the angiogenesis phase, the vascular plexus progressively expands by means of vessel sprouting and remodels into a highly organized and stereotyped vascular network of larger vessels ramifying into smaller ones [25]. Angiogenesis is responsible for the vascularization in the embryo and growing tissues. This process is generally suppressed in healthy adult organisms and is turned on temporarily in settings such as the female reproduction cycle (ovarian and uterine cycles) or during tissue repair processes (wound healing and restoration of capillary blood network into injured tissues) [26]. Otherwise, while angiogenesis is essentially a rare event in the

adult, it can occur in a number of relevant pathologies, such as cancer, various retinopathies, blinding ocular disorders, rheumatoid arthritis, psoriasis [20, 22].

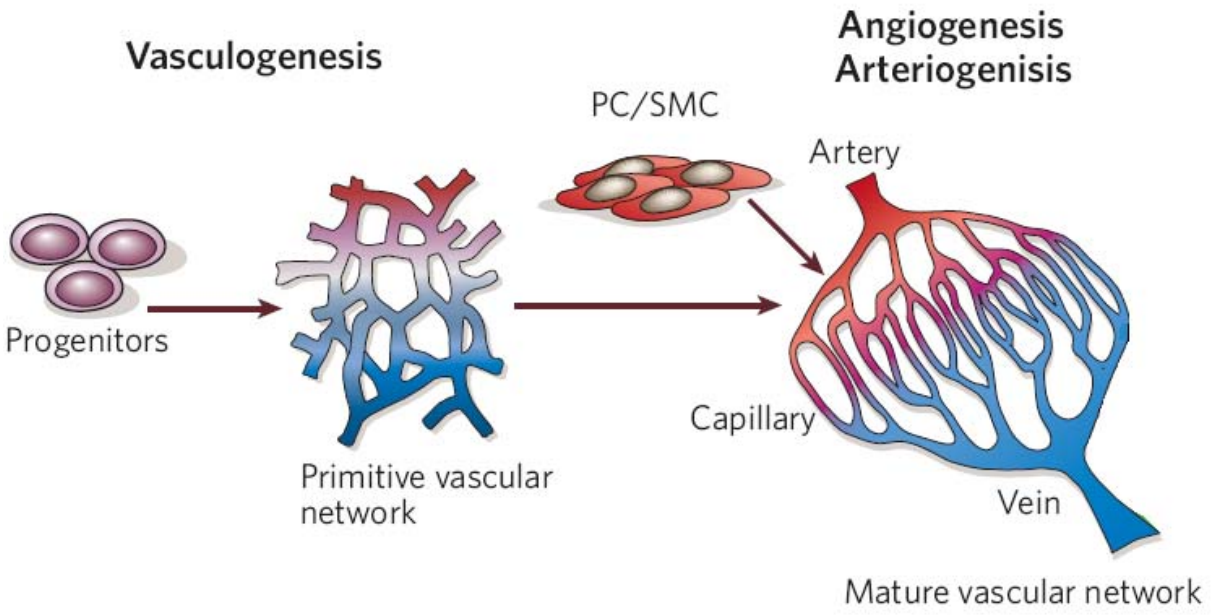

Figure 3. Formation of blood vessels. Development of the vascular systems: during vasculogenesis, endothelial progenitors give rise to a primitive vascular labyrinth of arteries and veins; during subsequent angiogenesis, the network expands, pericytes (PC) and smooth muscle cells (SMC) cover nascent endothelial channels, and a an organized vascular network emerges. (Modified based on Carmeliet 2005) [25].

II.1.2. Maturation of vasculature

The maturation of nascent vasculature, formed by vasculogenesis or angiogenesis, requires recruitment of mural cells (pericytes in medium-sized and vascular smooth muscle cells in larger vessels), generation of an extracellular matrix, and specialization of the vessel wall for structural support and regulation of vessel function. The vascular network is spatially organized to provide adequate oxygen and nutrients to the cells of all organs. The walls of vessels are composed of endothelial cells (ECs) and mural cells (MCs), which are embedded in an extracellular matrix (ECM) ***(Figure 4)*** [21, 27]. The origin, number, type and organization of mural cells, the composition of the associated matrix, and the connection between the vascular system and the nervous system depend on the location of the vessel and its function. This is called organ-specific specialization of vessel wall (such as inter endothelial

junctions, fenestrations, apical-basal polarity, surface receptors and foot processes) [27].

Capillaries are tubes formed by endothelial cells, which are supported by vascular pericytes and a basement membrane. Arteries and veins are tubes that consist of multiple layers: first, the intima, which is composed of ECs, pericytes and a basement membrane; second, the media, which is composed principally of smooth muscle cells and their ECM; and third, in the largest vessels, the adventitia, which is composed principally of fibroblasts and their ECM [23].

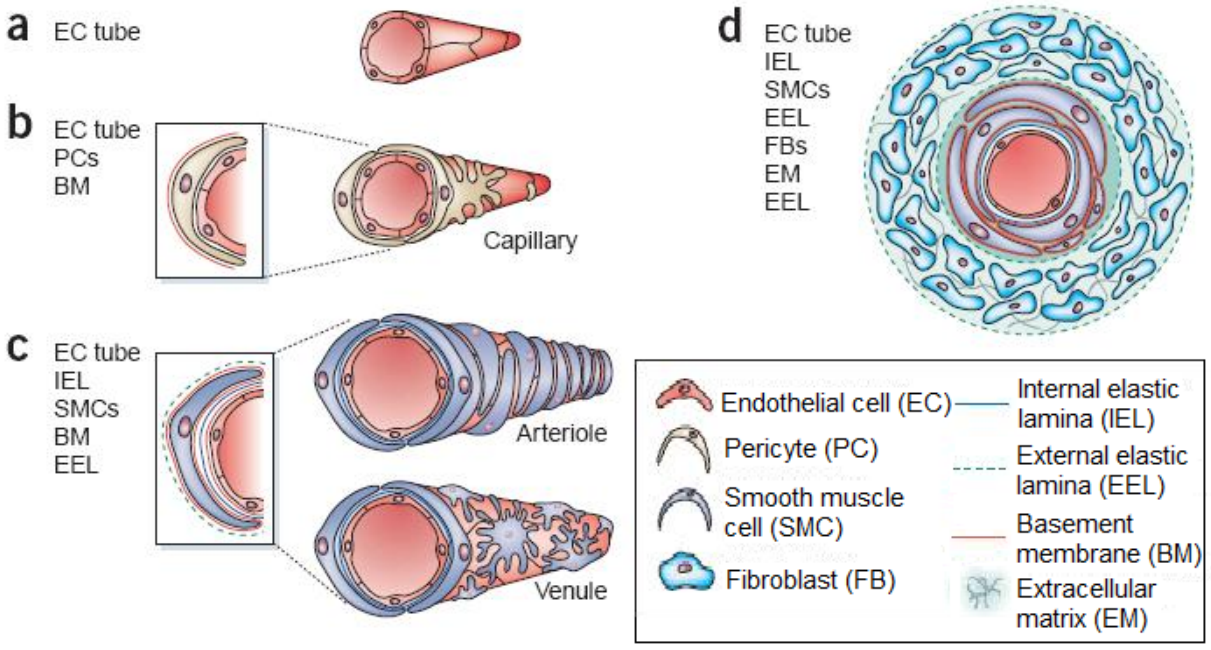

Figure 4. Wall composition of nascent versus mature vessels. (a) Nascent vessels consist of a tube of ECs. These mature into the specialized structures of capillaries, arteries and veins. **(b)** Capillaries, the most abundant vessels in our body, consist of ECs surrounded by basement membrane and a sparse layer of pericytes embedded within the EC basement membrane. Depending upon the organ or tissue, the capillary endothelial layer is continuous (as in muscle), fenestrated (as in kidney or endocrine glands) or discontinuous (as in liver sinusoids). The endothelia of the blood-brain barrier are further specialized to include tight junctions, and are thus impermeable to various molecules. **(c)** Arterioles and venules have an increased coverage of mural cells compared with capillaries. **(d)** The walls of larger vessels consist of three specialized layers: an intima composed of endothelial cells, a media of SMCs and an adventitia of fibroblasts, together with matrix and elastic lamina. (Modified, based on Jain 2003) [27].

II.2. Angiogenesis process

Angiogenesis involves a variety of coordinated events, including: 1- production and release of angiogenic factors, 2- proteolytic degradation of the extracellular matrix surrounding the parent vessel, 3- migration and proliferation of the endothelial cells and mural cells to assemble the new vessel, 4- lumen formation, and 5- construction of the mural cell layer of the vessel wall with associated pericytes and/or smooth muscle cells. Angiogenesis is regulated by multiple stimulatory and inhibitory factors that are able to modulate the migration and/or proliferation of microvascular cells. Of the angiogenic factors, Vascular Endothelial Growth Factor (VEGF) and Fibroblast Growth Factors (FGF-1 and FGF-2) have been studied the most intensively. The mitogenic activity of VEGF has been shown to be restricted to ECs, while FGF is mitogenic for a spectrum of cells, including vascular smooth muscle cells (VSMCs) and ECs. The VEGF expression appears to be upregulated by hypoxia [20, 28].

II.2.1. Endothelial cell functions relating to angiogenesis

Endothelial cells are the primary physical barrier in microvessels for delimitating between blood and tissue. As stated before, many endothelial cell functions are required for angiogenesis, including matrix degradation, migration, proliferation, and morphogenesis.

a. Matrix degradation

Vessel sprouting requires both the degradation of the laminin-rich basement membrane surrounding the endothelial cells and the proteolysis of the collagen-rich extracellular matrix of the surrounding connective tissue. Matrix degradation can facilitate angiogenesis by activating angiogenic proteins or releasing matrix- or membrane-bound growth factors. This process can also release anti-angiogenic matrix fragments, including endostatin, angiostatin, and tumstatin. Families of proteases responsible for matrix degradation during angiogenesis include matrix metalloproteinases (MMPs), serine proteinases (plasminogen activators), cathepsins, and aminopeptidases. Of these, the MMPs are most frequently assessed as

contributors to angiogenesis. Upon activation, MMPs digest matrix components such as collagen, fibrin, laminin, and fibronectin [28-31].

b. Migration

Following matrix degradation, ECs migrate into the surrounding tissue in response to angiogenic growth factors (VEGF) and chemokines (e.g. Interleukine-8 (IL-8)). These factors can contribute to endothelial cell motility by causing random cell movement (chemokinesis) or by directing migration towards a stimulatory factor (chemotaxis) [32, 33]. By definition, the formation of functional vascular sprouts depends on directional migration of microvascular cells in the surrounding tissue. The mechanisms for migration of these cells are comparable with those involved in invasion of tumor cells. Migration is facilitated by the binding of tumor cell to a basement membrane rich in laminin, collagen IV, and tenascin [19]. Directional endothelial migration is controlled by the ability of these cells to exert mechanical forces on the ECM of the surrounding tissue. Most of the identified ECM-receptors on ECs are of the integrin type [28].

c. Proliferation and Morphogenesis

Endothelial cell proliferation supplies the cells that build the new vessel. Many angiogenic factors increase the number of endothelial cells by enhancing both their proliferation and survival [34]. During angiogenesis, vascular endothelial cells can proliferate as rapidly as bone-marrow cells. This increase in proliferation is one of many events that are required for the formation of a new capillary blood vessel. When the detached endothelial cells are in contact with interstitial provisional matrix components, such as vitronectin, fibronectin, type I collagen, and thrombin, they mediate the formation of a new blood vessel with the vascular basement membrane (VBM) ***(Figure 5)*** [35].

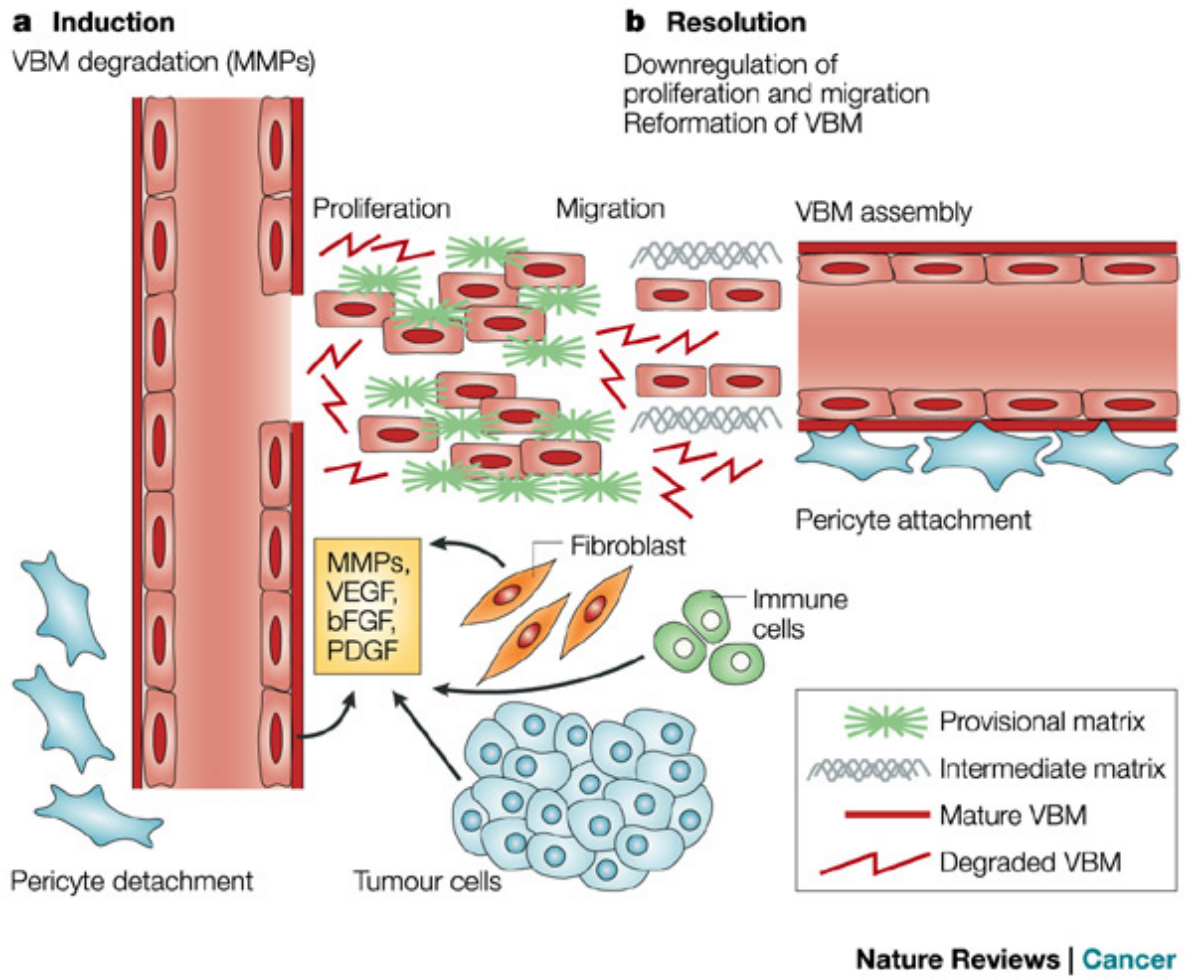

Figure 5. Matrix transitions during angiogenesis. Angiogenesis is associated with degradation and reformation of the VBM. **a.** In response to growth factors and MMPs, the VBM undergoes degradative and structural changes. This transition from mature VBM to provisional matrix promotes the proliferation and migration of vascular endothelial cells. Growth factors, such as VEGF, FGF-2 (b FGF) and platelet derived growth factor (PDGF), are released from the BM, and are also produced by tumor cells, fibroblasts and immune cells. **b.** This induces formation of an intermediate, and then a mature VBM. Together with the vascular endothelial cells and pericytes, the VBM mediates formation of a new blood vessel. The degraded VBM during this process has a crucial role in regulating angiogenesis. (Based on Kalluri 2003) [35].

II.2.2. Role of the vascular basement membrane

The VBM is a self-assembled layer of proteins, glycoproteins and proteoglycans produced by endothelial cells, pericytes and smooth muscle cells (SMCs). Type IV collagen, laminin, fibronectin, nidogen (entactin) and the heparan sulfate proteoglycan (HSPG / perlecan) are among the main components. Basement membrane of normal blood vessels tightly envelops and covers most endothelial

sprouts and pericyte processes. Redundant layers of VBM, visible under conditions where blood vessels undergo regression and regeneration, may provide a scaffold for vascular re-growth [35]. When vascular cells migrate to form new sprouts, the composition of the matrix network is altered. Proteinases expose new cryptic epitopes in ECM proteins (such as in collagen IV) or change their structure (fibrillar versus monomer collagen), which induce ECs and SMCs migration. In addition, a provisional matrix of fibronectin, fibrin and other components provides a support scaffold, guiding ECs to their targets [21, 35].

II.2.3. Role of pericytes

Cellular components of small blood vessels consist only of ECs, whereas larger vessels are surrounded by mural cells. Pericytes, also known as Rouget cells, peri-endothelial cells, or mural cells, are adventitial cells located within the basement membrane of capillaries and postcapillary venules. Because of their multiple cytoplasmic processes, distinctive cytoskeletal elements, and envelopment of endothelial cells, pericytes are generally considered to be contractile cells that stabilize vessel walls and participate in the regulation of blood flow in the microcirculation. Pericytes may also influence endothelial permeability, proliferation, survival, migration, and maturation**.** They are extensively involved in the angiogenic process as well as ECs and participate in vascular remodeling *in vivo*. *In vitro* studies demonstrated that pericytes can inhibit proliferation of ECs by a mechanism that requires contact or close proximity between the two cell types, the inhibition being mediated by Transforming Growth Factor-β1 (TGF-β1). Under hypoxic conditions, however, cultured pericytes were shown to produce VEGF and thus may promote ECs growth in a paracrine way. In cultured human brain pericytes the increased expression of α-smooth muscle actin (α-SMA) suggests a contractile role of these cells and has been shown to be mediated by TGF-β1 [36-38].

II.2.4. Angiogenesis regulators

Angiogenesis is a physiologic process that is tightly regulated and involves a balance between pro-angiogenic and anti-angiogenic factors [39]. The “angiogenic switch” is determined by the opposing faces of pro- and anti-angiogenic factors, it is

turned “Off”, “On”, or is in a balance depending on the activity on each end of the balance. It is likely turned “On” in several diseases such as psoriasis, rheumatoid arthritis [40], diabetic retinopathy [41], and cancer [20, 21, 42]. Switching to an angiogenic phenotype likely requires both up-regulation of angiogenesis activators and down-regulation of angiogenesis inhibitors. The exact molecular mechanisms controlling the “angiogenic switch” are not completely understood, and so far, more than 20 stimulators (including notably VEGF, PDGF, FGF and some integrins), as well as inhibitors of angiogenesis have been identified (More details in section III.1.2.). Among the large number of angiogenesis inhibitors, there is a subset of endogenous matrix-derived angiogenesis inhibitors, (e.g. Arresten, Canstatin, Endostatin, and Tumstatin) [43].

II.2.5. Mechanisms of angiogenesis

The growth, expansion and remodeling of the primary vascular plexus in a mature vasculature occur by two mechanisms: sprouting and intussusception.

a. Sprouting angiogenesis

Sprouting angiogenesis was the first identified form of angiogenesis. Sprouting consists of a number of steps: degradation of the vascular basement membrane, endothelial cell proliferation in response to angiogenic factors, formation of sprouts of endothelial cells reaching out to connect to a neighbouring vessel, and finally formation of a lumen connected on both ends of the tube to the original vascular network [34, 44].

b. Intussusceptive angiogenesis

Non-sprouting angiogenesis, also known as splitting angiogenesis or intussusception, occurs as a longitudinal division of an existing vessel. In this type of vessel formation, the capillary wall extends into the lumen to split a single vessel in two. There are four phases of intussusceptive angiogenesis. First, the two opposing capillary walls establish a zone of contact. Second, the endothelial cell junctions are reorganized and the vessel bilayer is perforated to allow growth factors and cells to

penetrate into the lumen. Third, a core is formed between the two new vessels at the zone of contact that is filled with pericytes and fibroblasts. These cells begin laying collagen fibers into the core to provide an extracellular matrix for the extension of the vessel lumen. The addition of collagen fibrils to the pillar core will stabilize the pillar mechanically. Finally, the core is fleshed out with no alterations to the basic structure. Intussusception is important because it is a reorganization of existing cells. It allows a vast increase in the number of capillaries without a corresponding increase in the number of endothelial cells. This is especially important in embryonic development since there are not enough resources to create a rich microvasculature with new cells every time a new vessel develops. After the formation of the primitive capillary plexus by vasculogenesis and/or sprouting, early developmental vascular growth and remodeling occur predominantly by intussusception. Thus blood vessel formation by intussusception is much faster than by sprouting since extensive cell proliferation, basal membrane degradation and invasion of the surrounding tissue are not required as is the case for sprouting [34, 44].

II.3. Angiogenesis in tumors

Angiogenesis is essential for the development and progression of many human solid tumors. It has been suggested that an outstanding characteristic of tumor cells is their capacity to elicit continuously the growth of new capillary endothelium from the host. The switch from an avascular tumor to an angiogenic phenotype represents a distinct step in the multistep pathogenesis of cancer.

II.3.1. Tumor angiogenesis

The diffusion capacity for oxygen and nutrients in tissues is limited to about 150–200 µm, therefore progressive growth of solid tumors beyond a diameter of 2 to 3 mm^3 is not optimally possible without neo-vascularization. It is thus dependent on the recruitment of angiogenic vessels and an expansion of the tumor vasculature to meet the metabolic requirements of the neoplasic tissue. Tumor metabolism varies with the function and architecture of these new blood vessels [45]. The formation of new tumor microvessels from preexisting vasculature requires a complex interaction

between tumor cells, endothelial cells, stromal cells, and matrix components [46]. Tumor cells have been shown to express angiogenic factors in order to stimulate expansion of the vascular bed. VEGF is expressed by tumor cells, such as glioma cells**,** and is the only known mitogen acting specifically on endothelial cells [47]. VEGF signaling initiates the formation of new vessels by recruiting ECs to form tubes. It also triggers a chain of molecular and cellular events that stabilize the EC tubes by recruiting mural cells and generating an extracellular matrix. It has been previously demonstrated that paracrine signaling *via* platelet derived growth factor B (expressed by ECs) and its receptor PDGFR-β (expressed by MCs) plays a central role in mural cell recruitment and blood vessel maturation and stabilization [48].

II.3.2. Tumor vasculature

The tumor vasculature is structurally and functionally abnormal. Tumor blood vessels are leaky, tortuous, dilated, and saccular and have an arbitrary pattern of inter-connections. Most tumor vessels do not fit into the conventional hierarchy of arterioles, capillaries, and venules. Their abnormalities involve all components of the vessel wall structure and branching patterns: endothelial cells, pericytes and basement membrane. Despite the abnormalities, most tumor vessels do have endothelial cells and pericytes [27, 49-51]. Collectively, these vascular abnormalities lead to an abnormal tumor microenvironment characterized by interstitial hypertension (elevated hydrostatic pressure outside the blood vessels), hypoxia, and acidosis. Impaired blood supply and interstitial hypertension interfere with the delivery of therapeutics to solid tumors. Hypoxia and low pH compromise the cytotoxic functions of immune cells that infiltrate a tumor rendering tumor cells resistant to both radiation and several cytotoxic drugs. Unfortunately, cancer cells are able to survive in this abnormal microenvironment. When normal tissues are subjected to hypoxia (oxygen starvation) - because of a reduction either in blood flow or in the oxygen content of the blood - the eventual result is cell death. To ensure survival, tumor tissues switch into a protective mode by using a specific set of hypoxia-sensing proteins called hypoxia-inducible factors (or HIFs); and they produce angiogenic factors that will attract new blood vessels to restore local blood flow [52].

a. ECs and BM abnormalities in tumor angiogenesis

In tumor blood vessels, ECs have aberrant morphology and form an imperfect lining, with wide junctions at some locations and stacked layers at others. The ECs may contain a large number of fenestrations, vesicle vacuolar organelles or both. The expression of adhesion molecules is also more heterogeneous than in normal tissue, for instance some ECs do not express common endothelial markers (such as CD31) and may undergo apoptosis, thus exposing cancer cells to the lumen (this is called mosaic vessels) ***(Figure 6)***. Basement membrane of tumor vessels is often abnormal, loosely associated with ECs and pericytes, varies in thickness (unusually thick at some locations, entirely absent at others) and has multiple layers in some regions. Vessel diameters are increased, due in part to compression of the immature wall by proliferating tumor cells [20, 27, 50].

b. Pericytes

In tumor blood vessels, pericytes are generally loosely attached to endothelial cells, have multiple layers and extend cytoplasmic processes away from the vessel wall. The data on the mural-cell coverage of tumor vessels is a little controversial, with some studies showing a paucity of mural cells and others showing their abundance. Mural cells are either absent or loosely associated with the tumor endothelium. This abnormality contributes to the leakiness of the vessels, rendering them vulnerable to anti-angiogenic therapies [27, 38].

II.3.3. Mechanisms of tumor angiogenesis

To obtain nutrients for their growth and to metastasize to distant organs, cancer cells coopt host vessels, sprout new vessels from existing ones (sprouting and intussusceptive angiogenesis: mechanisms previously described in II.2.5), and/or recruit endothelial cells from the bone marrow (de novo vessel formation or vasculogenesis from angioblasts or stem cells) ***(Figure 6)*** [50, 53].

Many tumors when developed in highly vascularized tissues, such as brain and lung, can use another mechanism for vascularization, named **“cooption”.** Tumor cells rapidly coopt existing host vessels to form an initially well-vascularized tumor

mass. Vessels are surrounded, coopted by tumor cells and no sprouts are observed [54, 55].

Tumor cells may localize into the wall of tumor blood vessels. They may form blood vessels in association with endothelial cells; this mechanism is named **"mosaic blood vessels".** Tumor cells in mosaic vessels are undergoing intravasation into the lumen and stay temporarily in the capillary vessel wall [56].

Tumor cells may also form tumor blood vessels instead of endothelial cells such as in skin and ovarian cancer. This process called **"vasculogenic mimicry"** seems to be driven by the acquisition, by these tumor cells, of phenotypic characteristics of endothelial type [57].

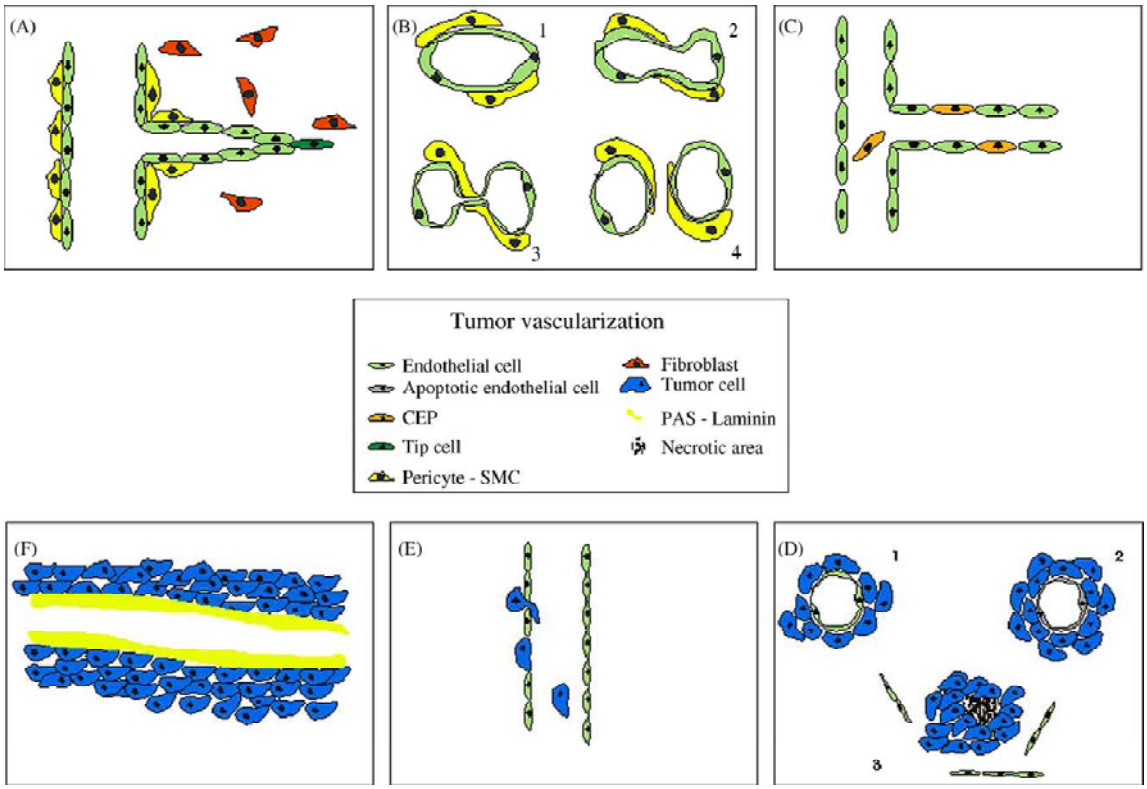

Figure 6. Mechanisms of tumor vascularization. The different mechanisms of tumor vascularization are shown in this figure. These include: (A) sprouting angiogenesis; (B) intussusception; (C) recruitment of circulating endothelial precursors; (D) cooption; (E) mosaic vessels; (F) vascular mimicry (Based on Auguste et al. 2005) [53].

III – ROLE OF ANGIOGENESIS IN GLIOMAS

Malignant gliomas are in general among the most vascularized human tumors. Glioblastoma multiforme (GBM) is one of the most highly vascularized classes of these tumors. The fact that microvascular proliferation cannot be observed in low grade glioma and is frequently present in GBM has led to the assumption that both the development as well as the progression of malignant glioma largely depend on angiogenesis. Thus, angiogenesis represents a crucial patho-physiological step in this tumor entity and antiangiogenic therapy might be especially useful [19, 58-61]. In animal models the growth of glioma xenografts can be inhibited by targeting the angiogenic process. However, unlike many glioma xenografts, human infiltrating gliomas such as GBM have a diffuse infiltrative growth pattern, and preexistent vessels provide many tumor cells with much of their blood supply, particularly in the critical peripheral infiltrative margins [28].

III.1. Pathogenesis of brain tumor angiogenesis

Many of the characteristic features of the vascular microenvironment in gliomas are related to abnormal expression patterns of vasoactive molecules. The high angiogenic activity of the tumor results from a high expression of pro-angiogenic growth factors and their receptors.

III.1.1. Characteristic features of brain tumor microvasculature

The glioma vessel morphology is highly heterogeneous and does not conform to the physiologic microvasculature in brain tissue. As a result, endothelial cells, pericytes, and the basement membrane of glioma vessels reveal significant abnormalities when compared to cerebral vessels. In contrast to cerebral capillaries (~3–5 μm in diameter), gliomas contain tortuous and sinusoidal vessels with diameters ranging between 3 and 40 μm. All morphologic analysis on the glioma microvasculature demonstrated that glioma endothelial cells were surrounded by a continuous basement membrane, although this one was found to be quite thin when compared with that seen around normal vessels. An increase in vessel wall thickness

is one common feature of the glioma vasculature and is attributed to endothelial cell hyperplasia (endothelial wall thickness in glioma ~0.5 µm vs. 0.26 µm in cerebral vessels) reflecting an increase in non-selective transendothelial transport [19, 62-64].

In normal human brain as well as in most glial neoplasms ECM proteins such as fibronectin, laminin, and the different types of collagen are essentially confined to the vessel walls. In GBM, the migration of microvascular cells into the glial tumor tissue during angiogenesis may have been facilitated by an altered expression of ECM components by tumor cells. For migration along blood vessels, interactions between integrins on tumor cells and vascular ECM components are considered to be important. Within the glial compartment, such ECM components are generally lacking, and diffuse infiltrative growth may be facilitated by other molecules like adhesion molecules of the CD44 family, especially since the glial ECM is rich in hyaluronic acid, a potent ligand of CD44 [28, 65]. ECM components such as laminin, fibronectin, collagen type IV, vitronectin, tenascin and hyaluronic acid, have all been shown to be key compounds for glioma cell migration and invasion in experimental model systems. Most of the components expressed within glioma tumors, e.g., laminin, fibronectin and collagen types (I, II, IV and V), are predominantly localized within the basement membrane of existing and newly formed hyperplastic blood vessels. The distribution of laminin, fibronectin and collagen type IV varied regionally within the tumors. These ECM components were found to be strongly associated with the basal lamina of blood vessels, but with deposits also present in the parenchyma of tumors, suggesting a possible role for these proteins during tumor cell invasion. These changes in the expression of ECM molecules indicate that this is a normal host response to environmental changes. The tumor cells may use these molecules either as stimulating or guiding molecules for their migration into the host tissue [66].

Regarding blood vessel maturity, many studies revealed some differentiations because heterogeneity is a common feature of tumor vasculature. Not all tumor-associated vessels have the same structural or functional defects and not all of them exhibit the same organization. Tenascin C, an extracellular matrix molecule, has been described previously to be absent in mature non-pathological brain tissue and to accumulate in the basal lamina of tumor vessels in high grade astrocytomas. It has been suggested that tenascin C may be correlated with the grade of malignancy in

astrocytic tumors [22, 67, 68]. Also, CD105 (endoglin) is expressed in the newly formed blood vessels of the tumor, but not in the mature vessels, either intra- or peri-tumoral [69]. Bian *et. al* [70] in their study for distinction between tumor microvessel endothelial cells from those derived from normal tissues, have revealed several characteristic features of GDMEC (Glioblastoma derived microvessel endothelial cells). GDMEC expressed high levels of CD105, a proliferation-associated cell membrane antigen and a defined endothelial cell marker present on newly formed preliminary capillaries of tumor tissues.

Electron microscopic studies of the blood brain barrier comprising endothelial cells and perivascular astrocytes have identified at least three structural abnormalities of the endothelial lining which all form the basis for an increased microvascular permeability and loss of BBB function in glioma tumors: open endothelial gaps (as inter-endothelial junctions and trans-endothelial channels), cytoplasmic vesicles (as vesicular vacuolar organelles), and fenestrations. Astrocytic alterations include abnormal junctions between astrocytic processes in certain gliomas [19, 71, 72].

Pericytes and vascular smooth muscle cells also contribute to the vascular microenvironment in gliomas. They have been implicated in all stages of neo-vascularization, guiding the migration of endothelial cells, regulating their proliferation, and connecting individual vascular sprouts [18]. Furthermore, they have also been linked to the process of glioma vessel maturation which identified them as regulators of glioma vascularization and of microvascular remodeling and survival [73]. The frequency of pericytes within the glioma microvasculature is a matter of debate since different techniques to identify pericytes have revealed controversial results. Conventional electron microscopy and immuno-electron microscopy have clearly identified a significant number of pericytes or VSMCs in direct contact to endothelial cells within the glioma microvasculature (3- to 5-fold compared with normal brain tissue) [64, 73]. Other results have shown that microvessel pericyte coverage ranges from 10–20% in human glioblastoma specimens [74, 75].

As abnormalities involve all components of the vessel wall structure: endothelial cells, basement membrane and pericytes, all markers used for these patterns might

help to understand the structural and functional alterations during tumor growth and might provide novel therapeutic targets. (More markers will be further detailed in section IV.2).

III.1.2. Mediators of glioma angiogenesis

Glioma microvessels appear to have three principal origins: angiogenesis, cooption, and intussusception. Although the exact biomolecular mechanisms responsible for these distinct vascularization mechanisms are still ambiguous, there is strong evidence that they are mediated by similar growth factors. Glioma angiogenesis is mediated by the release of angiogenic cytokines by the tumor cells. The VEGF and its receptors seem to be the central signaling pathway of glioma angiogenesis [16, 19, 76]. But there are many other important molecules which act angiogenically by stimulating endothelial cell migration and tumor invasiveness, such as PDGF, fibroblast growth factors (FGF-1 and FGF-2), hepatocyte growth factor / scatter factor (HGF / SF) and the angiopoietins (Ang-1 and Ang-2) [77-79]. Also some integrins have a role in glioma associated angiogenesis. Here we will develop two of these mediators:

a. VEGF and its receptors

VEGF acts not only as a growth factor but also as a survival factor for endothelial cells. It plays a central role in mediating the differential steps of tumor angiogenesis and is responsible for many pathological characteristic of the tumor vascular compartment. VEGF is a multifunctional angiogenic cytokine that induces a series of protein phosphorylations, beginning with the autophosphorylation of its main receptor tyrosine kinases VEGFR-1 (known as Flt-1) and VEGFR-2 (known as Flk-1/KDR). These receptors mediate their signals intracellularly via the MAP-kinase pathways. In the normal brain, VEGFR-1 and VEGFR-2 are expressed at very low levels, but become elevated after ischemia and in malignant gliomas. The expression of VEGF is mainly triggered by hypoxia, but also promoted by other vascular cytokines, such as FGF, PDGF, EGF, TNF-α, IL-1β, IL-6 and nitric oxide. In addition, upregulation of VEGF is, at least in part, responsible for the loss of blood brain barrier

function and increased microvascular permeability in gliomas, mediated by the VEGFR-2 [61, 78].

b. Integrin signaling

Integrins are cell-surface receptors of specific ECM molecules, responsible for the interaction of endothelial and tumor cells with the extracellular matrix, mediating cell migration and invasion. The αvβ3 and αvβ5 integrins are considered to positively regulate angiogenesis, because their pharmacological antagonists suppress pathological angiogenesis. Integrin αvβ3 is of special interest in gliomas, because its expression correlates with the histological grade and it is upregulated especially in the proliferating parts of malignant glioma, thus, playing a role in tumor invasion and angiogenesis [21, 80].

III.2. Anti-angiogenesis strategies

Two main anti-angiogenic approaches currently in development are the inhibition of the angiogenic process and vessel formation by the delivery of anti-angiogenic agents or direct targeting and destruction of the tumor vasculature. Inhibition of angiogenesis would represent an approach for blocking tumor growth, possibly circumventing the multidrug resistance problem [22]. Furthermore, angiogenesis inhibitors may help chemotherapy and radiotherapy when given in combination. In this way, cytotoxic agents would kill cancer cells directly, and anti-angiogenic agents would kill them indirectly by depriving them of nutrients [50].

Under physiological conditions angiogenesis in the CNS is tightly down-regulated. Recently a number of endogenous angiogenic inhibitors have been described [81-83], between them tumstatin, endostatin, and angiostatin (proteolytic fragments of collagen IV, XVIII and plasminogen, respectively) that inhibit endothelial cell migration and proliferation; and protease inhibitors that prevent degradation of the basal lamina of blood vessels. There are also some compounds that interfere with the adherence of endothelial cells to matrix proteins (*e.g.,* via blockade of αvβ3 integrin), such as *PEX* (hemopexin fragment), which regulates the interaction of metalloproteinase-2 (MMP-2) and integrin αvβ3 and it is a potent inhibitor of glioma

angiogenesis [84-86]. Other molecules have been also developed such as protein tyrosine kinase inhibitors which prevent phosphorylation in cell signaling by blocking access of ATP [87].

Other targets are vascular endothelial growth factor VEGF/VEGF-receptor complex. Antagonizing VEGF (such as using dominant-negative mutants of the VEGFR-2, or anti-VEGFR2 antibodies) can inhibit the growth of human malignant gliomas in animal models [88, 89]. Furthermore, this inhibition can also be achieved by simultaneous administration of molecules that target both tumor and endothelial cells and acting by separate mechanisms (as PF-4/CTF, CBO-P11) [86, 90]. CBO-P11 is a cyclic peptide (synthesized in our laboratory) derived from VEGF. It significantly blocks the growth of intracranial glioma in nude and syngeneic mice and improves survival.

Antiangiogenic therapies should destroy the tumor vasculature, thereby depriving the tumor of oxygen and nutrients. Jain has stated that certain antiangiogenic agents can also ‘‘normalize’’ the abnormal structure and function of tumor vasculature to make it more efficient for oxygen and drug delivery [91]. Targeting the VEGF signaling pathway can be a potential strategy to reverse some of the abnormalities. Anti-VEGF antibody (Bevacizumab) and anti-VEGFR2 antibody (DC101) prune some tumor vessels and remodel the remaining vasculature in human colon cancer and glioma xenografts as well as murine breast cancers so that it more closely resembles the normal vasculature. The anti-VEGF treatments reduce the size and length as well as permeability of these abnormally dilated and tortuous vessels [92-94].

.

IV – *EX VIVO* IMAGING OF ANGIOGENESIS

To be useful tools for studying angiogenesis, imaging methods should be able to locate sites of angiogenesis, determine level of blood vessel growth, characterize functional abnormalities of vessels, assess vascular heterogeneity and elucidate features that distinguish between tumor-mediated (angiogenic) and normal blood vessels. They should also have potential utility in assessing the efficacy of angiogenesis inhibitors used in the treatment of cancer. Current angiographic methods for visualizing blood vessels in clinics are usually able to evaluate larger arteries and veins but not the microvasculature of tumors or even the sites of angiogenesis. The poor resolution of *in vivo* imaging techniques such as MRI, PET and SPECT *(described before in section I.5)* does not allow imaging of angiogenic areas in the case of small-size tumors such as gliomas. For this purpose, microscopic methods or *ex vivo* imaging modalities may be of some help.

A few microscopic techniques have been developed for image analysis of the microvasculature in glial tissue. These methods are used to compare several vascular parameters in histological tumor sections of human glioblastoma with those in normal cerebral cortex. They are in part based on a significant increase in mean number, area, and perimeter of blood vessels per microscopic field in glioblastoma compared to normal cerebral area. However, each of the methods being potentially used for this diagnosis presents advantages and limits.

IV.1. Imaging morphological abnormalities of blood vessels

Imaging studies by conventional, UV-Vis, fluorescence, and electron microscopy have identified several cellular and molecular abnormalities that distinguish tumor vessels from their normal counterparts and help to explain their unusual appearance, disturbed blood flow, and leakiness.

IV.1.1. Classical histological examination

Traditionally, the diagnosis of tumors is based on visual inspection of stained tissue sections by an experienced pathologist. The standard histopathological procedures have in common that they “tag” and visualize the distribution and structure of cellular components in tissue sections using standard light microscopy-based techniques**.** Distinction between tumor and normal brain tissue is particularly important in neurosurgery in order to maximally resect tumor cells and to minimally affect brain function.

The diagnosis and grading of individual gliomas is based primarily on morphological pattern recognition. Cryostat sections for intraoperative diagnosis are prepared from fresh frozen samples. They are fixed, stained by hematoxylin and eosin (H&E), and evaluated by a neuropathologist. However, in 20 to 30% of cases there is an inability to provide diagnostic answers due to the high heterogeneity of tumors. Furthermore, the quality and quantity of tissue specimens constitute in some cases a problem for an accurate diagnosis. The histological classification of human gliomas nowadays remains a challenge. The aim is to define the histological type of glioma (astrocytic, oligodendrocytic, or mixed) and the grade in order to classify the patients and give them an accurate treatment. Although the standard remains the WHO classification, this classification suffers from a lack of reproducibility between pathologists. It is based on cell density, atypical nuclei, mitoses, endothelial cell hyperplasia, microvascular density and proliferation and necrosis. In particular this classification does not take into account the intrinsic morphological heterogeneity of infiltrative gliomas and does not discriminate the tumor cells from the residual brain parenchyma. The classification is not trivial, since the morphology used to classify the tumors forms a histological continuum and a single tumor may encompass regions of different morphology and cellularity with the highest grade of malignancy being relevant for the final classification of the tumor and the resulting therapy [95, 96].

IV.1.2. Electron microscopic examination

A key indicator emerged from the examination of blood vessels in different organs by transmission electron microscopy in the 1950s. These studies identified

three general types of capillaries: continuous, fenestrated, and discontinuous. Blood brain barrier was recognized as an example of specialized capillary endothelial cells joined by tight junctions. Three microvessel populations may occur in brain tumors: continuous nonfenestrated, continuous fenestrated and discontinuous (with or without fenestrations) [62].

Transmission and scanning electron microscopic analyses have gained further insight into ultrastructural alterations of the glioma vessel wall and potential transvascular transport mechanisms. Many articles describe and illustrate ultra-structural abnormalities in brain tumors such as fenestrations, endothelial gaps, pinocytotic vesicles, and transendothelial channels [19, 62, 63, 71, 97].

Electron microscopic studies may help for the understanding of structural and functional abnormalities of tumor blood vessels and analyzing at a submicroscopic level the morphological changes in vascular microenvironment of astrocytic tumors. The attempt is to understand the pathological aspects that may help researches for the design of future therapeutic strategies since current brain tumor treatment protocols are based on the histological and the vascular phenotype of the tumor microenvironment.

IV.2. Imaging molecular markers of blood vessels

Immunohistochemical markers and molecular approaches have also been integrated into the classification of gliomas with respect to their glial lineage (e.g., whether astrocytic or oligodendroglial), their clinical behavior, and their response to treatment [6]. Markers used to understand the structural and functional alterations during tumor growth highlight all components of the vessel wall structure: endothelial cells, basement membrane and pericytes. Immunohistochemistry (IHC) is widely used in basic research to understand the distribution and localization of biomarkers and differentially expressed proteins in different parts of a biological tissue.

The current standard marker of angiogenesis in cancer is the intra-tumor microvessel density (MVD). This is measured as the number of immunostained blood vessels per high power microscopic field on a few micrometers thick histological section, counted in an area of high vascular density [98].

Blood vessel detection by UV-Vis means on tissue sections is improved by immunohistochemical staining of endothelial cell markers, most commonly CD31 (Platelet endothelial cell adhesion molecule or PECAM), CD34, factor VIII-related antigen (von Willebrand factor) and *Ulex europaeus* lectin [51, 56, 99]. Vessels are also identified by their binding of intravascularly injected fluorescent probes (such as cationic liposomes which are positively charged lipid vesicles used as drug delivery vehicles) [100] and *Lycopersicon esculentum* lectin [51].

Because vascular endothelial cells are present in much smaller numbers than tumor cells, the density of angiogenic markers is low. Not all markers have the same specificity and they should be detectable at low concentrations. CD31 is an endothelial marker that is commonly used to identify tumor vessels [101]. Like the lectin, CD31 immunoreactivity defines the luminal surface of tumor vessels, but, unlike the lectin, it is also present on sprouts radiating from the vessel lining into the tumor [51, 101].

Blood vessels can also be marked by antibodies to basement membrane proteins. Regardless of the marker, the appearance of blood vessels in histological sections is greatly influenced by section thickness. Only short segments of vessels are visible in thinner sections, but the vascular network can be seen in thicker sections [99, 102]. Membrane proteins selectively expressed by angiogenic blood vessels provide potential markers for imaging tumors. Reported examples include αvβ3, αvβ5, and α5β1 integrins [80, 103] CD105 (endoglin) [104] **,** complexes of vascular endothelial growth factor (VEGF) and its receptor VEGFR-2 [105], CD36 (thrombospondin-1 receptor) [106], Thy-1 [107], prostate-specific membrane antigen [108] and tumor endothelial markers [109].

As a key cellular component of the microvasculature, pericytes are a potential target for vascular imaging agents, but the cells are located outside the endothelial

barrier. Reports that pericytes are an inconsistent component of tumor vessels and that their absence is a sign of vessel immaturity raise additional questions. Pericytes are identified by their distinctive location within the vascular basement membrane or by selective markers. Immunohistochemical markers of pericytes mostly known are α-SMA [36, 73, 110], platelet-derived growth factor receptor (PDGFR)-β [48, 111], desmin [112], nestin [113], aminopeptidase A, aminopeptidase N (CD13) [113], matrix metalloproteinase-9 (gelatinase B) [114], and regulator of G-protein signaling-5 [115].

Unfortunately, none of these markers is unique to pericytes. Moreover, pericytes are heterogeneous and may not express all markers. The most commonly used marker, α-SMA, is expressed by the mural cells of most arterioles and venules but not by capillaries, and has variable expression in tumors and other sites of angiogenesis [110, 112, 114]. Therefore, the absence of immuno-reactivity for α-SMA does not indicate an absence of pericytes. Nevertheless, when multiple markers are used for identification, pericytes are consistently found on tumor vessels and growing blood vessels at a stage when they do not express α-SMA [36, 111]. Marker expression can also vary in different organs and with pathological conditions. Because no single commonly used marker identifies all pericytes with certainty, pericytes identification is not systematic in pathological conditions, as for cancers, i.e., when the cells change their expression of marker proteins. Other limits result from differences in the markers used to identify pericytes or differences in section thickness, where partial pericyte coverage is missed in thin histological sections [36, 38].

The use of labeled probes, which can be visualized by fluorescence microscopy, confocal microscopy, scanning electron microscopy and transmission electron microscopy, is helping to define organ-, vessel- and cell-specific differences in the vasculature of normal organs, and of disease sites such as tumors. But it is very limited since actually, and in the best conditions, no more than three labels may be used on a same sample at once. Moreover, there may be interference between antibodies used to highlight blood vessels ultrastructure. Besides, the routine use of molecular related markers is laborious, requires suitable technical means, and is thus

time and money consuming. Furthermore, the high level of heterogeneity frequently encountered in gliomas (at histological, biological and molecular levels) does not facilitate the use of such markers [5, 116, 117]. In addition, these global profiling approaches have not adequately represented intra-tumor heterogeneity, which could be a critical issue if sub-populations of tumor cells had differential growth or migratory properties.

In conclusion, the most popular methods for imaging gliomas *in vivo* or *ex vivo* in humans still suffer from a number of important limitations. Angiographic methods have a poor resolution to spatially resolve the microvasculature. *Ex vivo* techniques such as microscopic methods ranging from fluorescence, confocal and multiphoton microscopy to electron microscopic imaging have not been demonstrated for elucidating systematically the structural and functional abnormalities of angiogenic blood vessels. Microscopic methods provide their highest resolution on preserved tissue specimens, whereas clinical methods give images of living tissues deep within the body but at much lower resolution and specificity, and generally cannot resolve vessels of the micro-circulation neither small size tumors as metastases. Future challenges include developing new imaging methods that can bridge this resolution gap and specifically identify angiogenic vessels.

On the other hand, glioma cell invasion and angiogenesis, today, can only be addressed by histological means. These ones are performed *in vitro*, require chemical reagents and staining, and limit the examination to a single observation time point. Any fixation and embedding procedure always change the morphology and the molecular contents of tissues and may distort the structure of cells. For example, immersion of tissues in lipid solvents, such as xylene, dissolves the tissue lipids. This treatment causes alterations for any further analysis.

A convenient technique to study glioma tissues should permit a direct, quantitative, sequential, and reproducible assessment of both the tumor cell as well as the microvascular compartment. Thus, it is still and crucially required to develop other molecular imaging modalities.

Chapter II

Vibrational Spectro-Imaging

Vibrational Spectro-Imaging

I – INTRODUCTION

Among the several methods that may be employed for the diagnosis of tumors, vibrational spectroscopies and spectro-imaging have been applied successfully, owing the possibility of performing analysis of the different chemical compositions and molecular structures of healthy and pathological tissues. Vibrational spectroscopy belongs to techniques which benefit from the interaction of light with matter. Photons that interact with a sample are either absorbed or scattered; photons of specific energy are absorbed, and the pattern of absorption provides information, or a fingerprint, on the molecules that are present in the sample.

Two vibrational spectroscopy techniques are available, infrared (IR) spectroscopy and Raman spectroscopy, and may be considered as fast analytical tools for providing reproducible information about the organic contents of biosamples. Moreover, they allow analyzing samples with no need of laborious and invasive sampling procedures, or the use of chemical reagents to obtain a result. In particular, IR spectroscopy provides the possibility to perform a qualitative and quantitative analysis at a molecular level.

Over the last decade, major technological advances occurred for many components of vibrational spectroscopy instruments, including the introduction of microscopes, new multi-channel detectors, tunable diode lasers, and optical fibers. One of the big advantages of vibrational spectroscopy, especially IR, is that it is not limited to a particular state of the sample. Spectra can be obtained from liquids, solids (pellets, powders, films), emulsions, suspensions, gases and tissues. In principle, the Raman technique has also a distinct advantage over IR for the analysis of biofluids, due to the weak scattering of water [118, 119].

II – PRINCIPLES OF VIBRATIONAL SPECTROSCOPY

II.1. IR spectroscopy

IR spectroscopy deals with the mid-infrared region (2.5-25 µm) of the electromagnetic spectrum ***(Figure 7)***, which is the most informative for biosamples since these ones contain mainly organic compounds, although the far (25-1000 µm) and near IR (0.75-2.5 µm) have proved some benefits.

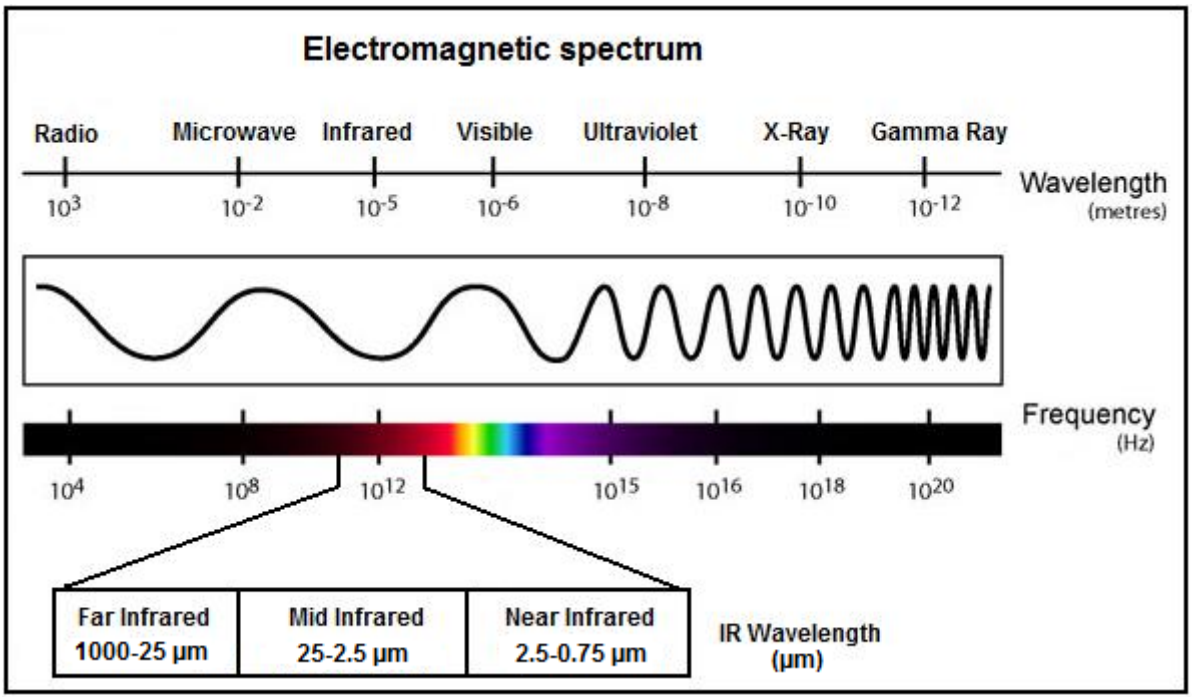

Figure 7. Electromagnetic spectrum with wavelength and frequency: It shows IR region divided in near, mid and far IR regions with their appropriate wavelength limits.

This vibrational spectroscopy is considered as a nondestructive photonic technique that provides a rapid measure of sample chemistry. Moreover, infrared spectral analyses have been widely used to study a variety of samples in different chemical and biological fields. IR spectroscopy is based on the absorption of infrared radiation by the material analyzed. It allows performing a chemical analysis *via* the detection of vibrations that are characteristic of chemical bonds. When the

wavelength (energy) provided by the light beam is close to energy vibration of the molecule, this one absorbs the radiation and a decrease in the reflected or transmitted intensity occurs.

Vibrations that result in a change of the dipole moment of the molecule are observed in the IR. The frequency or wavelength of absorption depends on the relative masses of the atoms and the force constants of the bonds. In general, functional groups that have a strong dipole give rise to strong absorptions in the IR ***(Figure 8)***. The number of normal frequencies of a molecule consisting of n atoms can be determined by the following calculations based on the theory of Groups: A nonlinear molecule with n atoms has 3n−6 normal modes of vibrations, whereas a linear molecule has 3n−5 normal modes of vibration. For organic compounds, the observations of the wavenumbers with the relative intensities are sufficient to identify a chemical component or a specific chemical bond. Therefore, mid-infrared spectroscopy is a global analytical method for biosamples, and an infrared spectrum of a molecule may be considered as the fingerprint of that one [120].

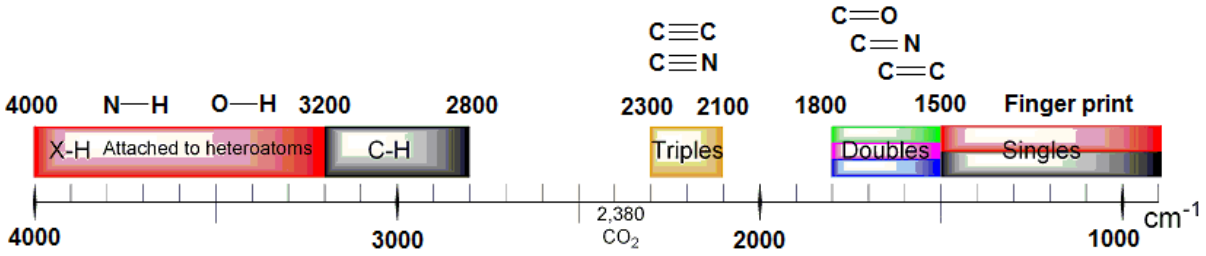

Figure 8. Summary of absorptions of bonds in organic molecules in the mid infrared region (4000-1000 cm^{-1}).

In the mid-infrared range are revealed mainly two types of molecular vibrations: stretching and bending. A stretching vibration (ν) is a rhythmical movement along the bond axis such that the interatomic distance is increasing or decreasing. A bending vibration (δ) (e.g. scissoring, rocking, wagging, and twisting vibrations) consists of a change in the bond angle between bonds. The bond axis (defined as the line directly joining two bonded atoms) may rock back and forth within the plane it shares with another bond or bend back and forth outside the plane ***(Figures 9)***.

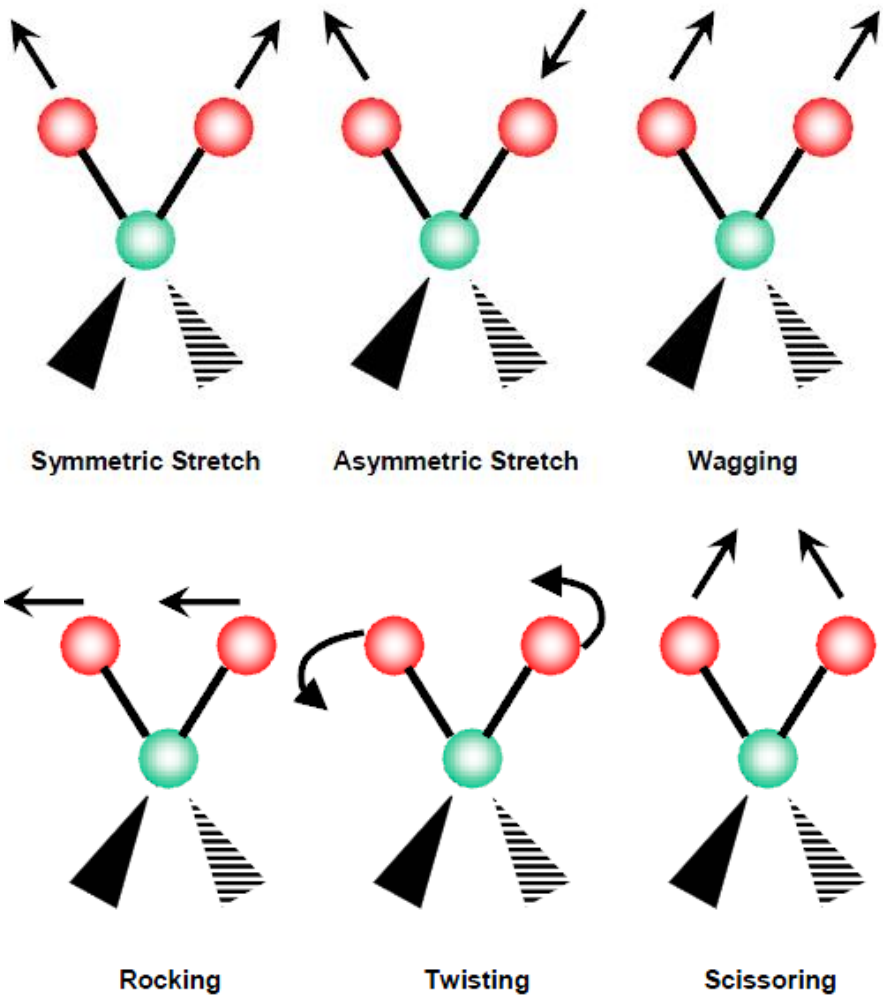

Figure 9. Types of vibrations bonds. The bonds between atoms in the molecule stretch and bend, absorbing infrared energy and creating the infrared spectrum. A molecule will absorb infrared light when the vibration (stretch or bend) results in a molecular dipole moment change.

II.2. Raman spectroscopy

Raman spectroscopy relies on inelastic scattering, or Raman scattering, of the monochromatic light. Excitation of light may range in the ultraviolet (UV), visible or near infrared domains of light [118]. When samples are illuminated with a laser beam, this latter interacts with the excitations in the sample, resulting in a variation of the energy of the laser photons being shifted up or down; this is called Raman scattering ***(Figure 10)***. Light from the source is collected with a lens and sent through a monochromator. Wavelengths close to the laser line, due to elastic Rayleigh scattering, are filtered out while the rest of the collected light is directed onto a

detector. The Raman effect occurs when the light hits a molecule, interacts with the electrons of its bonds and the incident photon excites one of the electrons in a virtual energy state. Two types of scattering may occur: Stokes Raman scattering when the molecule relax into a higher vibrational excited state than the original excitation energy state; and anti-Stokes Raman scattering occurs if the molecule was already in a high vibration energy state and thus returns to a lower state ***(Figure 11)***.

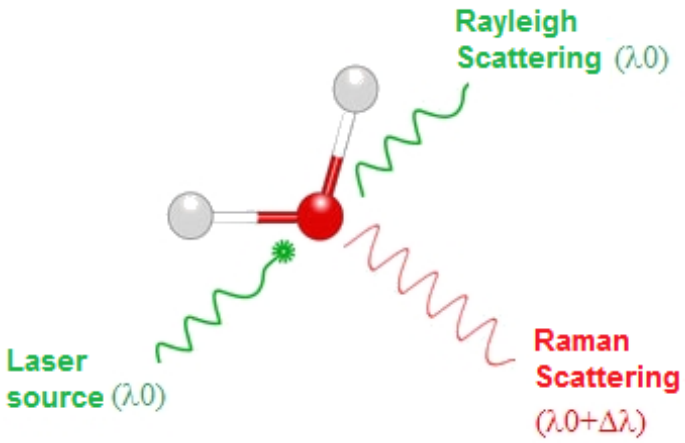

Figure 10. Principle of Raman scattering.

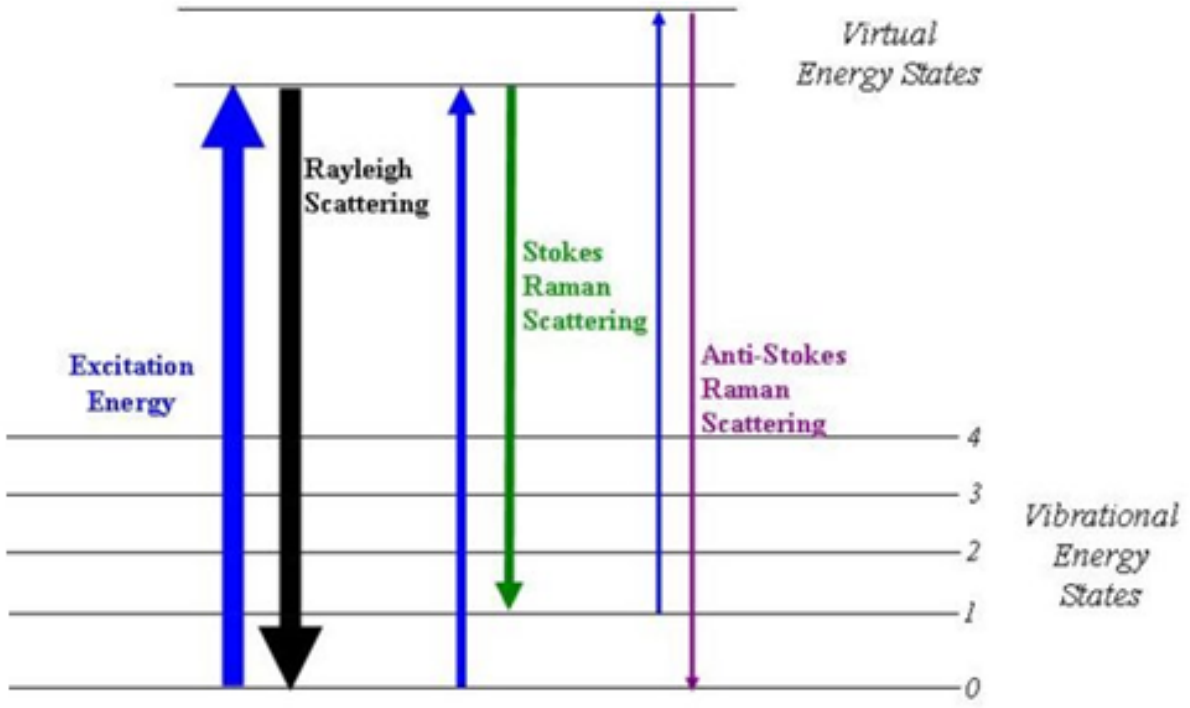

Figure 11. Energy level diagram showing the state involved in Raman signal.

Raman spectroscopy is a non-destructive technique that does not require previous sample preparation, allowing data collection, repetition, or complementation. Recently, it has been extensively developed to show its potential for the diagnosis of pathogens, the analysis of blood components, and for the study of tissue lesions, tumors…etc. [121-129]. The advances in optical-electronic devices, mainly in detectors and lasers, have increased the number of potential applications and thus active research groups in this field.

Until recently, most Raman spectrometers combined the spectral and the lateral information using serial registration procedures. Consequently, data acquisition was really time-consuming [130]. Another major disadvantage remains: it is that Raman light scattering of a biological sample is an inherently weak effect since only one photon over 10^6 is scattered and thus provides the Raman signal. The consequence of this weak sensitivity is that applicability of Raman spectroscopy to biological studies remains limited, notably for quantitative studies [131]. An alternative would be the utilization of the coherent anti-stokes Raman spectroscopy (CARS) technique. It is sensitive to the same vibrational signatures of molecules as seen in Raman spectroscopy, typically the nuclear vibrations of chemical bonds. However, unlike Raman spectroscopy, CARS employs multiple photons to address the molecular vibrations, and produces a signal in which the emitted waves are coherent with one another. As a result, CARS is orders of magnitude stronger than spontaneous Raman emission. This technique is actually under development, but in the future it should be able to fight with IR spectroscopy in terms of sensitivity and information level obtained from sample chemical contents.

Nevertheless, other limits strongly affect the applicability of Raman-related techniques to biology; as an example, biological tissues exhibit strong auto-fluorescence due to the presence of cellular components, and this may obscure the Raman spectra obtained when visible excitation is used. Alternatively, it is possible to use UV light at wavelengths below 270 nm to circumvent the fluorescence interference problem. However, with UV resonance excitation, the tissue penetration depth is about a few micrometers. Thus, this technique might be found suitable for analyzing surface layers although damages may occur on biosamples when using UV light [118].

Although water is a weak scatterer in the Raman, not all fluids can be measured with all available excitations. For example, analysis of intact blood is not possible with an excitation in the visible because the main component of blood is the protein hemoglobin, and the associated heme group has strong absorption bands in the 400–520 nm region. Dilution of blood with a buffer or the alternative use of near-infrared excitation can overcome this limit. However, the use of high intensity lasers induces heating of the sample, thus damaging his organic contents [132]. This is probably the major limit of actual Raman spectrometers for biosample analyses.

Raman spectroscopy offers several advantages for microscopic analysis. A Raman microscope consists in a standard optical microscope, an excitation laser, a monochromator, and a sensitive detector such as charge coupled device (CCD) or a photomultiplier tube (PMT). Although Raman microspectroscopy is not highly sensitive and may be interfered by laser-induced fluorescence, it allows for confocal analyses, less water interference, and higher spectral resolution than IR. Nevertheless, the heating destruction of the sample is due to his prolonged exposure to the laser beam for obtaining high signal-to-noise (S/N ratio) Raman spectra [119]. This makes Raman spectroscopy and imaging unsuitable for small size samples, such as single cells or thin tissue sections, where the small amount organic contents in presence will require high intensity lasers and/or long acquisition times for obtaining a signal.

All these characteristics and factors that we stated above might explain why there are twice as many biomedical applications of IR spectroscopy as Raman spectroscopy. That’s also why we were further interested in the biomedical applications of IR spectroscopy.

III – IR SPECTROSCOPY TECHNIQUES AND APPLICATIONS

III.1. IR spectroscopy Techniques

III.1.1. Sample processing

IR spectroscopy allows analyzing organic materials mainly. The vast diversity of experimental applications allows many types of samples, whatever their physical condition. There are several types of experimental procedures:

a. Transmission

Transmission is the property of a substance to allow the passage of light, with some or none of the incident photons being absorbed in the process. During the process, layers are deposited on an IR transparent substrate. Examples of substances tested in transmission: Powder that should be dispersed in a KBr pellet, Polymer films if their thickness is <10µm, or substances that should be dissolved in a solvent by using liquid cells. Examples of materials that transmit infrared: KBr, CaF_2, ZnSe, Si.

b. Reflection

Reflection techniques occur by collecting light reflected from an interface air/sample, solid/sample, or liquid/sample. In internal reflection also called attenuated total reflection (ATR) technique, the beam of infrared passes through the ATR crystal (e.g. Germanium, ZnSe, Diamond, etc.…) in a manner that it reflects the internal surface of the sample. This reflection forms the evanescent wave which extends into the sample (on < 1 micrometer). Then the beam is collected by a detector when exits the crystal. The ATR technique is used for a variety of materials and requires minimal or no sample preparation, but it has a sensitivity 3-4 orders of magnitude lower than for transmission measurements. There are also other types of reflection techniques

such as: external reflection or specular reflection used for smooth surfaces, and combination of the two types or diffuse reflection used for rough surfaces.

III.1.2. IR spectra processing

The infrared spectrum of a sample is collected by passing a beam of infrared light through the sample. This can be done with a monochromatic beam which changes in wavelength over time, or by using a Michelson interferometer with Fourier Transform (FT) instrument to measure all wavelengths at once. From this, a transmittance or absorbance spectrum can be produced and shows at which IR wavelengths the sample absorbs.

a. Michelson interferometer

The essential piece of optical hardware in a FTIR spectrometer is the interferometer. The basic scheme of a Michelson interferometer is shown in ***Figure 12A***. The infrared beam from the source is directed towards the interferometer, when the IR light hits the beam splitter, half of the beam passes through it directed to a mobile mirror, while the other half is reflected and directed to the fixed mirror. When the two beams recombine again on the beam splitter, destructive or constructive interferences appear depending on the position of the mobile mirror. The modulated beam is then directed from the two mirrors to the sample, where absorptions are involved. Then the beam arrives on a detector to be transformed into an electrical signal. The signal detector appears as an interferogram (i.e. a signing of the intensity (I) depending on the position of the mirror). The interferogram ***(Figure 12B)***, which is the sum of all the frequencies of the beam, is then converted into an infrared spectrum by a mathematical operation called Fourier Transform.

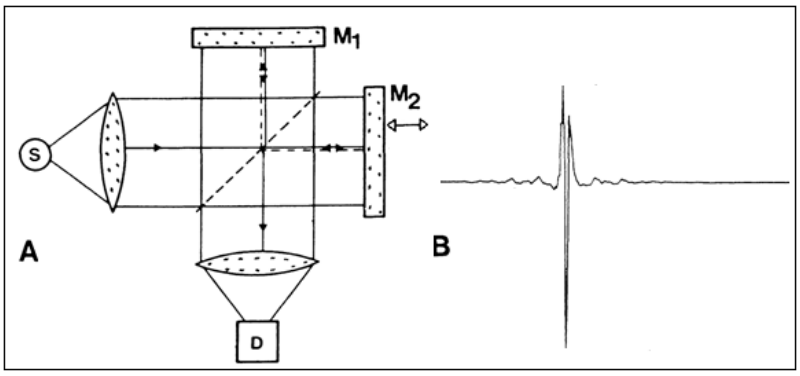

Figure 12. A) Schematics of a Michelson interferometer, S: source, D: detector, M1: fixed mirror, M2: mobile mirror, X: mirror displacement, **B)** Signal measured by detector D. This is the interferogram which will be converted into a spectrum by means of a mathematical operation called Fourier transform (FT).

b. Final spectrum

To obtain a final transmittance spectrum, three steps are necessary ***(Figure 13)***:

- An interferogram measured without sample in the optical path is Fourier transformed and yields a reference spectrum or background (B).
- An interferogram measured with a sample in the optical path is Fourier transformed and yields a sample spectrum (S). (S) is similar to (B) but has less intensity at the wavenumbers where the sample absorbs.
- The final transmittance spectrum T is defined as the ratio T=S/B.

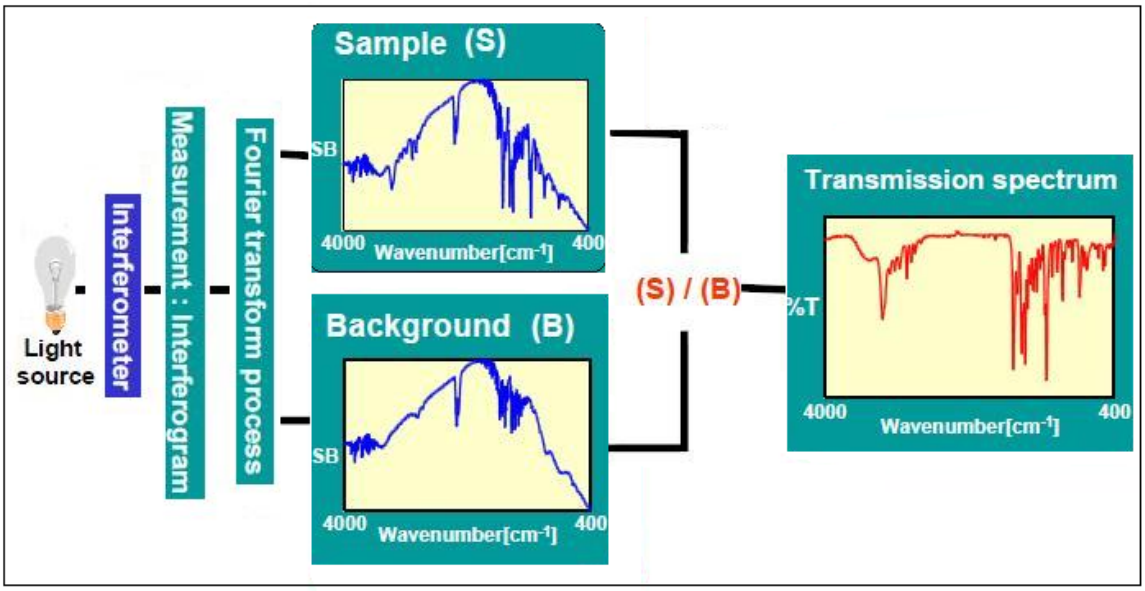

Figure 13. Process to obtain a final spectrum

The reference spectrum is used mainly to prevent fluctuations in the output of the source affecting the data. The final transmittance spectrum is the fraction of the incident light at a specific wavelength that passes through a sample:

$$T = I / I_0$$

where (I_0) is the intensity of the incident light and (I) is the intensity of the light coming out of the sample. Transmittance is related to absorbance by the equation:

$$A = - \log_{10} T$$

c. Detector properties

Two main types of IR detectors are available: thermal and photonic. The most commonly used are: The Deuterated triglycine sulfate (DTGS) detector which is a thermal detector that operates at room temperature. It is in thermal equilibrium with the environment. And the Mercury cadmium telluride (MCT) detector which is a photonic or photoconductive detector, it has to be cooled to cut thermal noise. It usually operates at the temperature of liquid nitrogen.

The detection limit of an IR detector is the number of photons necessary for a signal to be recorded.

III.1.3. Advantages of FTIR over conventional IR

Besides its high wavenumber accuracy, FTIR offers other advantageous features, which make it superior to conventional IR:

- The circular apertures used in FTIR spectrometers have a larger area than the linear slits used in conventional spectrometers, thus enabling higher throughput of radiation.

- In conventional spectrometers the spectrum is measured directly by recording the intensity at different monochromator settings, one after the other. In FTIR, all frequencies emanating from the IR source hit simultaneously the detector.

- The measuring time in FTIR is the time needed to move mirror M2 over a distance proportional to the desired resolution. As the mirror can be moved very fast, complete spectra can be measured in fractions of a second.

III.1.4. IR microscopy and imaging

With IR microscopy (where a spectrometer is coupled to a microscope), the chemical information of a sample is obtained from a microscopic volume, which may be close to the cellular level or even below. This spatially resolved investigation of samples is useful for analyzing biological tissues. The major advantage of IR microscopy over microscopic methods in the visible / UV spectral region is its ability to monitor the chemical composition using the inherent spectral properties of the components [133].

The term infrared microscopy covers two main types of diffraction-limited microscopy. The first one uses a single detector and thus provides optical visualization plus IR spectroscopic data collection at one point of the sample. Point-by-point mapping of a sample area is also possible, although IR spectra acquisition time may be very long. The second technique employs arrays (linear or focal plane) of detectors and thus provides optical visualization plus a spatially resolved IR mapping of a sample area. In this case, the term “FTIR imaging” may be used to discriminate with “FTIR microscopy”. One advantage of FTIR microscopy is the possibility to modulate the aperture, thus allowing a “confocal-like” microscopy of the sample. In this case, it becomes possible to obtain information from the sample at a spatial resolution below the diffraction limit, i.e., from a sample area smaller than the IR vibration length. As a consequence, the limit of this microscopy will be the level of signal obtained, which is usually very poor for apertures more than 50% smaller than the diffraction limit. On the other hand, FTIR imaging uses arrays of detectors without a physical control of aperture but with a magnification level. In other words, the spatial resolution of the image is determined by the size of the detectors and the

magnification level. As an example, a 6.25*6.25 µm pixel-size is obtained on the final IR image with FTIR imaging system using detectors of 25*25 µm and a 4X magnification level of the microscope. It means that a spectrum is collected every step of 6.25 µm (named “step-size” resolution), whatever the diffraction limit. Therefore, for spectral resolutions below 6.25*6.25 µm, i.e., below 1600 cm^{-1}, there is overlapping of information from the adjacent pixels. This has to be taken into account for the interpretation of results. Nevertheless, the development of linear and focal plane arrays of detectors opened the way to the routine use of FTIR imaging for biosample analyses, which is mainly due to the enormous gain of time in FTIR image acquisitions with respect to FTIR micro-spectroscopy.

a. Arrays of detectors

Spectra may be measured using only one detector (FTIR microscopy) or a series of detectors physicaly arranged as Linear Arrays (LA; typically 16 or 32 detectors) or the two-dimensional Focal Plane Arrays (FPA; typically 64*64 = 4096 detectors or 128*128 = 16384 detectors). With FTIR microscopy, a reconstructed FTIR image of a sample is obtained point-by-point by moving the sample in the x and y directions using a computer-controlled stage. For mapping a sample with LA or FPA detectors, sample movements are tremendously reduced, thus saving time in FTIR spectra acquisitions and reducing possible displacement errors. FPA imaging, with its ability to collect tens of thousands of spectra simultaneously is orders of magnitude faster than linear arrays which can typically collect 16 to 32 spectra simultaneously, which are in turn much faster than single-point mapping. However, the disadvantage at using FPA or LA detectors is that the photon flux produced by the IR source is divided by 16 to 16.10^3, thus necessitating longer acquisition time to obtain high quality spectra with appropriate S/N for further spectral data treatment and interpretation. In theory, the same S/N should be obtained by FTIR microscopy and imaging means as soon as a sample has absorbed the same count of photons. In the practice however, the FTIR spectroscopy technique is sensitive enough to obtain high S/N with a limited number of scans, over which the absorption of photons does not mean a higher quality of the spectrum obtained. One may also consider that long acquisition time is also affected by changes in the environmental conditions,

notably for CO_2 and H_2O in air, making the background spectrum lifetime quite limited. To overcome this limit, the N_2 purge of the system must be optimized, which usually requires modifications of commercial IR instruments. Therefore, FTIR imaging maintains a significant advantage over FTIR microscopy in term of acquisition time for large sample areas.

b. Data analysis

The data volume obtained in chemical imaging is called hyperspectral as many spectral wavelengths are collected and the data format is called a hypercube. It is visualized as a three-dimensional block: two spatial dimensions (x and y) and a series of wavelength (λ) making up the third spectral axis. Data analysis methods for chemical imaging data sets typically employ mathematical algorithms common to single point spectroscopy or to image analysis. The reasoning is that the spectrum acquired by each detector is equivalent to a single point spectrum; therefore pre-processing, chemometrics and pattern recognition techniques are utilized with the similar goal to separate chemical and physical information and perform a qualitative or quantitative characterization of individual sample components. Spectral data processing is necessary regarding the complexity of biological spectra. Due to the composition of samples, containing hundreds to thousands of molecules in very different and variable concentrations, their absorptions are overlapped in small spectral regions, mainly 3050-2800 and 1750-900 cm^{-1}, where the most useful spectral information is found for the mid-infrared range.

III.2. FTIR Bio-applications

FTIR spectroscopy is widely used and adaptable method for chemical analysis, which produces a spectrum with characteristic spectral absorption bands from a single molecular species at specific vibrational frequencies ***(Figure 14)***. The huge information found in IR spectra of biosamples grants itself to the operation of data bases and the “fingerprint” approach to chemical identification.

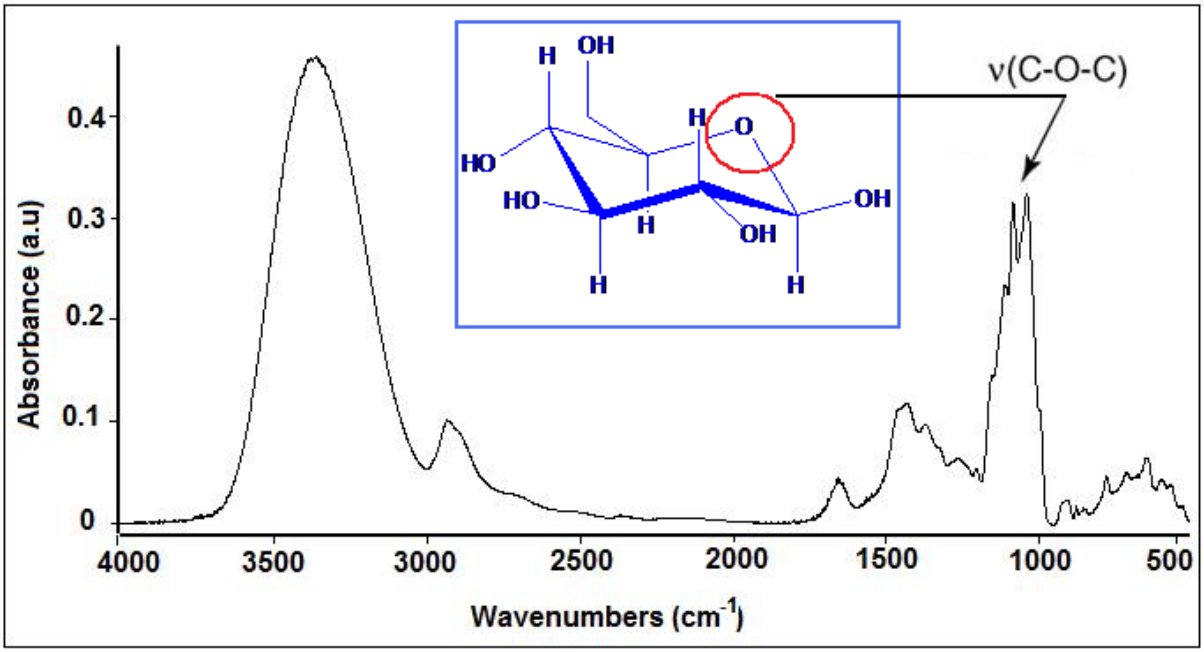

Figure 14. IR spectrum of β-D-Glucose (pure product). IR reveals the ν(C-O-C) at 1033 cm^{-1}.

For years, FTIR spectroscopy has been widely applied as an analytical technique in different fields as geology, material sciences, polymers, engineering, chemical and pharmaceutical industries…etc. for the study of molecular structure of compounds. However, it found also an application in biology since rapid advances in biomedical sciences required new chemical and structural information of biological materials. These include kidney stones [134, 135] and biological fluids such as synovial fluid [136] and plasma which was studied in our laboratory [137-139]. Due to its unique fingerprinting capabilities, infrared spectroscopy is a very valuable tool for biomolecular investigations.

Infrared spectra of tissues from various biological organs show similarities in main spectral features, and consist of several bands similar to those obtained from IR spectra of mixtures of extracellular and intracellular proteins and typical cell components, such as nucleic acids, lipids, and carbohydrates, which are the main constituents of biological tissues. The bands observed in the IR spectra of the samples revealed the various modes of the functional groups in the molecules of these constituents. Detailed assignments of the IR bands in various tissues have

been established by comparison of the IR spectra of proteins, nucleic acids, lipids, and carbohydrates isolated from tissues and cultured cells ***(Figure 15)***.

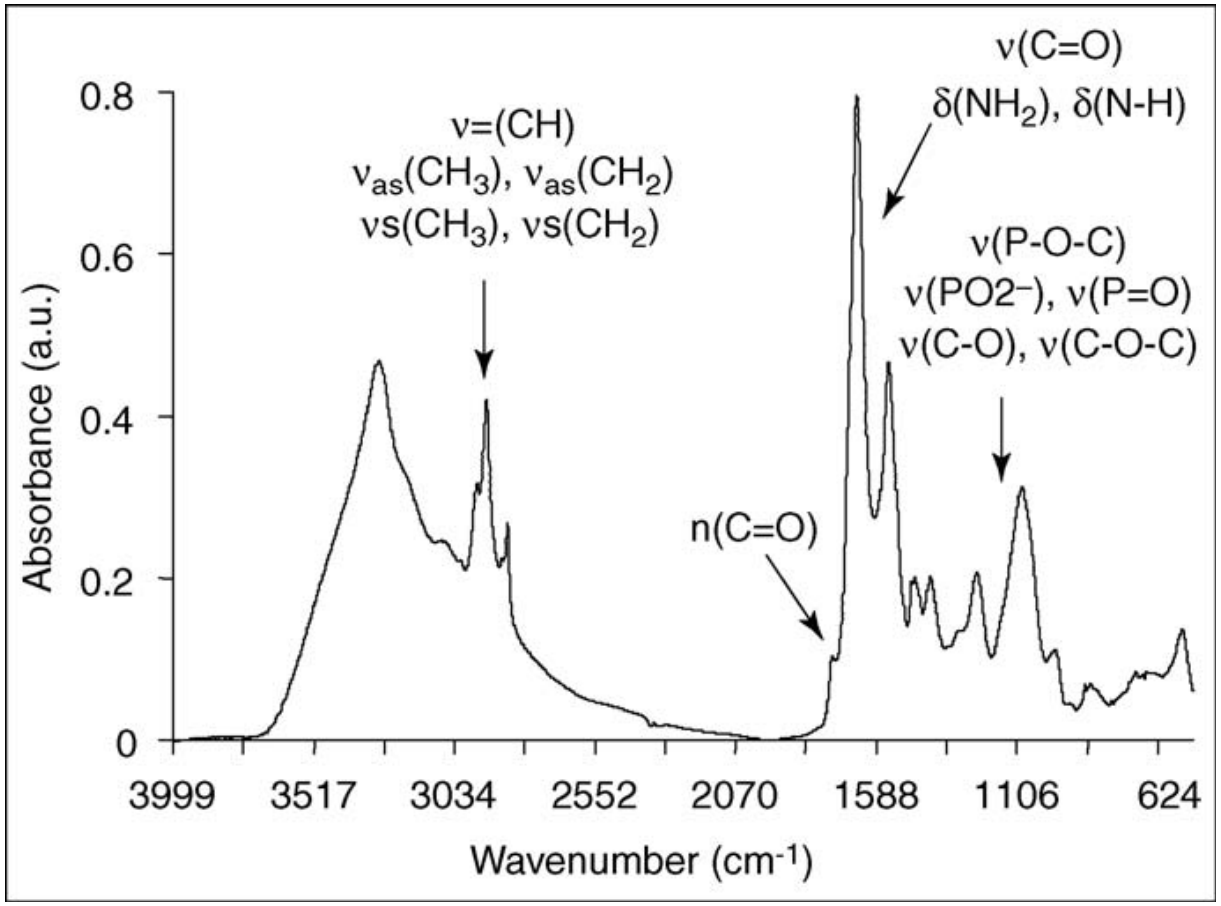

Figure 15. FTIR spectrum of U87 cells (human glioblastoma) expressed as arbitrary units (a.u.). The main infrared absorptions belonging to cellular contents are the ν-(–CH) of fatty acyl moieties, the C=O and N–H of amides, the NH_2 of amines, P–O and P=O of phosphate groups and C–O–C of sugars. (Based on Petibois et al. 2006) [140].

In biological tissues, FTIR spectra reveal absorbances corresponding to their chemical components. As an example of band assignments in a biological tissue: brain tissue is mainly composed of lipids (6–16%), proteins (9–11%), and water (70–83%) [141, 142]. FTIR spectra of brain samples are dominated by the amide I band at 1655 cm^{-1} and amide II band at 1545 cm^{-1} which arise from the C=O stretching and N–H bending vibrations, respectively, of the amide groups comprising the peptide linkages of proteins. Weaker protein absorptions include the amide III band at 1254 cm^{-1} and a number of peptide side chain vibrations that occur in the range between 1310 and 1470 cm^{-1}. At 1080 and 1240 cm^{-1} occur absorption bands due to

deoxyribose C–O and PO^{2-} groups of DNA [143]. White matter is known to have a high lipid and cholesterol content. Cholesterol exhibits IR bands at 1060 and 1382 cm^{-1} [141]. Intense IR bands of lipids are found at 1234 cm^{-1} (phosphodioxy groups), 1467 cm^{-1} (CH_2 bend), 1740 cm^{-1} (C=O stretch), and 2851 and 2920 cm^{-1} (CH_2 stretch), owing to the phospholipids, sphingomyelin, and glycolipids of the major white matter constituent myelin [144].

Several groups used infrared microscopy as a diagnostic tool to distinguish control from diseased cells or tissues. Numerous papers are devoted to the studies on cancerous disease, and subtle differences between normal and cancerous samples were detected. Infrared microscopy has also been applied in neuroscience. Several research papers to introduce the biomedical applications of FT-IR microscopy have been reported [133, 140, 141, 145-153]. Results obtained for various pathological states of human tissues are quite promising: changes in cell structure and composition can be visualized in the vibrational spectrum of a biological fluid or tissue even at an early stage of the disease. Thus, FTIR microscopy can join *ex vivo* clinical diagnostics, immunohistochemical analysis and histological determinations to set up a suitable protocol to study lesions in human tissues.

III.2.1. FTIR in cell biology

FTIR microscopy is becoming increasingly important for the study of cellular changes in various biological samples due to the molecular information provided. This powerful technique has been around for years but only now is becoming used in cell biology. Advances in high resolution FTIR microscopy may provide valuable new information on stem cells [154, 155]. It has been used to detect intracellular changes associated with diseases. It has also been used to study erythrocytes changes during exercise oxidative stress [138] and to analyze biochemical changes in tumor cells under stress conditions [150]. FTIR microscopy provides unique information about the structural and conformational changes of the molecules inside the cell in response to physiological or pathological stimuli. Studies of main biological molecules in individual cells with the use of FTIR means were previously applied to identification of changes that proceed during normal cell cycle or other processes like necrosis or apoptosis [156, 157]. Moreover, it has been proved that IR spectra is very informative

for taxonomical purposes concerning bacterial classification [158, 159], and other studies used FTIR spectroscopy for discrimination between diverse microbial species and strains on a routine basis [160, 161].

III.2.2. FTIR in histology

FTIR spectroscopy utilization may be envisaged as a tool for the detection of cancer over the traditional methods such as histopathologic analysis or others. The histological analysis of tissue samples by focusing on the bulk morphological features lacks quantitative accuracy and gives no account for the biochemical causality of the changes that occur during carcinogenesis. In comparison, IR spectroscopy may be a good alternative, being better than both of the histopathological or ultrasound examination (for ensuring high accuracy) and the computer tomography or X-ray transmission diagnosis (for being less expensive) [162]. Rather than using a stain- or immunoassay-based approach to histopathologic analysis, many researches focused to develop a spectroscopic imaging approach based on the chemical constitution of tissue.

As biological tissues contain same chemical components (proteins, nucleic acids, carbohydrates and lipids), their characteristic FTIR spectra are close but reveal small differences in specific absorbance features. Whereas chemical concentrations are quantified by spectral absorbance properties at specific vibrational frequencies, subtle molecular structural changes are indicated by spectral peak shifts, band shapes and relative intensity changes occurring across the vibrational spectrum [163]. Any changes in the body induced by diseases such as cancer are due to biochemical changes in one or all of these components. And since vibrational spectra are sensitive to the structure of these components, then they also change with the diseased state. For conventional methods, such as standard histological techniques, fluorescent probes and stains are required to display the spatial distribution of cellular and some biochemical components in tissue. Thus, quantification with these methods remains difficult. The use of FTIR imaging is exceptionally well suited for differentiating distinct tissue structures and for identifying tissue pathology. A series of works done by the group of Malins have demonstrated that highly sensitive statistical models of FTIR spectra are capable of identifying subtle differences in the

base and backbone structures of DNA in normal and abnormal tissues such as in prostate, ovary, and breast cancers [164-167]. Many other investigations have been focused on discriminating normal and malignant tissues at different sites such as stomach [168], cervical [169, 170], breast [146, 162], skin [171, 172], colon [148, 173], prostate [174-176] and lung [177]; or for studying tissue changes in other pathological conditions such for bone [178, 179], osteomalacia [180], and osteoarthritis [181].

However, if the FTIR technique for molecular assessing of tissue diagnosis has still not become an everyday tool in the hands of pathologists, it is that surgery and treatment of these diseases have already benefited dedicated developments from other high performance methods. It appears that FTIR imaging might play a role only for clinical applications where all other imaging modalities have already failed to provide accurate diagnostic results. This is the case for brain gliomas or prostate cancer, which have in common to be lethal for most of occurrences and present small size dimensions, i.e., a few mm^3 at early stage of the pathology. Since tissue composition is modified during carcinogenesis, the FTIR spectrum of cancerous tissue, as for glioma, will differ from that of the healthy tissue. Pathological changes associated with the development of brain tumor were investigated by FTIR imaging in many previous studies [143, 151, 182-184]. Most of these studies mentioned that structural changes were mainly related to qualitative and quantitative changes in lipids and they suggest that an increase in malignancy is accompanied by a reduction of total lipids relatively to other chemical species [151, 182, 184]. However, till now there is not a real clinical application of these studies that would allow help to define tumor edge during neurosurgery.

In summary, vibrational infrared spectro-imaging is a nondestructive photonic technique that provides a rapid measure of sample chemistry. Consequently, infrared spectral analyses have been used to study a wide variety of biomedical samples. There are three major aspects to the implementation of such an approach: 1- the rapid acquisition of high-fidelity microspectroscopic imaging data; 2- the development of robust algorithms to provide statistical controls over the classification process; and 3- the large-scale validation of the developed algorithms. The resultant FTIR vibrational microscopy or imaging can provide molecular information of samples with a high spatial resolution at microscopic level (e.g. the secondary structure of the proteins may be noninvasively measured in native environment). Thus, the use of this technique has extensively become a great potential over other diagnostic techniques for noninvasively investigating the chemical components of ultrastructual tissues at various disease states, due to the reagentless procedure and no dyes or labels addition for spectral determination. As compared with conventional histopathologic diagnosis, the micro-spectroscopic chemical information is supposed to be more objective and rapid. It not only provides more detailed spectral information of tissue (lipids, proteins, RNA/DNA, carbohydrates) for physicians, but also earlier predicts the diagnostic results of diseases.

FTIR imaging is a new tool for examining tissue sections, which does not require sample staining or fixation. In combination with advanced data processing techniques, this new approach has the potential to complement established strategies of tissue section diagnosis. Concordance between spectroscopic and clinical results opens the way for FTIR imaging to complement and support immunohistochemical and histological procedures, regarding the complexity of biological tissues. Nevertheless, chemical mapping by FTIR imaging may lead to an early and better understanding of chemical and morphological changes through the localization and characterization of pathological areas of a tissue. The possibility to detect molecular changes resulting from the initial pathological levels of a disease makes this technique a powerful tool for its accurate early diagnosis and prognosis.

In this research, Infrared spectro-imaging will be suggested as a tool in clinical and diagnostic analysis of glioma tissues to complement the existing methods because of its potential to probe tissue and cells at the molecular level. Compared to

routine imaging modalities, FTIR imaging advantages include that (i) it is rapid, as spectral data can be collected and interpreted within minutes by automated algorithms; (ii) it requires minimal sample preparation, as molecular vibrations probe the chemical composition and structural properties of tissue sections without external markers; and (iii) it is non-destructive, so the sample can be subjected to further analyses such as immunohistochemistry in order to confirm the findings.

Regarding the role of angiogenesis in gliomas, the limits of the imaging techniques for gliomas angiogenesis used nowadays, and the molecular information available through FTIR imaging data treatments, we performed this research to complement established histological techniques used for gliomas diagnosis. The most relevant parameters for discriminating between areas of tumor and healthy tissue are the following: (i) discriminating tumor versus healthy vasculature; (ii) determining changes in protein secondary structure of blood vessels during tumor growth; and (iii) evaluating oxidative stress effects on the fatty acyl chains of phospholipids. A combination of these parameters was envisaged to provide a more robust molecular histopathology prediction tool to study gliomas angiogenesis in different xenografted tumors as well as in human samples. **After the review of the literature, it is noteworthy to precise that for the first time FTIR imaging was used to study angiogenic blood capillaries in glioma tumors.**

Bibliography

1. Castro MG, Cowen R, Williamson IK, David A, Jimenez-Dalmaroni MJ, Yuan X, Bigliari A, Williams JC, Hu J & Lowenstein PR (2003) Current and future strategies for the treatment of malignant brain tumors. *Pharmacol Ther* **98**, 71-108.

2. Zukiel R, Nowak S, Barciszewska AM, Gawronska I, Keith G & Barciszewska MZ (2004) A simple epigenetic method for the diagnosis and classification of brain tumors. *Mol Cancer Res* **2**, 196-202.

3. Louis DN, Ohgaki H, Wiestler OD, Cavenee WK, Burger PC, Jouvet A, Scheithauer BW & Kleihues P (2007) The 2007 WHO classification of tumours of the central nervous system. *Acta neuropathologica* **114**, 97-109.

4. Dunn IF, Heese O & Black PM (2000) Growth factors in glioma angiogenesis: FGFs, PDGF, EGF, and TGFs. *J Neurooncol* **50**, 121-137.

5. Ichimura K, Ohgaki H, Kleihues P & Collins VP (2004) Molecular pathogenesis of astrocytic tumours. *J Neurooncol* **70**, 137-160.

6. Kleihues P, Louis DN, Scheithauer BW, Rorke LB, Reifenberger G, Burger PC & Cavenee WK (2002) The WHO classification of tumors of the nervous system. *Journal of neuropathology and experimental neurology* **61**, 215-225; discussion 226-219.

7. Surawicz TS, Davis F, Freels S, Laws ER, Jr. & Menck HR (1998) Brain tumor survival: results from the National Cancer Data Base. *J Neurooncol* **40**, 151-160.

8. Price SJ (2007) The role of advanced MR imaging in understanding brain tumour pathology. *British journal of neurosurgery* **21**, 562-575.

9. Essig M, Wenz F, Scholdei R, Bruning R, Berchtenbreiter C, Meurer M & Knopp MV (2002) Dynamic susceptibility contrast-enhanced echo-planar imaging of cerebral gliomas. Effect of contrast medium extravasation. *Acta Radiol* **43**, 354-359.

10. Miller JC, Pien HH, Sahani D, Sorensen AG & Thrall JH (2005) Imaging angiogenesis: applications and potential for drug development. *Journal of the National Cancer Institute* **97**, 172-187.

11. Berthelot T, Lasne MC & Deleris G (2008) New trends in molecular imaging of tumor angiogenesis. *Anti-cancer agents in medicinal chemistry* **8**, 497-522.

12. Choi SJ, Kim JS, Kim JH, Oh SJ, Lee JG, Kim CJ, Ra YS, Yeo JS, Ryu JS & Moon DH (2005) [18F]3'-deoxy-3'-fluorothymidine PET for the diagnosis and grading

of brain tumors. *European journal of nuclear medicine and molecular imaging* **32**, 653-659.

13. Price P (2001) PET as a potential tool for imaging molecular mechanisms of oncology in man. *Trends in molecular medicine* **7**, 442-446.

14. Mitchell P, Ellison DW & Mendelow AD (2005) Surgery for malignant gliomas: mechanistic reasoning and slippery statistics. *Lancet Neurol* **4**, 413-422.

15. Francis K, van Beek J, Canova C, Neal JW & Gasque P (2003) Innate immunity and brain inflammation: the key role of complement. *Expert reviews in molecular medicine* **5**, 1-19.

16. Jain RK, di Tomaso E, Duda DG, Loeffler JS, Sorensen AG & Batchelor TT (2007) Angiogenesis in brain tumours. *Nature reviews* **8**, 610-622.

17. Kacem K, Lacombe P, Seylaz J & Bonvento G (1998) Structural organization of the perivascular astrocyte endfeet and their relationship with the endothelial glucose transporter: a confocal microscopy study. *Glia* **23**, 1-10.

18. Balabanov R & Dore-Duffy P (1998) Role of the CNS microvascular pericyte in the blood-brain barrier. *Journal of neuroscience research* **53**, 637-644.

19. Vajkoczy P & Menger MD (2000) Vascular microenvironment in gliomas. *J Neurooncol* **50**, 99-108.

20. Carmeliet P & Jain RK (2000) Angiogenesis in cancer and other diseases. *Nature* **407**, 249-257.

21. Carmeliet P (2003) Angiogenesis in health and disease. *Nat Med* **9**, 653-660.

22. Alessi P, Ebbinghaus C & Neri D (2004) Molecular targeting of angiogenesis. *Biochim Biophys Acta* **1654**, 39-49.

23. Semenza GL (2007) Vasculogenesis, angiogenesis, and arteriogenesis: mechanisms of blood vessel formation and remodeling. *J Cell Biochem* **102**, 840-847.

24. Folkman J (1995) Angiogenesis inhibitors generated by tumors. *Molecular medicine (Cambridge, Mass* **1**, 120-122.

25. Carmeliet P (2005) Angiogenesis in life, disease and medicine. *Nature* **438**, 932-936.

26. Folkman J & Shing Y (1992) Angiogenesis. *J Biol Chem* **267**, 10931-10934.

27. Jain RK (2003) Molecular regulation of vessel maturation. *Nat Med* **9**, 685-693.

28. Wesseling P, Ruiter DJ & Burger PC (1997) Angiogenesis in brain tumors; pathobiological and clinical aspects. *J Neurooncol* **32**, 253-265.

29. Pepper MS (2001) Role of the matrix metalloproteinase and plasminogen activator-plasmin systems in angiogenesis. *Arteriosclerosis, thrombosis, and vascular biology* **21**, 1104-1117.

30. Rundhaug JE (2005) Matrix metalloproteinases and angiogenesis. *Journal of cellular and molecular medicine* **9**, 267-285.

31. Goodwin AM (2007) In vitro assays of angiogenesis for assessment of angiogenic and anti-angiogenic agents. *Microvasc Res* **74**, 172-183.

32. Bernardini G, Ribatti D, Spinetti G, Morbidelli L, Ziche M, Santoni A, Capogrossi MC & Napolitano M (2003) Analysis of the role of chemokines in angiogenesis. *Journal of immunological methods* **273**, 83-101.

33. Eccles SA (2004) Parallels in invasion and angiogenesis provide pivotal points for therapeutic intervention. *The International journal of developmental biology* **48**, 583-598.

34. Risau W (1997) Mechanisms of angiogenesis. *Nature* **386**, 671-674.

35. Kalluri R (2003) Basement membranes: structure, assembly and role in tumour angiogenesis. *Nat Rev Cancer* **3**, 422-433.

36. Morikawa S, Baluk P, Kaidoh T, Haskell A, Jain RK & McDonald DM (2002) Abnormalities in pericytes on blood vessels and endothelial sprouts in tumors. *The American journal of pathology* **160**, 985-1000.

37. Shepro D & Morel NM (1993) Pericyte physiology. *Faseb J* **7**, 1031-1038.

38. Jain RK & Booth MF (2003) What brings pericytes to tumor vessels? *The Journal of clinical investigation* **112**, 1134-1136.

39. Hanahan D & Folkman J (1996) Patterns and emerging mechanisms of the angiogenic switch during tumorigenesis. *Cell* **86**, 353-364.

40. Koch AE (1998) Review: angiogenesis: implications for rheumatoid arthritis. *Arthritis and rheumatism* **41**, 951-962.

41. Tolentino MJ & Adamis AP (1998) Angiogenic factors in the development of diabetic iris neovascularization and retinopathy. *International ophthalmology clinics* **38**, 77-94.

42. Folkman J (1990) What is the evidence that tumors are angiogenesis dependent? *Journal of the National Cancer Institute* **82**, 4-6.

43. Mundel TM & Kalluri R (2007) Type IV collagen-derived angiogenesis inhibitors. *Microvasc Res* **74**, 85-89.

44. Burri PH & Djonov V (2002) Intussusceptive angiogenesis--the alternative to capillary sprouting. *Molecular aspects of medicine* **23**, S1-27.

45. Fenton BM & Paoni SF (2003) Oxygenation and vascular perfusion in spontaneous and transplanted tumor models. *Advances in experimental medicine and biology* **530**, 165-176.

46. Folkman J (1992) The role of angiogenesis in tumor growth. *Semin Cancer Biol* **3**, 65-71.

47. Ferrara N, Gerber HP & LeCouter J (2003) The biology of VEGF and its receptors. *Nat Med* **9**, 669-676.

48. Hellstrom M, Gerhardt H, Kalen M, Li X, Eriksson U, Wolburg H & Betsholtz C (2001) Lack of pericytes leads to endothelial hyperplasia and abnormal vascular morphogenesis. *The Journal of cell biology* **153**, 543-553.

49. McDonald DM & Foss AJ (2000) Endothelial cells of tumor vessels: abnormal but not absent. *Cancer metastasis reviews* **19**, 109-120.

50. Jain RK (2005) Normalization of tumor vasculature: an emerging concept in antiangiogenic therapy. *Science (New York, NY* **307**, 58-62.

51. Hashizume H, Baluk P, Morikawa S, McLean JW, Thurston G, Roberge S, Jain RK & McDonald DM (2000) Openings between defective endothelial cells explain tumor vessel leakiness. *The American journal of pathology* **156**, 1363-1380.

52. Bottaro DP & Liotta LA (2003) Cancer: Out of air is not out of action. *Nature* **423**, 593-595.

53. Auguste P, Lemiere S, Larrieu-Lahargue F & Bikfalvi A (2005) Molecular mechanisms of tumor vascularization. *Crit Rev Oncol Hematol* **54**, 53-61.

54. Holash J, Maisonpierre PC, Compton D, Boland P, Alexander CR, Zagzag D, Yancopoulos GD & Wiegand SJ (1999) Vessel cooption, regression, and growth in tumors mediated by angiopoietins and VEGF. *Science (New York, NY* **284**, 1994-1998.

55. Leenders WP, Kusters B & de Waal RM (2002) Vessel co-option: how tumors obtain blood supply in the absence of sprouting angiogenesis. *Endothelium* **9**, 83-87.

56. Chang YS, di Tomaso E, McDonald DM, Jones R, Jain RK & Munn LL (2000) Mosaic blood vessels in tumors: frequency of cancer cells in contact with flowing blood. *Proc Natl Acad Sci U S A* **97**, 14608-14613.

57. Maniotis AJ, Folberg R, Hess A, Seftor EA, Gardner LM, Pe'er J, Trent JM, Meltzer PS & Hendrix MJ (1999) Vascular channel formation by human melanoma cells in vivo and in vitro: vasculogenic mimicry. *The American journal of pathology* **155**, 739-752.

58. Wesseling P, van der Laak JA, de Leeuw H, Ruiter DJ & Burger PC (1994) Quantitative immunohistological analysis of the microvasculature in untreated human glioblastoma multiforme. Computer-assisted image analysis of whole-tumor sections. *J Neurosurg* **81**, 902-909.

59. Plate KH & Risau W (1995) Angiogenesis in malignant gliomas. *Glia* **15**, 339-347.

60. Leon SP, Folkerth RD & Black PM (1996) Microvessel density is a prognostic indicator for patients with astroglial brain tumors. *Cancer* **77**, 362-372.

61. Tuettenberg J, Friedel C & Vajkoczy P (2006) Angiogenesis in malignant glioma--a target for antitumor therapy? *Crit Rev Oncol Hematol* **59**, 181-193.

62. Schlageter KE, Molnar P, Lapin GD & Groothuis DR (1999) Microvessel organization and structure in experimental brain tumors: microvessel populations with distinctive structural and functional properties. *Microvasc Res* **58**, 312-328.

63. Stewart PA, Farrell CL & Del Maestro RF (1991) The effect of cellular microenvironment on vessels in the brain. Part 1: Vessel structure in tumour, peritumour and brain from humans with malignant glioma. *International journal of radiation biology* **60**, 125-130.

64. Stewart PA (2000) Endothelial vesicles in the blood-brain barrier: are they related to permeability? *Cellular and molecular neurobiology* **20**, 149-163.

65. Chintala SK, Sawaya R, Gokaslan ZL, Fuller G & Rao JS (1996) Immunohistochemical localization of extracellular matrix proteins in human glioma, both in vivo and in vitro. *Cancer letters* **101**, 107-114.

66. Mahesparan R, Read TA, Lund-Johansen M, Skaftnesmo KO, Bjerkvig R & Engebraaten O (2003) Expression of extracellular matrix components in a highly infiltrative in vivo glioma model. *Acta neuropathologica* **105**, 49-57.

67. Carnemolla B, Castellani P, Ponassi M, Borsi L, Urbini S, Nicolo G, Dorcaratto A, Viale G, Winter G, Neri D & Zardi L (1999) Identification of a glioblastoma-associated tenascin-C isoform by a high affinity recombinant antibody. *The American journal of pathology* **154**, 1345-1352.

68. Rascher G, Fischmann A, Kroger S, Duffner F, Grote EH & Wolburg H (2002) Extracellular matrix and the blood-brain barrier in glioblastoma multiforme: spatial segregation of tenascin and agrin. *Acta Neuropathol (Berl)* **104**, 85-91.

69. Li C, Guo B, Bernabeu C & Kumar S (2001) Angiogenesis in breast cancer: the role of transforming growth factor beta and CD105. *Microscopy research and technique* **52**, 437-449.

70. Bian XW, Jiang XF, Chen JH, Bai JS, Dai C, Wang QL, Lu JY, Zhao W, Xin R, Liu MY, Shi JQ & Wang JM (2006) Increased angiogenic capabilities of endothelial cells from microvessels of malignant human gliomas. *Int Immunopharmacol* **6**, 90-99.

71. Hirano A, Kawanami T & Llena JF (1994) Electron microscopy of the blood-brain barrier in disease. *Microscopy research and technique* **27**, 543-556.

72. McDonald DM & Choyke PL (2003) Imaging of angiogenesis: from microscope to clinic. *Nat Med* **9**, 713-725.

73. Wesseling P, Schlingemann RO, Rietveld FJ, Link M, Burger PC & Ruiter DJ (1995) Early and extensive contribution of pericytes/vascular smooth muscle cells to microvascular proliferation in glioblastoma multiforme: an immuno-light and immuno-electron microscopic study. *Journal of neuropathology and experimental neurology* **54**, 304-310.

74. Benjamin LE, Golijanin D, Itin A, Pode D & Keshet E (1999) Selective ablation of immature blood vessels in established human tumors follows vascular endothelial growth factor withdrawal. *The Journal of clinical investigation* **103**, 159-165.

75. Eberhard A, Kahlert S, Goede V, Hemmerlein B, Plate KH & Augustin HG (2000) Heterogeneity of angiogenesis and blood vessel maturation in human tumors: implications for antiangiogenic tumor therapies. *Cancer Res* **60**, 1388-1393.

76. Neufeld G, Cohen T, Gengrinovitch S & Poltorak Z (1999) Vascular endothelial growth factor (VEGF) and its receptors. *Faseb J* **13**, 9-22.

77. Schmidt NO, Westphal M, Hagel C, Ergun S, Stavrou D, Rosen EM & Lamszus K (1999) Levels of vascular endothelial growth factor, hepatocyte growth factor/scatter factor and basic fibroblast growth factor in human gliomas and their relation to angiogenesis. *Int J Cancer* **84**, 10-18.

78. Vajkoczy P, Farhadi M, Gaumann A, Heidenreich R, Erber R, Wunder A, Tonn JC, Menger MD & Breier G (2002) Microtumor growth initiates angiogenic sprouting with simultaneous expression of VEGF, VEGF receptor-2, and angiopoietin-2. *The Journal of clinical investigation* **109**, 777-785.

79. Stratmann A, Risau W & Plate KH (1998) Cell type-specific expression of angiopoietin-1 and angiopoietin-2 suggests a role in glioblastoma angiogenesis. *The American journal of pathology* **153**, 1459-1466.

80. Bello L, Francolini M, Marthyn P, Zhang J, Carroll RS, Nikas DC, Strasser JF, Villani R, Cheresh DA & Black PM (2001) Alpha(v)beta3 and alpha(v)beta5 integrin expression in glioma periphery. *Neurosurgery* **49**, 380-389; discussion 390.

81. Joki T, Machluf M, Atala A, Zhu J, Seyfried NT, Dunn IF, Abe T, Carroll RS & Black PM (2001) Continuous release of endostatin from microencapsulated engineered cells for tumor therapy. *Nat Biotechnol* **19**, 35-39.

82. Peroulis I, Jonas N & Saleh M (2002) Antiangiogenic activity of endostatin inhibits C6 glioma growth. *Int J Cancer* **97**, 839-845.

83. Puduvalli VK & Sawaya R (2000) Antiangiogenesis -- therapeutic strategies and clinical implications for brain tumors. *J Neurooncol* **50**, 189-200.

84. Brooks PC, Silletti S, von Schalscha TL, Friedlander M & Cheresh DA (1998) Disruption of angiogenesis by PEX, a noncatalytic metalloproteinase fragment with integrin binding activity. *Cell* **92**, 391-400.

85. Bello L, Lucini V, Carrabba G, Giussani C, Machluf M, Pluderi M, Nikas D, Zhang J, Tomei G, Villani RM, Carroll RS, Bikfalvi A & Black PM (2001) Simultaneous inhibition of glioma angiogenesis, cell proliferation, and invasion by a naturally occurring fragment of human metalloproteinase-2. *Cancer Res* **61**, 8730-8736.

86. Bello L, Lucini V, Costa F, Pluderi M, Giussani C, Acerbi F, Carrabba G, Pannacci M, Caronzolo D, Grosso S, Shinkaruk S, Colleoni F, Canron X, Tomei G, Deleris G & Bikfalvi A (2004) Combinatorial administration of molecules that simultaneously inhibit angiogenesis and invasion leads to increased therapeutic efficacy in mouse models of malignant glioma. *Clin Cancer Res* **10**, 4527-4537.

87. Jansen M, de Witt Hamer PC, Witmer AN, Troost D & van Noorden CJ (2004) Current perspectives on antiangiogenesis strategies in the treatment of malignant gliomas. *Brain Res Brain Res Rev* **45**, 143-163.

88. Skobe M, Rockwell P, Goldstein N, Vosseler S & Fusenig NE (1997) Halting angiogenesis suppresses carcinoma cell invasion. *Nat Med* **3**, 1222-1227.

89. Zilberberg L, Shinkaruk S, Lequin O, Rousseau B, Hagedorn M, Costa F, Caronzolo D, Balke M, Canron X, Convert O, Lain G, Gionnet K, Goncalves M, Bayle M, Bello L, Chassaing G, Deleris G & Bikfalvi A (2003) Structure and inhibitory effects on angiogenesis and tumor development of a new vascular endothelial growth inhibitor. *J Biol Chem* **278**, 35564-35573.

90. Bikfalvi A (2004) Recent developments in the inhibition of angiogenesis: examples from studies on platelet factor-4 and the VEGF/VEGFR system. *Biochem Pharmacol* **68**, 1017-1021.

91. Jain RK (2001) Normalizing tumor vasculature with anti-angiogenic therapy: a new paradigm for combination therapy. *Nat Med* **7**, 987-989.

92. Tong RT, Boucher Y, Kozin SV, Winkler F, Hicklin DJ & Jain RK (2004) Vascular normalization by vascular endothelial growth factor receptor 2 blockade induces a pressure gradient across the vasculature and improves drug penetration in tumors. *Cancer Res* **64**, 3731-3736.

93. Winkler F, Kozin SV, Tong RT, Chae SS, Booth MF, Garkavtsev I, Xu L, Hicklin DJ, Fukumura D, di Tomaso E, Munn LL & Jain RK (2004) Kinetics of vascular normalization by VEGFR2 blockade governs brain tumor response to radiation: role of oxygenation, angiopoietin-1, and matrix metalloproteinases. *Cancer cell* **6**, 553-563.

94. Fukumura D & Jain RK (2007) Tumor microvasculature and microenvironment: targets for anti-angiogenesis and normalization. *Microvasc Res* **74**, 72-84.

95. Figarella-Branger D & Bouvier C (2005) [Histological classification of human gliomas: state of art and controversies]. *Bulletin du cancer* **92**, 301-309.

96. Figarella-Branger D, Colin C, Coulibaly B, Quilichini B, Maues De Paula A, Fernandez C & Bouvier C (2008) Classification histologique et moléculaire des gliomes. *Revue Neurologique* **164**, 505-515.

97. Arismendi-Morillo G & Castellano A (2005) Tumoral micro-blood vessels and vascular microenvironment in human astrocytic tumors. A transmission electron microscopy study. *J Neurooncol* **73**, 211-217.

98. Laking GR, West C, Buckley DL, Matthews J & Price PM (2006) Imaging vascular physiology to monitor cancer treatment. *Crit Rev Oncol Hematol* **58**, 95-113.

99. Pusztaszeri MP, Seelentag W & Bosman FT (2006) Immunohistochemical expression of endothelial markers CD31, CD34, von Willebrand factor, and Fli-1 in normal human tissues. *J Histochem Cytochem* **54**, 385-395.

100. Campbell RB, Fukumura D, Brown EB, Mazzola LM, Izumi Y, Jain RK, Torchilin VP & Munn LL (2002) Cationic charge determines the distribution of liposomes between the vascular and extravascular compartments of tumors. *Cancer Res* **62**, 6831-6836.

101. Hayashi K, Yamauchi K, Yamamoto N, Tsuchiya H, Tomita K, Amoh Y, Hoffman RM & Bouvet M (2007) Dual-color imaging of angiogenesis and its inhibition in bone and soft tissue sarcoma. *J Surg Res* **140**, 165-170.

102. Norrby K & Ridell B (2003) Tumour-type-specific capillary endothelial cell stainability in malignant B-cell lymphomas using antibodies against CD31, CD34 and Factor VIII. *Apmis* **111**, 483-489.

103. Kim S, Bell K, Mousa SA & Varner JA (2000) Regulation of angiogenesis in vivo by ligation of integrin alpha5beta1 with the central cell-binding domain of fibronectin. *The American journal of pathology* **156**, 1345-1362.

104. Bredow S, Lewin M, Hofmann B, Marecos E & Weissleder R (2000) Imaging of tumour neovasculature by targeting the TGF-beta binding receptor endoglin. *Eur J Cancer* **36**, 675-681.

105. Brekken RA, Huang X, King SW & Thorpe PE (1998) Vascular endothelial growth factor as a marker of tumor endothelium. *Cancer Res* **58**, 1952-1959.

106. Bogdanov A, Jr., Marecos E, Cheng HC, Chandrasekaran L, Krutzsch HC, Roberts DD & Weissleder R (1999) Treatment of experimental brain tumors with trombospondin-1 derived peptides: an in vivo imaging study. *Neoplasia (New York, NY* **1**, 438-445.

107. Lee WS, Jain MK, Arkonac BM, Zhang D, Shaw SY, Kashiki S, Maemura K, Lee SL, Hollenberg NK, Lee ME & Haber E (1998) Thy-1, a novel marker for

angiogenesis upregulated by inflammatory cytokines. *Circulation research* **82**, 845-851.

108. Chang SS, Reuter VE, Heston WD, Bander NH, Grauer LS & Gaudin PB (1999) Five different anti-prostate-specific membrane antigen (PSMA) antibodies confirm PSMA expression in tumor-associated neovasculature. *Cancer Res* **59**, 3192-3198.

109. Croix BS, Rago C, Velculescu V, Traverso G, Romans KE, Montgomery E, Lal A, Riggins GJ, Lengauer C, Vogelstein B & Kinzler KW (2000) Genes Expressed in Human Tumor Endothelium. *Science (New York, NY* **289**, 1197-1202.

110. Nehls V & Drenckhahn D (1991) Heterogeneity of microvascular pericytes for smooth muscle type alpha-actin. *The Journal of cell biology* **113**, 147-154.

111. Abramsson A, Berlin O, Papayan H, Paulin D, Shani M & Betsholtz C (2002) Analysis of mural cell recruitment to tumor vessels. *Circulation* **105**, 112-117.

112. Nehls V, Denzer K & Drenckhahn D (1992) Pericyte involvement in capillary sprouting during angiogenesis in situ. *Cell and tissue research* **270**, 469-474.

113. Alliot F, Rutin J, Leenen PJ & Pessac B (1999) Pericytes and periendothelial cells of brain parenchyma vessels co-express aminopeptidase N, aminopeptidase A, and nestin. *Journal of neuroscience research* **58**, 367-378.

114. Nielsen BS, Sehested M, Kjeldsen L, Borregaard N, Rygaard J & Dano K (1997) Expression of matrix metalloprotease-9 in vascular pericytes in human breast cancer. *Laboratory investigation; a journal of technical methods and pathology* **77**, 345-355.

115. Cho H, Kozasa T, Bondjers C, Betsholtz C & Kehrl JH (2003) Pericyte-specific expression of Rgs5: implications for PDGF and EDG receptor signaling during vascular maturation. *Faseb J* **17**, 440-442.

116. Kleihues P & Ohgaki H (2000) Phenotype vs genotype in the evolution of astrocytic brain tumors. *Toxicologic pathology* **28**, 164-170.

117. Walker C, Joyce KA, Thompson-Hehir J, Davies MP, Gibbs FE, Halliwell N, Lloyd BH, Machell Y, Roebuck MM, Salisbury J, Sibson DR, Du Plessis D, Broome J & Rossi ML (2001) Characterisation of molecular alterations in microdissected archival gliomas. *Acta neuropathologica* **101**, 321-333.

118. Dukor RK (2002) Vibrational Spectroscopy in the Detection of Cancer. In *The Handbook of Vibrational Spectroscopy* (Chalmers JM & Griffiths PR, ed^eds), pp. 3335 - 3361. Wiley, Chichester.

119. Lin S-Y, Li M-J & Cheng W-T (2007) FT-IR and Raman vibrational microspectroscopies used for spectral biodiagnosis of human tissues. *Spectroscopy* **21**, 1-30.

120. Silverstein R.M. BGC, Morrill Terence C. (1991) Infrared spectrometry. In *Spectrometric identification of organic compounds* (Wiley, ed^eds), pp. 91-164, New York.

121. Andrade PO, Bitar RA, Yassoyama K, Martinho H, Santo AM, Bruno PM & Martin AA (2007) Study of normal colorectal tissue by FT-Raman spectroscopy. *Anal Bioanal Chem* **387**, 1643-1648.

122. Baena JR & Lendl B (2004) Raman spectroscopy in chemical bioanalysis. *Current opinion in chemical biology* **8**, 534-539.

123. Bitar RA, Martinho Hda S, Tierra-Criollo CJ, Zambelli Ramalho LN, Netto MM & Martin AA (2006) Biochemical analysis of human breast tissues using Fourier-transform Raman spectroscopy. *J Biomed Opt* **11**, 054001.

124. Choo-Smith LP, Edwards HG, Endtz HP, Kros JM, Heule F, Barr H, Robinson JS, Jr., Bruining HA & Puppels GJ (2002) Medical applications of Raman spectroscopy: from proof of principle to clinical implementation. *Biopolymers* **67**, 1-9.

125. Crow P, Stone N, Kendall CA, Uff JS, Farmer JA, Barr H & Wright MP (2003) The use of Raman spectroscopy to identify and grade prostatic adenocarcinoma in vitro. *Br J Cancer* **89**, 106-108.

126. Kendall C, Stone N, Shepherd N, Geboes K, Warren B, Bennett R & Barr H (2003) Raman spectroscopy, a potential tool for the objective identification and classification of neoplasia in Barrett's oesophagus. *J Pathol* **200**, 602-609.

127. Krishna CM, Sockalingum GD, Bhat RA, Venteo L, Kushtagi P, Pluot M & Manfait M (2007) FTIR and Raman microspectroscopy of normal, benign, and malignant formalin-fixed ovarian tissues. *Anal Bioanal Chem* **387**, 1649-1656.

128. Yamazaki H, Kaminaka S, Kohda E, Mukai M & Hamaguchi HO (2003) The diagnosis of lung cancer using 1064-nm excited near-infrared multichannel Raman spectroscopy. *Radiation medicine* **21**, 1-6.

129. Choo-Smith LP, Maquelin K, van Vreeswijk T, Bruining HA, Puppels GJ, Ngo Thi NA, Kirschner C, Naumann D, Ami D, Villa AM, Orsini F, Doglia SM, Lamfarraj H, Sockalingum GD, Manfait M, Allouch P & Endtz HP (2001) Investigating microbial (micro)colony heterogeneity by vibrational spectroscopy. *Applied and environmental microbiology* **67**, 1461-1469.

130. Schlucker S, Schaeberle MD, Huffman SW & Levin IW (2003) Raman microspectroscopy: a comparison of point, line, and wide-field imaging methodologies. *Analytical chemistry* **75**, 4312-4318.

131. Krafft C, Kirsch M, Beleites C, Schackert G & Salzer R (2007) Methodology for fiber-optic Raman mapping and FTIR imaging of metastases in mouse brains. *Anal Bioanal Chem* **389**, 1133-1142.

132. Berger AJ, Koo TW, Itzkan I, Horowitz G & Feld MS (1999) Multicomponent blood analysis by near-infrared Raman spectroscopy. *Applied optics* **38**, 2916-2926.

133. Diem M, Romeo M, Boydston-White S, Miljkovic M & Matthaus C (2004) A decade of vibrational micro-spectroscopy of human cells and tissue (1994-2004). *Analyst* **129**, 880-885.

134. Anderson JC, Williams JC, Jr., Evan AP, Condon KW & Sommer AJ (2007) Analysis of urinary calculi using an infrared microspectroscopic surface reflectance imaging technique. *Urological research* **35**, 41-48.

135. C. Paluszkiewicz MG, lstrok & ka WKAPSW (1997) Renal stone studies using vibrational spectroscopy and trace element analysis. *Biospectroscopy* **3**, 403-407.

136. Ziegler CM, Kircher P & Hassfeld S (2002) Analysis of temporomandibular joint synovial fluid using Fourier transform/infrared spectroscopy. *Journal of Oral and Maxillofacial Surgery* **60**, 1302-1306.

137. Petibois C, Cazorla G, Gin H & Deleris G (2001) Differentiation of populations with different physiologic profiles by plasma Fourier-transform infrared spectra classification. *The Journal of laboratory and clinical medicine* **137**, 184-190.

138. Petibois C & Déléris G (2005) Evidence that erythrocytes are highly susceptible to exercise oxidative stress: FT-IR spectrometric studies at the molecular level. *Cell Biology International* **29**, 709-716.

139. Petibois C & Deleris G (2003) Stress-induced plasma volume change determined using plasma FT-IR spectra. *Applied spectroscopy* **57**, 396-399.

140. Petibois C & Deleris G (2006) Chemical mapping of tumor progression by FT-IR imaging: towards molecular histopathology. *Trends Biotechnol* **24**, 455-462.

141. Krafft C, Sobottka SB, Schackert G & Salzer R (2004) Analysis of human brain tissue, brain tumors and tumor cells by infrared spectroscopic mapping. *Analyst* **129**, 921-925.

142. Wolthuis R, van Aken M, Fountas K, Robinson JS, Jr., Bruining HA & Puppels GJ (2001) Determination of water concentration in brain tissue by Raman spectroscopy. *Analytical chemistry* **73**, 3915-3920.

143. Beleites C, Steiner G, Sowa MG, Baumgartner R, Sobottka S, Schackert G & Salzer R (2005) Classification of human gliomas by infrared imaging spectroscopy and chemometric image processing. *Vibrational Spectroscopy* **38**, 143-149.

144. Krafft C, Sobottka SB, Geiger KD, Schackert G & Salzer R (2007) Classification of malignant gliomas by infrared spectroscopic imaging and linear discriminant analysis. *Anal Bioanal Chem* **387**, 1669-1677.

145. Boskey AL & Mendelsohn R (2005) Infrared spectroscopic characterization of mineralized tissues. *Vib Spectrosc* **38**, 107-114.

146. Fabian H, Thi NA, Eiden M, Lasch P, Schmitt J & Naumann D (2006) Diagnosing benign and malignant lesions in breast tissue sections by using IR-microspectroscopy. *Biochim Biophys Acta* **1758**, 874-882.

147. Kneipp J, Beekes M, Lasch P & Naumann D (2002) Molecular changes of preclinical scrapie can be detected by infrared spectroscopy. *J Neurosci* **22**, 2989-2997.

148. Lasch P, Haensch W, Naumann D & Diem M (2004) Imaging of colorectal adenocarcinoma using FT-IR microspectroscopy and cluster analysis. *Biochim Biophys Acta* **1688**, 176-186.

149. Levin IW & Bhargava R (2005) Fourier transform infrared vibrational spectroscopic imaging: integrating microscopy and molecular recognition. *Annual review of physical chemistry* **56**, 429-474.

150. Petibois C, Drogat B, Bikfalvi A, Deleris G & Moenner M (2007) Histological mapping of biochemical changes in solid tumors by FT-IR spectral imaging. *FEBS letters* **581**, 5469-5474.

151. Steiner G, Shaw A, Choo-Smith LP, Abuid MH, Schackert G, Sobottka S, Steller W, Salzer R & Mantsch HH (2003) Distinguishing and grading human gliomas by IR spectroscopy. *Biopolymers* **72**, 464-471.

152. Szczerbowska-Boruchowska M, Dumas P, Kastyak MZ, Chwiej J, Lankosz M, Adamek D & Krygowska-Wajs A (2007) Biomolecular investigation of human substantia nigra in Parkinson's disease by synchrotron radiation Fourier transform infrared microspectroscopy. *Archives of biochemistry and biophysics* **459**, 241-248.

153. Wetzel DL & LeVine SM (1999) Imaging molecular chemistry with infrared microscopy. *Science (New York, NY* **285**, 1224-1225.

154. Ami D, Neri T, Natalello A, Mereghetti P, Doglia SM, Zanoni M, Zuccotti M, Garagna S & Redi CA (2008) Embryonic stem cell differentiation studied by FT-IR spectroscopy. *Biochim Biophys Acta* **1783**, 98-106.

155. Krafft C, Salzer R, Seitz S, Ern C & Schieker M (2007) Differentiation of individual human mesenchymal stem cells probed by FTIR microscopic imaging. *Analyst* **132**, 647-653.

156. Holman HY, Martin MC, Blakely EA, Bjornstad K & McKinney WR (2000) IR spectroscopic characteristics of cell cycle and cell death probed by synchrotron radiation based Fourier transform IR spectromicroscopy. *Biopolymers* **57**, 329-335.

157. Mourant JR, Yamada YR, Carpenter S, Dominique LR & Freyer JP (2003) FTIR spectroscopy demonstrates biochemical differences in mammalian cell cultures at different growth stages. *Biophysical journal* **85**, 1938-1947.

158. AMIEL Caroline ML, DENIS Catherine, & PICHON Patricia TJ (2001) FTIR spectroscopy and taxonomic purpose: Contribution to the classification of lactic acid bacteria. *Lait* **81**, 249-255.

159. Melin A. PA, and Deleris G. (2001) Effect of Radical Attack on Bacteria: An Application of FT-IR Spectroscopy. *Appl Spectrosc* **55**, 23-28.

160. Preisner O, Lopes JA, Guiomar R, Machado J & Menezes JC (2007) Fourier transform infrared (FT-IR) spectroscopy in bacteriology: towards a reference method for bacteria discrimination. *Anal Bioanal Chem* **387**, 1739-1748.

161. Sandt C, Madoulet C, Kohler A, Allouch P, De Champs C, Manfait M & Sockalingum GD (2006) FT-IR microspectroscopy for early identification of some clinically relevant pathogens. *Journal of applied microbiology* **101**, 785-797.

162. Eckel R, Huo H, Guan H-W, Hu X, Che X & Huang W-D (2001) Characteristic infrared spectroscopic patterns in the protein bands of human breast cancer tissue. *Vibrational Spectroscopy* **27**, 165-173.

163. Fernandez DC, Bhargava R, Hewitt SM & Levin IW (2005) Infrared spectroscopic imaging for histopathologic recognition. *Nat Biotechnol* **23**, 469-474.

164. Malins DC, Anderson KM, Gilman NK, Green VM, Barker EA & Hellstrom KE (2004) Development of a cancer DNA phenotype prior to tumor formation. *Proc Natl Acad Sci U S A* **101**, 10721-10725.

165. Malins DC, Gilman NK, Green VM, Wheeler TM, Barker EA, Vinson MA, Sayeeduddin M, Hellstrom KE & Anderson KM (2004) Metastatic cancer DNA phenotype identified in normal tissues surrounding metastasizing prostate carcinomas. *Proc Natl Acad Sci U S A* **101**, 11428-11431.

166. Malins DC, Polissar NL & Gunselman SJ (1996) Progression of human breast cancers to the metastatic state is linked to hydroxyl radical-induced DNA damage. *Proc Natl Acad Sci U S A* **93**, 2557-2563.

167. Malins DC, Polissar NL, Schaefer S, Su Y & Vinson M (1998) A unified theory of carcinogenesis based on order-disorder transitions in DNA structure as studied in the human ovary and breast. *Proc Natl Acad Sci U S A* **95**, 7637-7642.

168. Wang TD, Triadafilopoulos G, Crawford JM, Dixon LR, Bhandari T, Sahbaie P, Friedland S, Soetikno R & Contag CH (2007) Detection of endogenous biomolecules in Barrett's esophagus by Fourier transform infrared spectroscopy. *Proc Natl Acad Sci U S A* **104**, 15864-15869.

169. Cohenford MA & Rigas B (1998) Cytologically normal cells from neoplastic cervical samples display extensive structural abnormalities on IR spectroscopy: implications for tumor biology. *Proc Natl Acad Sci U S A* **95**, 15327-15332.

170. Neviliappan S, Fang Kan L, Tiang Lee Walter T, Arulkumaran S & Wong PT (2002) Infrared spectral features of exfoliated cervical cells, cervical adenocarcinoma tissue, and an adenocarcinoma cell line (SiSo). *Gynecol Oncol* **85**, 170-174.

171. Crupi V, De Domenico D, Interdonato S, Majolino D, Maisano G, Migliardo P & Venuti V (2001) FT-IR spectroscopy study on cutaneous neoplasie. *Journal of Molecular Structure* **563-564**, 115-118.

172. Pouliot R, Germain L, Auger FA, Tremblay N & Juhasz J (1999) Physical characterization of the stratum corneum of an in vitro human skin equivalent produced by tissue engineering and its comparison with normal human skin by ATR-FTIR spectroscopy and thermal analysis (DSC). *Biochim Biophys Acta* **1439**, 341-352.

173. Salman A, Argov S, Ramesh J, Goldstein J, Sinelnikov I, Guterman H & Mordechai S (2001) FT-IR microscopic characterization of normal and malignant human colonic tissues. *Cellular and molecular biology (Noisy-le-Grand, France)* **47 Online Pub**, OL159-166.

174. Gazi E, Baker M, Dwyer J, Lockyer NP, Gardner P, Shanks JH, Reeve RS, Hart CA, Clarke NW & Brown MD (2006) A correlation of FTIR spectra derived from prostate cancer biopsies with gleason grade and tumour stage. *European urology* **50**, 750-760; discussion 760-751.

175. Li MJ, Hsu HS, Liang RC & Lin SY (2002) Infrared microspectroscopic detection of epithelial and stromal growth in the human benign prostatic hyperplasia. *Ultrastruct Pathol* **26**, 365-370.

176. Malins DC, Johnson PM, Barker EA, Polissar NL, Wheeler TM & Anderson KM (2003) Cancer-related changes in prostate DNA as men age and early identification of metastasis in primary prostate tumors. *Proc Natl Acad Sci U S A* **100**, 5401-5406.

177. Yang Y, Sule-Suso J, Sockalingum GD, Kegelaer G, Manfait M & El Haj AJ (2005) Study of tumor cell invasion by Fourier transform infrared microspectroscopy. *Biopolymers* **78**, 311-317.

178. Boskey A & Mendelsohn R (2005) Infrared analysis of bone in health and disease. *J Biomed Opt* **10**, 031102.

179. Camacho NP, Rinnerthaler S, Paschalis EP, Mendelsohn R, Boskey AL & Fratzl P (1999) Complementary information on bone ultrastructure from scanning small angle X-ray scattering and Fourier-transform infrared microspectroscopy. *Bone* **25**, 287-293.

180. Faibish D, Gomes A, Boivin G, Binderman I & Boskey A (2005) Infrared imaging of calcified tissue in bone biopsies from adults with osteomalacia. *Bone* **36**, 6-12.

181. David-Vaudey E, Burghardt A, Keshari K, Brouchet A, Ries M & Majumdar S (2005) Fourier Transform Infrared Imaging of focal lesions in human osteoarthritic cartilage. *European cells & materials* **10**, 51-60; discussion 60.

182. Amharref N, Beljebbar A, Dukic S, Venteo L, Schneider L, Pluot M, Vistelle R & Manfait M (2006) Brain tissue characterisation by infrared imaging in a rat glioma model. *Biochim Biophys Acta* **1758**, 892-899.

183. Bambery KR, Schultke E, Wood BR, Rigley MacDonald ST, Ataelmannan K, Griebel RW, Juurlink BH & McNaughton D (2006) A Fourier transform infrared microspectroscopic imaging investigation into an animal model exhibiting glioblastoma multiforme. *Biochim Biophys Acta* **1758**, 900-907.

184. Krafft C, Thummler K, Sobottka SB, Schackert G & Salzer R (2006) Classification of malignant gliomas by infrared spectroscopy and linear discriminant analysis. *Biopolymers* **82**, 301-305.


PART II
Results & Discussion

Paper I

- PAPER 1-

Analysis of type I and IV collagens by FT-IR spectroscopy and imaging for a molecular investigation of skeletal muscle connective tissue

---

Anal Bioanal Chem (2006) 386:1961–1966.

Purpose: The aim of this study was to show that FT-IR spectroscopy and imaging are relevant techniques for studying biological tissue molecular contents, notably for its connective part. Type I and IV collagens (tI-C and tIV-C, respectively) were analyzed by FT-IR spectroscopy to determine the differences in secondary structure of these proteins. FT-IR imaging of skeletal muscle tissue sections was then used for comparing perimysium and endomysium collagen types, which are known to be mainly tI-C and tIV-C, respectively. This tissue model was chosen because of the ease morphological recognition of these connective tissue parts.

Main results: Secondary structure of collagen types was determined by using their secondary derivative spectrum for determining the position of absorption bands within the amide I spectral interval (1700-1600 cm^{-1}) and the curve-fitting of this one for determining every band absorption (spectral area, in squared a.u. of FTIR spectrum). Eight absorption bands could be determined on series of pure product FTIR spectra of types I and IV collagens, with α-helix (1,656 cm^{-1}), β-sheet (added 1,691; 1,679; and 1,626 cm^{-1}), β-turn (added 1,669 and 1,608 cm^{-1}), triple helix (1,638 cm^{-1}), and unordered structure (1,647 cm^{-1}). Type I collagen could be differentiated from type IV by its higher amounts of triple helix and α-helix, and lower amount of β-sheets ($P<0.01$). FT-IR imaging was then used to determine structural features of perimysium and endomysium collagen network in bovine flexor *carpi radialis* muscle. Secondary structure of proteins contained in perimysium and endomysium was found to be highy correlated to type I and IV collagens, respectively. FT-IR spectroscopy

and imaging are thus analytical tools that might be used for investigating biodistribution and assembly of collagen types in tissues.

Conclusion: This study has shown that type I and IV collagens may be differentiated by using several secondary structure parameters revealed by the curve-fitting of the amide I spectral interval of FT-IR spectra. Moreover, FT-IR imaging allows differentiation of the main connective tissue compartments of skeletal muscle, perimysium and endomysium, on the basis of these collagen types secondary structure parameters. These perspectives open the route to a functional FT-IR imaging of tissues on the basis of molecular features considered as characteristic of a given physiological situation (e.g., pathology or necrosis), which may be named a molecular histopathology.

Contribution to a "molecular histology of brain glioma": The extracellular matrix (ECM) provides necessary contacts between endothelial cells (ECs) and the surrounding tissue, and thus prevents blood vessels from collapsing. At their native state, i.e., when vessels are quiescent, their basement membrane is mainly made of of collagen IV, laminin, and other components surround the vascular cells; pericytes and ECs are even embedded in the same basement membrane. An interstitial matrix of collagen I and elastin between vascular cells further provides visco-elasticity and strength to the vessel wall. The ECM also regulates the formation of new vessel sprouts. Thus, the idea is to study collagen type contents within the vascular basement membrane of healthy and tumor blood capillaries by FT-IR spectroscopy with the aim of determining the morphological limits of gliomas.

Anal Bioanal Chem (2006) 386:1961–1966
DOI 10.1007/s00216-006-0828-0

ORIGINAL PAPER

Analysis of type I and IV collagens by FT-IR spectroscopy and imaging for a molecular investigation of skeletal muscle connective tissue

Cyril Petibois · Gilles Gouspillou · Katia Wehbe · Jean-Paul Delage · Gérard Déléris

Received: 28 July 2006 / Revised: 26 August 2006 / Accepted: 1 September 2006 / Published online: 17 October 2006

Abstract Many muscular diseases result from abnormal organization of connective tissue and/or collagen network formation. Only a few molecular imaging techniques are able to analyze this collagen network by differentiating collagen types. In this study, FT-IR spectroscopy was used to analyze type I and IV collagens, the most important compounds of which are perimysium and endomysium, respectively. Secondary structure of collagen types was determined by curve-fitting the 1,700–1,480 cm^{-1} spectral interval. Type I collagen could be differentiated from type IV by its higher amounts of triple helix and α-helix, but lower amounts of β-sheets ($P<0.01$). FT-IR imaging was then used to determine structural features of perimysium and endomysium collagen network in bovine *Flexor carpi radialis* muscle. Secondary structure of proteins contained in perimysium and endomysium was found to be very close to type I and IV collagens, respectively. FT-IR spectroscopy and imaging are thus analytical tools that might be used for investigating biodistribution and assembly of collagen types in connective tissues.

Keywords FT-IR imaging · Skeletal muscle · Collagen · Perimysium · Endomysium

C. Petibois (✉) · G. Gouspillou · K. Wehbe · G. Déléris
CNRS UMR 5084, CNAB, Bio-Organic Chemistry Group,
Université Victor Segalen Bordeaux 2,
146 rue Léo Saignat,
33076 Bordeaux Cedex, France
e-mail: cyril.petibois@u-bordeaux2.fr

G. Gouspillou · J.-P. Delage
INSERM U688 Physiopathologie Mitochondriale,
Université Victor Segalen Bordeaux 2,
146 rue Léo Saignat,
33076 Bordeaux Cedex, France

Abbreviations

ECM	extracellular matrix
FT-IR	Fourier-transform infrared
IMCT	intramuscular connective tissue
tI-C	type I collagen
tIV-C	type IV collagen

Introduction

Abnormal formation of skeletal muscle connective tissue is presumed to initiate a wide range of debilitating diseases, such as dystrophies [1], fibrosis [2], rhabdomyosarcoma [3], and most myopathies [4]. In such pathologies, the extracellular matrix (ECM) plays a fundamental role, both in structural and functional aspects of skeletal muscle. The two main components of the ECM are the endomysium and the perimysium. The endomysium is made of a continuous sheet covering the full length of myofibers until the myotendinous junction. It is organized as a regular network of thin collagen fibers composed mostly of type IV (tIV-C), as well as types III, VI, and XII to a minor extent. This network attaches myofibers sarcolemma to specific transmembrane proteins, thereby forming a regular mosaic pattern. In contrast, the perimysium is formed by an alveolar network of crimped collagen fibers varying in diameter and composition, including essentially type I collagen (tI-C) in conjunction with small amounts of types III, VI, and XII. Thus, perimysium and endomysium network formation within skeletal muscle may be analyzed through the respective biodistributions of tI-C and tIV-C [5, 6].

However, to date, only a few analytical methods are able to provide information about collagen biodistribution, assembly, and typology [5]. The spatial distribution of the

intramuscular connective tissue (IMCT) is usually examined by using histology and magnetic resonance imaging, but these techniques do not provide a spatial resolution allowing the study of collagen network organization [7]. Among ex vivo diagnostic methods, Fourier-transform infrared (FT-IR) spectroscopy and spectro-imaging emerged and developed rapidly during the last decade [8]. The FT-IR technique is based on the absorption of infrared light by vibrational transitions in covalent bonds. The intensities provide quantitative information about sample contents, since frequencies relate to the nature of molecular bonds, their structure, and their environment. In complex systems such as cells, an infrared spectrum is the sum of the contributions gathered from the proteins, lipids, nucleic acids, and metabolic parameters present. The spectra can be used as signatures if spectral patterns are correlated with biological properties. Useful diagnostic information has been extracted from infrared spectra in the case of different pathologies [9–11], but this technique is not yet recognize as a powerful diagnostic tool. Right now, the main successes of FT-IR spectroscopy have been bacteria identification [12], recognition of molecular structure [13], and molecular concentrations determination within biological fluids [14, 15]. One of the advantages of the FT-IR spectroscopy approach is that a spectrum is representative of all the cell constituents and may be recorded within a few seconds. A recent technical advance has been the development of imaging systems able to provide fast FT-IR images of tissues, and only a few minutes are now required to obtain a functional FT-IR image of a 1-mm^2 tissue area. Therefore, as a molecular probe of tissue composition, FT-IR imaging may favorably help histopathology in detecting and diagnosing diseases, notably small-sized and/or diffuse tumors, which are undetectable using the MRI or PET imaging techniques in vivo [16, 17].

The aim of this study was to show that FT-IR imaging may be considered as a useful tool for the functional molecular imaging of skeletal muscle connective tissue. tI-C and tIV-C were analyzed by FT-IR spectroscopy to determine secondary structure differences between proteins. FT-IR imaging of skeletal muscle tissue sections was then used to determine tI-C and tIV-C biodistribution within the connective tissue collagen network.

Methods

Reference collagen FT-IR spectra

The tissue the most concentrated in type I collagen (>90%) is the tail of male Wistar rat [18] and thus may be used to analyze this protein secondary structure. A series of thin fibers were removed from the rat tail for FT-IR spectra acquisitions. Fibers were laid down flat on a ZnSe window (25-mm diameter; 2-mm thickness) before desiccation in a moderate drying vacuum to evaporate residual water (2 h). Pure product (>95%) type IV collagen was purchased from Sigma-Aldrich (Ref. product: C5533). Type IV collagen solution was deposited on a series of ZnSe windows before desiccation to obtain reproducible dry films. All spectra were obtained by using a Spotlight 300 imaging system, equipped with a Spectrum One spectrometer (Perlin-Elmer, France). For FT-IR spectra acquisition, the imaging system was used in spectroscopy point mode (aperture of 100× 100 μm), with a 4.0 cm^{-1} resolution, and acquisitions were performed using 60 scans in transmittance mode. All experiments were performed in triplicate and FT-IR spectra were averaged before data treatments (n=10 averaged spectra for each collagen type).

Tissue FT-IR imaging

All procedures were performed in accordance with institutional guidelines for animal care. The *Flexor carpi radialis* muscles of the foreleg were taken from different cows, just after slaughter, and immediately frozen. Frozen tissue was laid down flat on cooled glue (poly(vinyl alcohol) for cryostat, −20 °C) to avoid tissue embedding. Tissue deposition on sample holder was arranged in order that fibers present vertically to the blade at sectioning. Additional glue was used to homogenize the sample intended for cryosections (Cryostat 3050-TM, Leica-Microsystems, France). A series of 16-μm-thick sections were used for FT-IR analyses using the Spotlight 300 FT-IR imaging system (Perkin-Elmer, France). Transmittance FT-IR spectra were obtained in image mode (6.25-μm pixels) and using 8 scans (4,000–700 cm^{-1}) and a 4 cm^{-1} resolution. A total of 10 tissue sections were used for statistical data treatments.

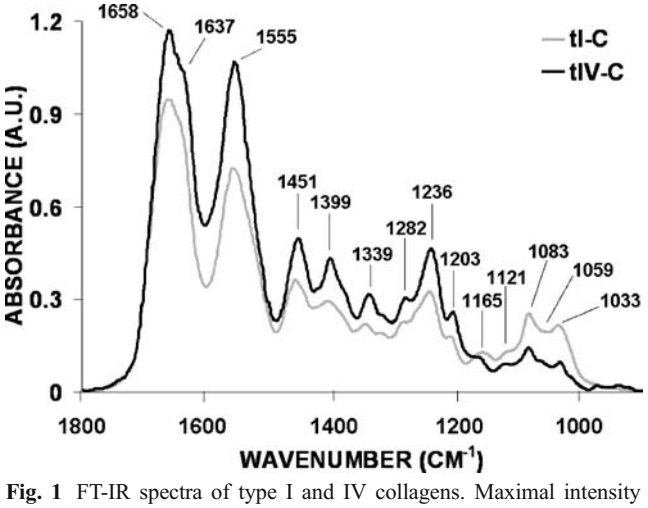

Fig. 1 FT-IR spectra of type I and IV collagens. Maximal intensity absorptions are revealed by the peak-picking sub-routine of Opus 4.2 software (Bruker, Germany) with a sensitivity of 1%

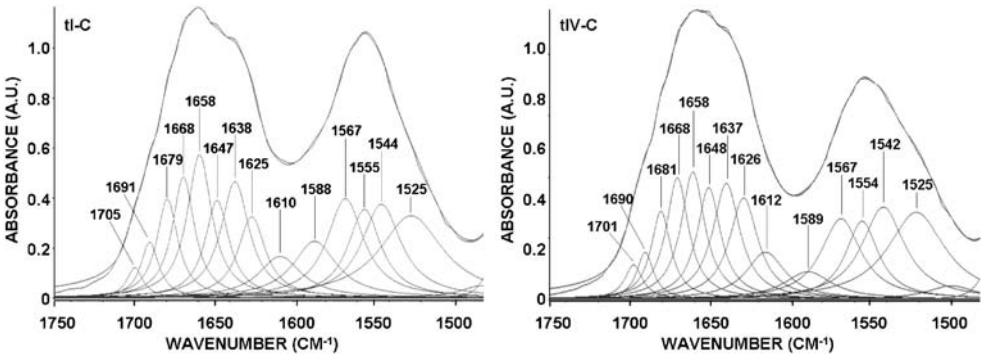

Fig. 2 Spectral curve-fitting of type I (*left*) and IV (*right*) collagens for the 1,750–1,400 cm^{-1} spectral interval. Absorption bands of amide I are used for secondary structure calculation (Table 1)

Spectral curve-fitting

Curve-fitting of collagen FT-IR spectra was performed as previously described [19], using a sub-routine of Opus 4.2 software (Bruker, Germany). Briefly, the 1,750–1,400 cm^{-1} spectral interval was used to determine secondary structure of collagen protein. To avoid the usual confounding effects of self curve-fitting, where absorption band positions may vary a lot, absorption bands were fixed for all FT-IR spectra according to previous studies [13, 20–22]. The percentage of Gaussian and Lorentzian functions for every absorption band was first determined from the series of pure product spectra of collagen. Thirteen absorption bands of amides I and II were found in the 1,700–1,480 cm^{-1} spectral interval of plasma FT-IR spectra. Secondly, bandwidth and absorption line shape fixed for these 13 bands were applied to determine collagen absorptions on skeletal muscle tissue FT-IR images. Free parameters in fitting procedure were also added at 1,750 and 1,400 cm^{-1} to avoid anomalous band additions at the limits of the selected spectral interval. In this way, secondary structure absorption bands of collagen were not modified by the bands that could not be correctly determined at the limits of the spectral interval selected. According to literature [8, 13, 19–21, 23, 24], secondary structure calculation was performed using amide I bands as follows: α-helix (ca. 1,656 cm^{-1}), β-sheet (added ca. 1,691, 1,679, and 1,626 cm^{-1}), β-turn (added ca. 1,669 and 1,608 cm^{-1}), triple helix (ca. 1,638 cm^{-1}), and unordered structure (ca. 1,647 cm^{-1}). Secondary structure parameters were expressed as percentage of total amide I absorption.

Statistics

Results are presented as means±SD. Differences between series of data were determined by using the Student t-test. Confidence limit was set at 1 or 5% ($P<0.01$ or 0.05) as indicated in text or tables.

Results and discussion

FT-IR spectra of type I and IV collagens

FT-IR spectra from tI-C and tIV-C are presented in Fig. 1. Peak picking was performed on the 1,800–900 cm^{-1} spectral interval for comparison with literature [13, 20, 25–29]. Both types of collagen exhibited absorptions at 1,033, 1,059, and 1,083 cm^{-1}, which arise from the C–OH stretching vibrations of the carbohydrate moieties attached to the protein [29]. Absorption features at 1,451, 1,399, 1,339, 1,282, 1,236, and 1,203 cm^{-1} are attributed to CH_2 and CH_3 wagging and deformation, and C–N stretching of collagen [4]. Amides I and II absorptions were revealed at 1,658 and 1,555 cm^{-1} and the shoulder appearing at 1,637 cm^{-1} could be attributed to the triple helix absorption of collagens [27]. Both tI-C and tIV-C exhibited very similar absorptions although one could notice that tI-C presented higher intensities for the 1,100–1,000 cm^{-1} spectral interval.

To analyze secondary structure of proteins, amide band absorptions were determined by curve-fitting the 1,750–1,480 cm^{-1} spectral interval (Fig. 2). All amide I absorption bands could be determined on every spectrum ($n=10$ for

Table 1 Secondary structure calculation from tI-C and tIV-C FT-IR spectra

	α-helix	Triple helix	β-sheets	β-turns	Unordered
tI-C	18.6±0.9	17.7±0.4	27.7±1.1	24.4±0.7	11.6±0.9
tIV-C	15.6±0.6**	15.7±1.0*	31.7±2.5*	25.0±1.2	12.0±1.9

*Significantly different from tI-C, $P<0.05$; **$P<0.01$. Absorption bands used for secondary structure calculation: α-helix (ca. 1,656 cm^{-1}), β-sheet (ca. 1,691, 1,679, and 1,626 cm^{-1}), β-turn (ca. 1,669 and 1,608 cm^{-1}), triple helix (ca. 1,638 cm^{-1}), and unordered structure (ca. 1,647 cm^{-1}). $n=10$ spectra for each protein

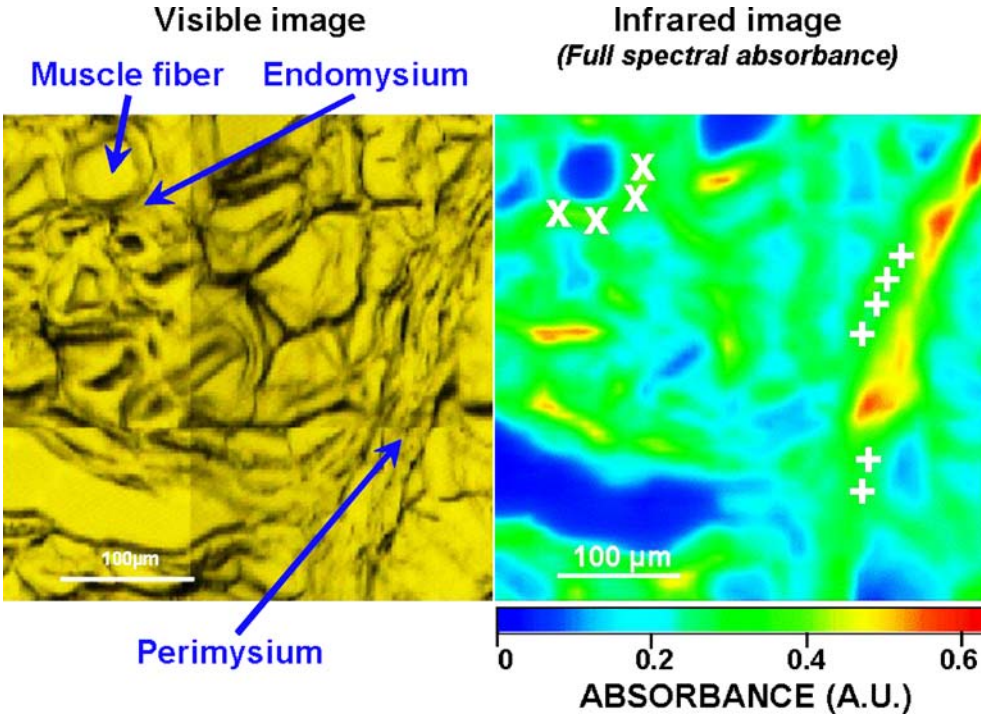

Fig. 3 Visible (*left*) and full spectral FT-IR (*right*) images of skeletal muscle tissue section (16 µm) exhibiting a vertical arrangement of fibers. + and × in FT-IR image show selected positions to obtain FT-IR spectra of perimysium and endomysium, respectively

each collagen type) with no more than 2 cm^{-1} shift at maximal intensities. As previously described in the literature [8, 13, 20–22], absorption features could be attributed as follows: ca. 1,690 cm^{-1} (parallel β-sheets), ca. 1,680 cm^{-1} (anti-parallel β-sheets), ca. 1,668 cm^{-1} (β-turns), ca. 1,658 cm^{-1} (α-helix), ca. 1,647 cm^{-1} (unordered), 1,638 cm^{-1} (triple helix), ca. 1625 cm^{-1} (parallel β-sheets), and ca. 1,612 cm^{-1} (β-turns). It was found that both tI-C and tIV-C exhibited very close absorptions, which only varied significantly in intensity. Spectral area per band was used for secondary structure calculation. Absorption bands belonging to β-sheets (3 bands) or β-turns (2 bands) were added. As described in Table 1, it was found that tI-C presented significantly higher α-helix and triple helix contents than tIV-C, while β-sheet content was lower ($P<0.05$). Contents in β-turns and unordered structure were found similar between collagen types. This higher content in α-helix and triple helix for tI-C could be explained by the lack of globular domains in the protein. As a consequence, the relative amount of α-helix and triple helix is increased in tI-C, while the amount of β-sheets is lowered [30, 31]. The results obtained in this study show for the first time that spectral curve-fitting allows differentiation of collagen types on the basis of their secondary structure. Further studies might be envisaged for differentiating other collagen types (e.g., type VI), which notably play a role in pathologies implying connective tissue alterations [5]. This differentiation of collagen types is also the basis of a functional infrared imaging of connective tissue in skeletal muscle, since endomysium and perimysium are mostly composed of tIV-C and tI-C, respectively [5, 6].

FT-IR images of skeletal muscle tissue

An example of tissue analysis by FT-IR imaging is provided in Fig. 3. Once a tissue section was found to present skeletal muscle fibers arranged in the vertical plan, an area in which perimysium and endomysium could be distinguished was selected to perform visible and FT-IR image acquisitions. Typically, 400×400-µm tissue areas could be analyzed in 6–8 min. As shown in Fig. 3, 4 to 6 spectra belonging to endomysium and perimysium were selected and averaged for every tissue section ($n=10$) and used for determining secondary structure of protein content (Table 2; Fig. 4). The same differences were found between

Table 2 Secondary structure calculation from perimysium and endomysium FT-IR spectra

	α-helix	Triple helix	β-sheets	β-turns	Unordered
Perimysium	18.9±0.4[a]	17.6±0.8[a]	28.3±1.5[a]	22.6±2.2	12.6±0.8
Endomysium	16.0±0.5*[b]	15.4±0.6*[b]	31.6±1.1*[b]	24.9±1.6[b]	13.0±0.6

*Significantly different from perimysium, $P<0.05$
[a] Significant correlation with tI-C secondary structure parameters, $P<0.05$
[b] Significant correlation with tIV-C secondary structure parameters, $P<0.05$ (see Table 1 for details). $n=10$ spectra for each sample

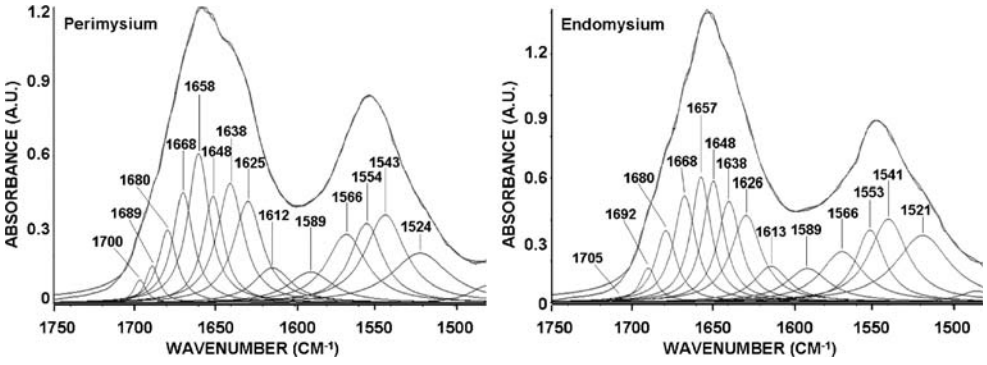

Fig. 4 Spectral curve-fitting of perimysium (*left*) and endomysium (*right*) FT-IR spectra for the 1,750–1,400 cm^{-1} spectral interval. Absorption bands of amide I are used for secondary structure calculation (Table 2)

perimysium and endomysium as for tI-C and tIV-C, respectively, i.e., perimysium secondary structure presented higher amounts of α-helix and triple helix ($P<0.05$), while the proportion of β-sheets was lower ($P<0.05$) than for endomysium. Again, as for collagen types, relative amounts of β-turns and unordered structure were found to be similar. It is also noteworthy that several features of secondary structure of perimysium protein contents were found significantly correlated to the results obtained for tI-C: relative amounts of α-helix, triple helix, and β-sheets were found to be very similar ($P<0.05$). The same level of correlation was found between secondary structures of tIV-C and endomysium protein contents ($P<0.05$). These results clearly indicate that skeletal muscle perimysium and endomysium may be analyzed by FT-IR spectroscopy and imaging on the basis of the contents of their main collagen type. A further step in this functional FT-IR imaging of connective tissue will be the ability to differentiate other collagen types, thus allowing determination of the relative amount of each one. Alterations in amounts of collagen type are currently investigated to explain connective tissue degeneration in many skeletal muscle pathologies [6].

Conclusion

This study has shown that type I and IV collagens may be differentiated by using several secondary structure parameters revealed by curve-fitting the amide I spectral interval of FT-IR spectra. Moreover, FT-IR imaging allows differentiation of the main connective tissue compartments of skeletal muscle, perimysium and endomysium, on the basis of these secondary structure parameters. An enhancement of this analytical tool might be the development of a software subroutine able to determine the secondary structure of protein contents found under every pixel of an FT-IR image. Moreover, it can be expected that future FT-IR imaging systems will rapidly use higher spatial resolution (currently ca. 6 μm), thus allowing more detailed analysis of the junctions between collagen types in the different compartments of connective tissue. These perspectives open the route to a functional FT-IR imaging of tissues on the basis of molecular features considered as characteristic of a given physiological situation (e.g., pathology or necrosis), which may be named a molecular histopathology.

References

1. Stamler JS, Meissner G (2001) Physiol Rev 81:209–237
2. Rossi MA (1998) Int J Cardiol 66:183–194
3. Diomedi-Camassei F, Boldrini R, Rava L, Donfrancesco A, Boglino C, Messina E, Dominici C, Callea F (2004) J Pediatr Surg 39:1673–1679
4. Wang Q, Sanad W, Miller LM, Voigt A, Klingel K, Kandolf R, Stangl K, Baumann G (2005) Vib Spectrosc 38:217–222
5. Passerieux E, Rossignol R, Chopard A, Carnino A, Marini JF, Letellier T, Delage JP (2006) J Struct Biol 154:206–216
6. Purslow PP (2002) Comp Biochem Physiol A Mol Integr Physiol 133:947–966
7. Sifre L, Berge P, Engel E, Martin JF, Bonny JM, Listrat A, Taylor R, Culioli J (2005) J Agric Food Chem 53:8390–8399
8. Petibois C, Déléris G (2006) Trends Biotechnol 24
9. Cohenford MA, Rigas B (1998) Proc Natl Acad Sci USA 95:15327–15332
10. Kneipp J, Lasch P, Baldauf E, Beekes M, Naumann D (2000) Biochim Biophys Acta 1501:189–199
11. Yano K, Ohoshima S, Gotou Y, Kumaido K, Moriguchi T, Katayama H (2000) Anal Biochem 287:218–225
12. Naumann D, Helm D, Labischinski H (1991) Nature 351:81–82
13. Fabian H, Naumann D (2004) Methods 34:28–40
14. Petibois C, Rigalleau V, Melin AM, Perromat A, Cazorla G, Gin H, Deleris G (1999) Clin Chem 45:1530–1535
15. Petibois C, Cazorla G, Cassaigne A, Deleris G (2001) Clin Chem 47:730–738
16. Knudsen GM, Rostrup E, Hasselbalch SG (2004) Int Congress Series 1265:189–200
17. Miller JC, Thrall JH (2004) J Am Coll Radiol 1:4–23
18. Venturoni M, Gutsmann T, Fantner GE, Kindt JH, Hansma PK (2003) Biochem Biophys Res Commun 303:508–513
19. Petibois C, Gionnet K, Goncalves M, Perromat A, Moenner M, Déléris G (2006) Analyst 131:640–647
20. Goormaghtigh E, Ruysschaert JM, Raussens V (2006) Biophys J 90:2946–2957
21. Sun WY, Fang JL, Cheng M, Xia PY, Tang WX (1997) Biopolymers 42:297–303
22. Hu Y, Li W, Hu J (2005) Spectrochim Acta A Mol Biomol Spectrosc 62:16–21
23. Ami D, Natalello A, Taylor G, Tonon G, Maria Doglia S (2006) Biochim Biophys Acta 1764:793–799

24. Muyonga JH, Cole CGB, Duodu KG (2004) Food Chem 86:325–332
25. Crupi V, De Domenico D, Interdonato S, Majolino D, Maisano G, Migliardo P, Venuti V (2001) J Mol Struct 563–4:115–118
26. Li MJ, Hsu HS, Liang RC, Lin SY (2002) Ultrastruct Pathol 26:365–370
27. Wetzel DL, Post GR, Loddler RA (2005) Vib Spectrosc 38:53–59
28. Bi X, Li G, Doty SB, Camacho NP (2005) Osteoarthr Cartil 13:1050–1058
29. Liu KZ, Dixon IM, Mantsch HH (1999) Cardiovasc Pathol 8:41–47
30. Kalluri R (2003) Nat Rev Cancer 3:422–433
31. Sundaramoorthy M, Meiyappan M, Todd P, Hudson BG (2002) J Biol Chem 277:31142–31153

Research Report

- RESEARCH REPORT -

Effect of tumor phenotype in the formation of blood capillaries: molecular analysis by FTIR spectral imaging

---

Purpose: The aim of this study was to use FTIR spectral imaging to investigate whereas different angiogenic phenotype derived tumors induce different angiogenic stress levels altering the chemical compositions of blood vessels. Two cell-derived tumors, obtained with either C6 (rat) or U87 (human) glioma cell lines, were used for this purpose. Glioma cells have been implanted onto the chorio-allantoic membrane (CAM) of the chicken embryo to develop highly vascularized solid tumors 7 days after implantation. The CAM is a densely vascularized extra-embryonic tissue of the chick embryo, which allows nutrients and oxygen intake. FTIR imaging was used to analyze blood capillaries spectral features and differences between tumor phenotypes.

Background: Generally, solid tumor growth may induce a local increase in free radicals, leading to the alteration of normal cellular processes through peroxidation of lipids, proteins, and nucleic acids. Tumors also differ widely in their energy requirement, depending on the cell types considered, tumor grade and tissue locations. The rat C6 glioma cell line is widely used as a model mimicking the growth of human glioblastoma multiforme. The U87 cell line is a human phenotype known to develop a highly vascularized tumor similar to those occurring naturally in human glia (glioblastoma or astrocytoma).

Main results: The two cell phenotypes produced highly vascularized solid tumors, highlightling the high angiogenic properties of C6 and U87 cells. Variations in the ν=(CH), $\nu_{as}(CH_3)$, and $\nu_{as}(CH_2)$ IR absorptions (3050–2800 cm^{-1} spectral interval) were analyzed for determining fatty acyl chain length and unsaturation level in cells of blood capillaries, pericytes and endothelial cells. The results obtained from the curve fitting of the 3050 - 2800 cm^{-1} spectral interval revealed that the ν=(CH)/$\nu_{as}(CH_3)$ ratio

was higher in C6 tumor capillaries with respect to U87 tumor capillaries, and an opposite results was obtained for the $\nu_{as}(CH_2)/\nu_{as}(CH_3)$ ratio. We might hypothesize that these absorption changes could result from tumor cell aggressiveness because they mainly arise from the lipid content of cell membranes in blood capillaries. However, the biological interpretation of this result is not possible using only this spectral information. Oxidative stress effects on fatty acyl chain contents of membrane phospholipids would require further determinations to study the balance between reactive oxygen species and antioxidants, which is not envisageable on dried tissue sections. Nevertheless, the aim of this study was to determine spectral markers discriminating between tumor phenotypes effects on blood capillary formation. These spectral markers based on fatty acyl chain absorptions might be considered for discriminating between cell phenotypes in brain tumors.

Moreover, we could observe another spectral difference of capillaries between the two phenotypes for absorptions in the 1200-950 cm^{-1} spectral interval, which is attributed mainly to sugars. Second derivative spectra showed that the absorption band at 1056 cm^{-1} in U87 was shifted to 1051 cm^{-1} and the band centered at 1041 cm^{-1} was not found in C6 tumor blood capillaries. Hierarchical analysis of first derivative FTIR spectra of blood vessels based on the 1200-950 cm^{-1} spectral interval discriminated clearly between the two populations of blood capillaries. This other spectral marker could not be linked to the previous one on fatty acyl chains, but this double differentiation between two tumor cell phenotypes suggest two possible interpretations: 1- if these two spectral changes are interdependent, i.e., they belong to same molecules, then a glycolipidic marker may show changes between tumor phenotypes; 2- if these two spectral changes are not interdependent, then at least two molecular markers should allow the differentiation between tumor phenotypes. Further studies are required to address this point, but this study has clearly demonstrated that spectral markers of differentiation might be used for identifying the cell phenotype involved in the tumor formation by FTIR imaging.

Contribution to a "molecular histology of brain glioma": The high level of heterogeneity encountered in gliomas does not facilitate the use and the interpretation of routine histological markers. Sometimes, low-grade astrocytomas have a tendency to develop over time into anaplasic or even malignant neoplasms.

Glioblastoma and ganglioglioma may look like meningioma or metastasis in computer tomography or magnetic resonance imaging images, as well as *ex vivo* after surgical excision. Histological examination is not always suitable for identifying these different types of tumors with precision. Therefore, the results obtained in this research suggest that modifications of membrane lipids, according with the phenotype of the tumor, can be responsible for functional variations connected with neoplastic growth. These IR markers combined with the changes of band shapes in the carbohydrates spectral interval constitute valuable biochemical parameters which may be useful, together with histological studies, in the diagnosis of brain tumors.

Effect of tumor phenotype in the formation of blood capillaries: molecular analysis by FTIR spectral imaging

Abstract

The aim of this study was to use FTIR spectral imaging for determining chemical markers of discrimination between two glioma cell phenotypes derived tumors on the basis of their blood capillaries. U87 human glioma and C6 murine glioma cells were implanted onto the chorio-allantoic membrane (CAM) of the chicken embryo to develop highly angiogenic solid tumors. Infrared spectra of tumor blood capillaries found in C6-derived tumors indicated a higher unsaturation level of membrane phospholipids than those from U87-derived tumors. This was demonstrated by a curve fitting procedure of the fatty acyl chain spectral interval (3050-2800 cm^{-1}) showing higher ν=(CH)/$\nu_{as}(CH_3)$ and lower $\nu_{as}(CH_2)/\nu_{as}(CH_3)$ ratios (C6 vs. U87, respectively). Moreover, hierarchical analysis of first derivative FTIR spectra of blood vessels in the carbohydrates spectral interval (1200-950 cm^{-1}) differentiated spectra into two clusters, one per tumor phenotype, and with high heterogeneity level. Our results show that tumor phenotype must be taken into account in the analysis of gliomas and that FTIR imaging is able to reveal subtle changes in molecular parameters belonging to blood capillaries of these tumors.

Abbreviations

CAM: chorioallantoic membrane; DMEM: Dulbecco's modified eagle medium; FBS: Fetal bovine serum; FTIR: Fourier Transform Infrared; HA: Hierarchical analysis

Keywords

FTIR spectral imaging, CAM, gliomas, angiogenesis, blood vessels

Materials and methods

Cell culture

U87 and C6 human and murine glioma cells, respectively, were selected for the study as malignant glioma models that form highly vascularized tumors. Cells were maintained in DMEM, with 10% FBS, antibiotics, and L-glutamine, and then incubated in a 37°C-incubator in 5% CO_2. Cells were grown to confluence, harvested after trypsinization, and re-suspended in serum free DMEM for injection.

In vivo CAM assay

The chorioallantoic membrane (CAM) of the chick embryo appears on day 4–5 and its vessels subsequently spread over the surface of the yolk sac, totally covering it [1]. Fertilized chicken eggs (*Gallus gallus*) (EARL Morizeau, Dangers, France) were handled as previously described [2]. Eggs were incubated at 37°C and 80% humidified atmosphere. On day 4 of incubation a window was made in the eggshell after removal of 2–3 mL of albumin so as to detach the developing CAM from the shell. The window was sealed with Durapore® tape and the eggs were returned to the incubator. On embryonic day 10, a plastic ring was placed on the CAM, and 5 million of U87 or C6 cells in 20 µl of medium were deposited after gentle laceration of the surface. Digital photos were taken under a stereomicroscope (Nikon SMZ800). Tumors were removed after 7 days of injection (embryonic day 17), placed in tubes without fixatives before to be frozen in liquid N_2 and stored at -80°C until required.

Histology and Immunohistochemistry procedures

CAM tumors were covered by cooled glue (polyvinyl alcohol for cryostat, -20°C). Serial sections (Cryostat 3050-TM, Leica-Microsystems, France) of 20 µm in thickness were transferred, respectively, onto a glass slide (SuperFrost) for immunohistochemistry assessment, and onto a Zinc Selenide (ZnSe) windows for FTIR spectro-imaging. All tissue sections were dried on air before further processing. In order to get more precision and reproducibility of data, we preferred to do immuno-histochemistry also on the same sections of ZnSe windows after image acquisition for each CAM sample. Immunohistochemistry was used to highlight all blood vessels of tumor sections and for further comparisons with FTIR analyses. For this, the 20

µm sections were fixed in paraformaldehyde 4% for 10 minutes, then washed with PBS containing 0.1% Triton X-100 (PBS-T; Sigma). Slides were incubated with biotinylated Sambucus Nigra lectin (SNA-lectin) antibody (1:500; Vector Laboratories), for 45 minutes at room temperature in a humidified chamber. After washing with PBS, sections were then incubated with standard avidin–biotin complex (Vectastain Elite kit ABC, Vector Laboratories) for 30 min for routine signal amplification. Antibody binding was revealed using H_2O_2 as a substrate and diaminobenzidine as chromogen. Counterstaining was performed with hematoxylin only on superfrost slide sections but not for the ZnSe sections [3].

FTIR spectral imaging acquisition

Spectral images were collected in transmission mode using a Spotlight 300 FTIR imaging system, equipped with a Spectrum One spectrometer (Perkin-Elmer, France). The imaging system was equipped with a liquid N2-cooled MCT linear detector comprising 16 pixel elements. FTIR images were collected from CAM tumor sections, in the 4000-720 cm^{-1} range using 8 scans with 4 cm^{-1} as spectral resolution and 6.25*6.25 µm spatial resolution per pixel. Highly vascularized areas were selected referring to the immunohistochemical sections on slides. After image acquisition, we also performed immunohistochemistry for ZnSe sections.

Data processing and analysis

Referring to immunohistochemistry, we obtained 90 spectra for capillary blood vessels for each tumor phenotype. After baseline correction, data treatments were performed using OPUS 4.2 software (Bruker, Germany). FTIR spectra representing blood capillaries for each group were averaged to form model spectra (called “MS-group” U87 and “MS-group” C6, respectively). The second derivative spectrum of every MS was used to determine the position of all absorption bands within the 3050-2800 cm^{-1} spectral interval, with a 9-point smoothing and 0.44% sensitivity (subroutine of OPUS 4.2 software, Bruker). The minimum values yielded absorption bands at 3030, 3012, 2981, 2959, 2921, 2894, 2872, 2852, and 2811 cm^{-1} and were all found in the two MS models. Spectral curve fitting procedure could thus be performed after fixing bands at these values to obtain a “Report”. For every FTIR spectrum corresponding to a blood capillary, all absorptions bands were modeled by

the curve fitting procedure based on Lorentzian function, by applying the “Report” obtained from MS given by the curve-fitting toolbox.

Statistics

Data used for comparison between the two groups, were expressed as mean ± SD. A paired Student’s *t*-test was used to determine differences between series of data between the two groups. *P-values* were fixed at .05 to consider the significance level of differences between series of data.

Results

Phenotypic changes of tumor tissues

Glioma cells deposited on the CAM surface form solid tumors that exhibit characteristic features of malignant progression. Phenotypic changes of C6 and U87 cell derived tumors were checked 4 and 7 days after implantation. U87 cell derived tumors grew rapidly and formed a compact tumor mass at day 4 more expanded at day 7. These tumors presented a structured vascular network into the whole tumor mass at day 7. C6 cell-derived tumors have shown to be more expanded than U87 at day 4 and they were likely to be exploded at day 7. They were more edematous and sometimes showed necrotic and hemorrhagic areas with different patterns of vascularization ***(Figure 1).*** To get a similar behavior of glial cells during malignant glioma grade, we only analyzed day-7 tumors for data treatment and statistics.

FTIR data analysis

Careful examination of spectra indicates that most of the variability between the two cell-derived tumor blood capillaries is in the fatty acyl and carbohydrates spectral intervals (i.e., 3050–2800 and 1200–950 cm^{-1}).

1. *Fatty acyl chain spectral interval*

Spectra exhibited significant differences between their profiles. In order to interpret these spectral differences and to understand the biochemical variations in tumor blood vessels for each angiogenic phenotype, we used the curve fitting procedure for the spectral interval of 3050-2800 cm^{-1}. Using this procedure to every FTIR spectrum

of each capillary blood vessel, we analyzed the variations of the absorption bands at 3012 cm^{-1} for ν=(CH), 2959 cm^{-1} for $\nu_{as}(CH_3)$ and 2921 cm^{-1} for $\nu_{as}(CH_2)$, identified from the second derivative spectra of averaged capillary for each tumor phenotype ***(Figure 2)***. These absorptions are mainly due to the asymmetric stretching vibrations mode of the fatty acyl moieties of membrane phospholipids for determining the level of phospholipid unsaturation in blood vessel membranes. The results obtained from the curve fitting of the 3050–2800 cm^{-1} spectral interval ***(Figure 3)*** revealed that the ν=(CH)/$\nu_{as}(CH_3)$ ratio is higher in C6 tumor BV than U87 tumor BV (17.7% increase). However, the $\nu_{as}(CH_2)/\nu_{as}(CH_3)$ ratio (8.7% decrease) was lower in C6 than in U87 tumor BV. Only the ν=(CH)/$\nu_{as}(CH_3)$ ratio shows a significant difference ($P< 0.05$) between the two populations (see ***Table 1*** for more details).

2. Carbohydrates spectral interval

Figure 4 shows the second derivative of the averaged capillary spectra for each tumor phenotype within the carbohydrates spectral interval (1200-950 cm^{-1}). As we can see, the main difference is situated between the 1020 and 1080 cm^{-1} spectral interval. Obviously, the absorption band at 1056 in U87 is shifted to 1051 cm^{-1} and the band at 1041 cm^{-1} is not present in C6 tumor BV. Moreover, in order to see if these differences are able to separate the two sets of blood vessels, we performed a hierarchical analysis (HA). HA was used to classify spectra of blood vessels issued from the two cell-derived tumors using the first derivatives of the spectra with 5-point smoothing. Based on the carbohydrates spectral interval (1200-950 cm^{-1}), we got a good discrimination between the two sets of data. As we can see in ***Figure 5,*** the two sets of data were correctly classified without any overlapping.

References

1. Ribatti D, De Falco G, Nico B, Ria R, Crivellato E & Vacca A (2003) In vivo time-course of the angiogenic response induced by multiple myeloma plasma cells in the chick embryo chorioallantoic membrane. *J Anat* **203**, 323-328.
2. Hagedorn M, Javerzat S, Gilges D, Meyre A, de Lafarge B, Eichmann A & Bikfalvi A (2005) Accessing key steps of human tumor progression in vivo by using an avian embryo model. *Proc Natl Acad Sci U S A* **102**, 1643-1648.
3. Sihn G, Walter T, Klein JC, Queguiner I, Iwao H, Nicolau C, Lehn JM, Corvol P & Gasc JM (2007) Anti-angiogenic properties of myo-inositol trispyrophosphate in ovo and growth reduction of implanted glioma. *FEBS letters* **581**, 962-966.

Tables

Table 1: Curve fitting results showing the different values of ratios in the fatty acyl chain spectral interval for the two tumor cell phenotypes.

	Asymmetric stretching bands	
	ν=(CH)/$\nu_{as}(CH_3)$	**$\nu_{as}(CH_2)/\nu_{as}(CH_3)$**
C6	0.73 ± 0.47	1.72 ± 0.75
U87	0.62 ± 0.31	1.87 ± 0.72
t test	0.044 *	0.088
C6 vs. U87	17.7 %	- 8.7 %

Average values ± SD for ratios of the fatty acyl chains in the two cell derived tumors. n=90 blood capillary spectra for each tumor phenotype. An increase in the percentage of ν=(CH)/$\nu_{as}(CH_3)$ versus a decrease in the percentage of $\nu_{as}(CH_2)/\nu_{as}(CH_3)$ are shown in the last line of this table. We assigned a " – " to mention the decrease in the percentage. The student *t* test performed shows a significant difference (*) between the two populations for the first ratio (P< 0.05).

Figures

Figure 1: A: Tumor cells were deposited onto the CAM of embryonated chicken eggs at day 17 of development. **B** and **C:** U87 and C6 cell derived tumors, respectively, after 7 days of implantation. We can obviously see that C6 tumors were more edematous than U87. **D:** From the left to the right, tumor sections with immunohistochemistry (IHC) on slide, visible image by Spotlight, visible image after IHC on ZnSe window to locate all blood capillaries marked with SNA-lectin (brown). FTIR image was realized using 8 scans with a spectral resolution of 4 cm^{-1} and a spatial resolution of 6.25 µm. Spectra were chosen according to the IHC section. Scale bar represents 200 µm.

Figure 2: Second derivative averaged spectra of each tumor phenotype blood capillary model within the 3050-2800 cm^{-1} spectral interval. Minimum values at 3012, 2959, and 2921 cm^{-1} represent asymmetric stretching vibrations of fatty acyl moieties.

Figure 3: Spectral curve fitting performed within the 3050-2800 cm^{-1} spectral interval. Absorption bands at 3012 cm^{-1} for ν=(CH), 2959 cm^{-1} for $\nu_{as}(CH_3)$, and 2922 cm^{-1} for $\nu_{as}(CH_2)$ were used to calculate the ν=(CH)/$\nu_{as}(CH_3)$ and $\nu_{as}(CH_2)/\nu_{as}(CH_3)$ ratios.

Figure 4: Second derivative spectra of each tumor phenotype blood capillary model within the 1200-950 cm^{-1} spectral interval for carbohydrates determination. As we can see, the absorption band at 1056 in U87 is shifted to 1051 cm^{-1} and the band at 1041 cm^{-1} is not present in C6 tumor BV.

Figure 5: Hierarchical analysis of 1st derivative spectra of each tumor phenotype blood capillaries (n=90 for each phenotype) within the carbohydrates spectral interval (1200-950 cm^{-1}).

Figure 1

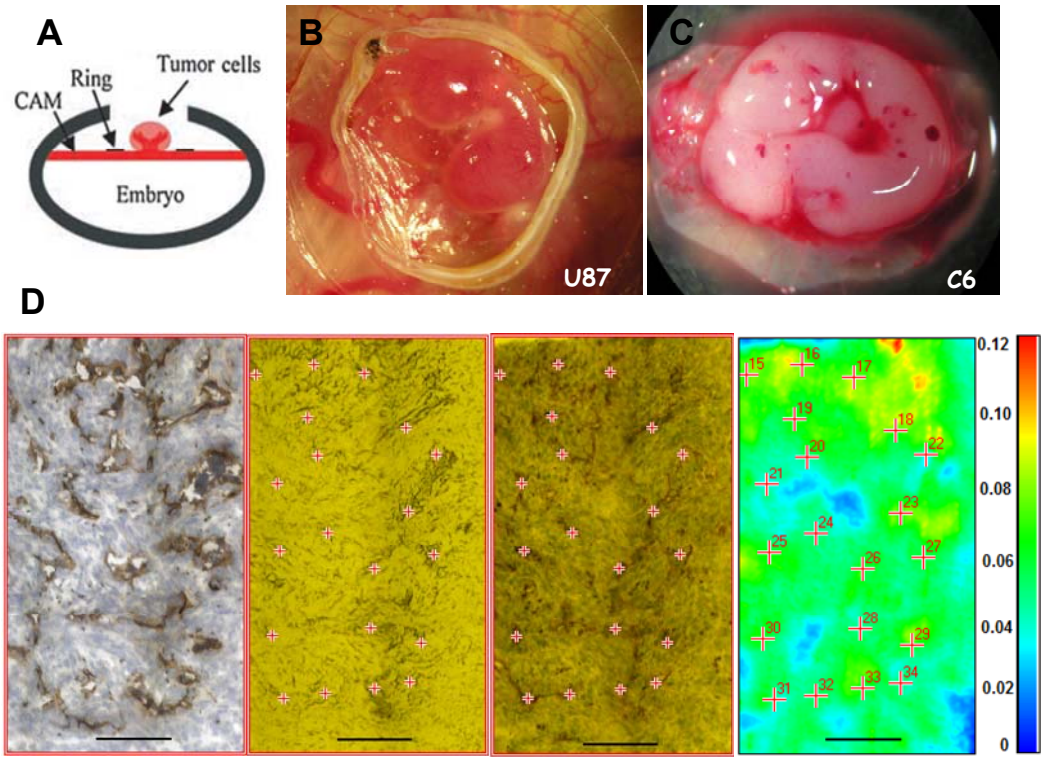

Figure 2

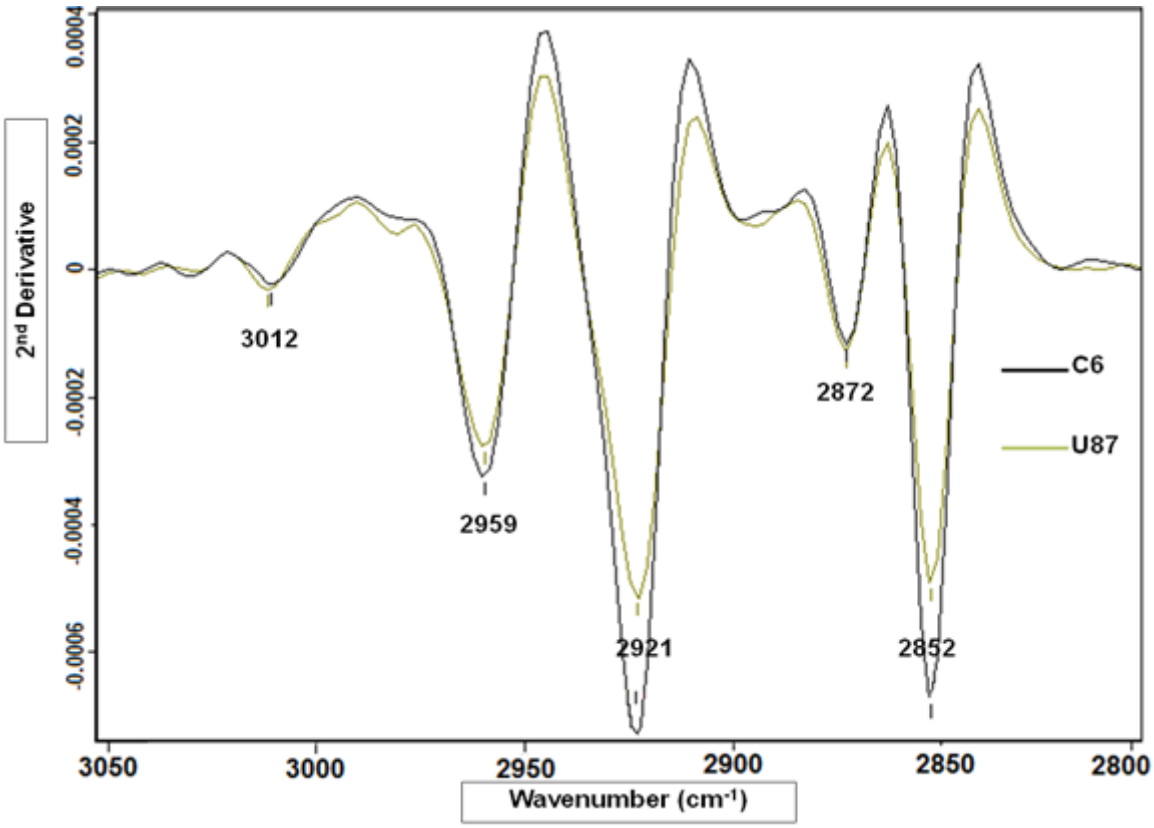

Figure 3

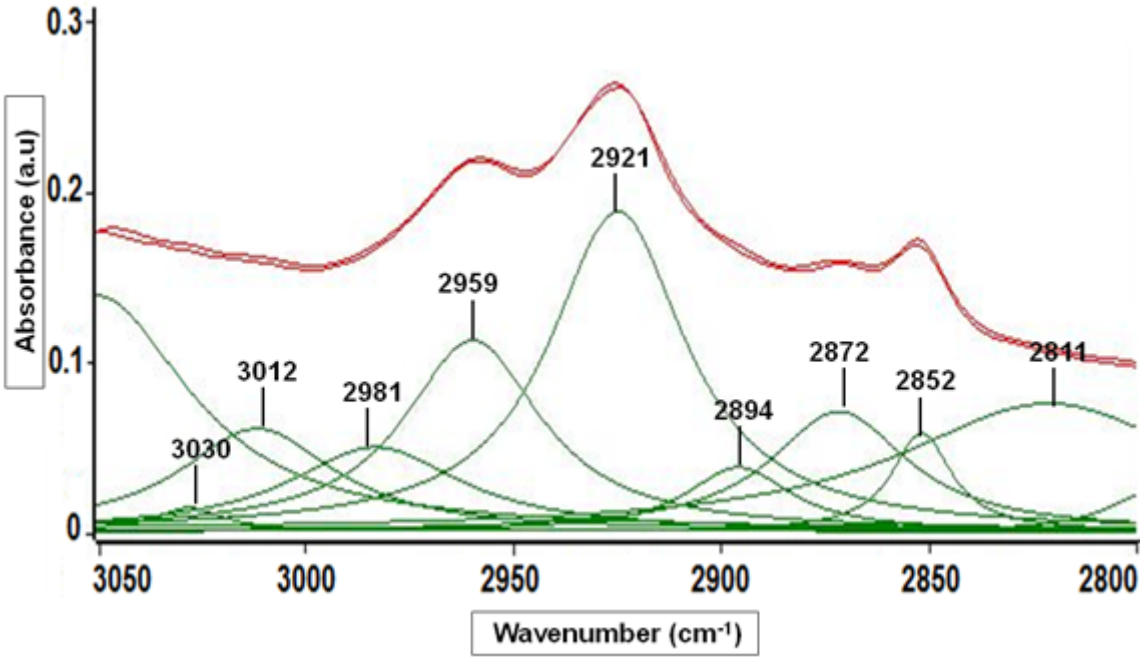

Figure 4

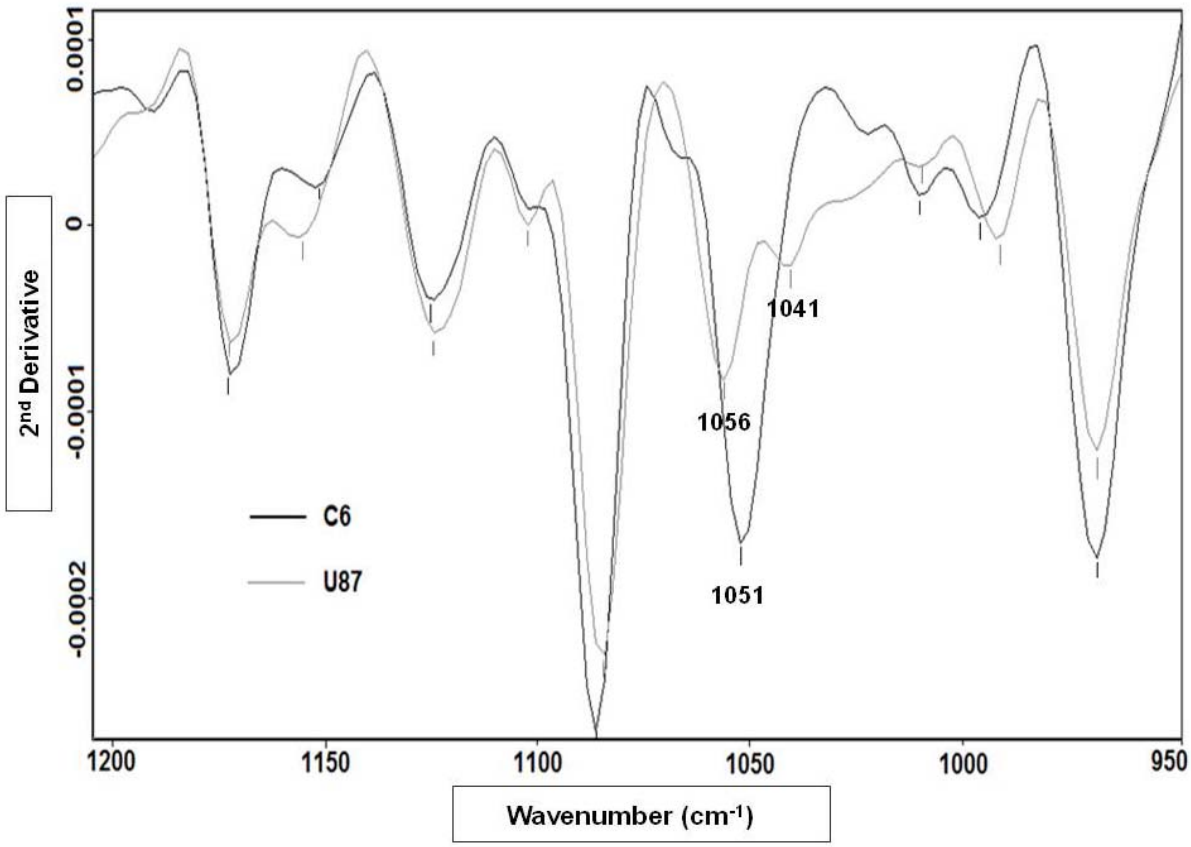

Figure 5

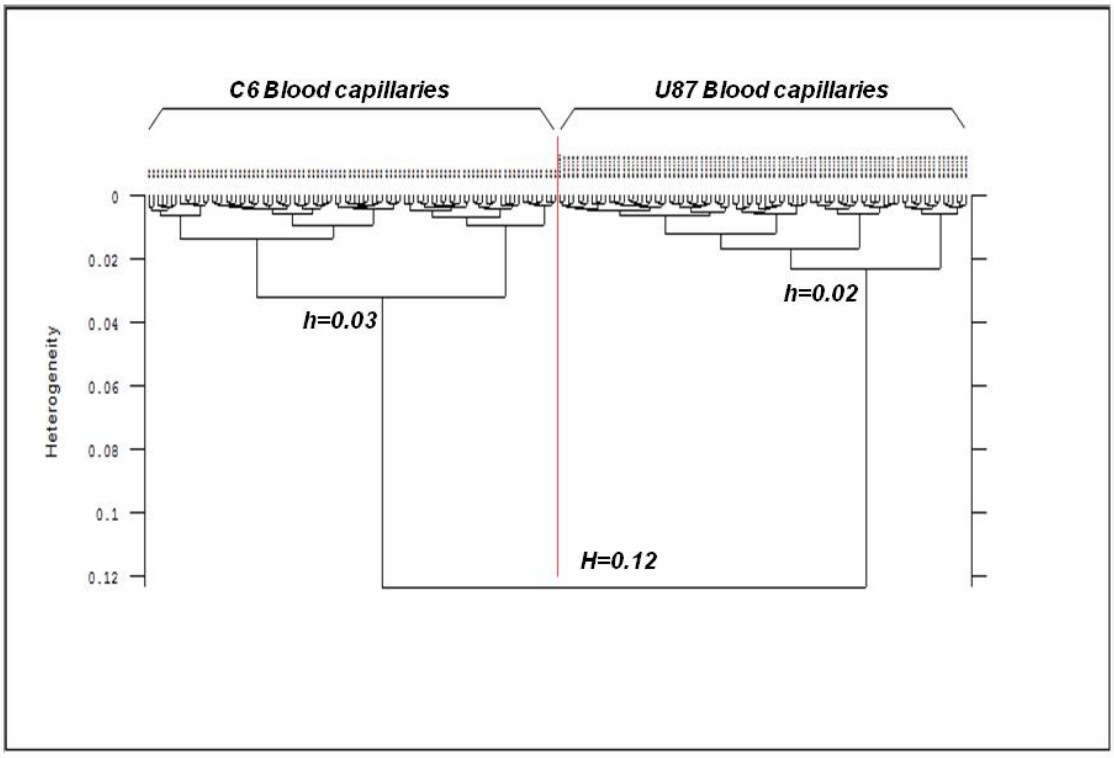

Paper II

- PAPER 2 -

FTIR spectral imaging of blood vessels reveals protein secondary structure deviations induced by tumor growth

---

Anal Bioanal Chem. 2008 Sep; 392(1-2):129-35.

Purpose: The aim of this study was to analyze the molecular structures of blood capillaries of astrocytic tumors at different stages of the tumor growth by FTIR spectral imaging. A reproducible animal model (Rag-gamma mice) was used to assess the potential of FTIR spectral imaging for determining structural features in vascular basement membrane (VBM) protein contents 14 and 21 days after implantation.

Background: Vascular basement membrane remodeling is involved in tumor angiogenesis to enable tumor invasion and growth. During angiogenesis, VBM is degraded and disassembled to be finally reorganized to a native state around a newly formed capillary. Collagens (especially type IV) are the main components of BM proteins (at least 50%). The VBM of tumor capillaries is characterized by variable diameter, swelling, vacuolization, and degeneration. These changes in collagen assembly and disposition in VBM exposed to the tumor angiogenic stress are now regarded as sub-molecular targets for tumor imaging and diagnosis.

Main results: To analyze capillary blood vessels by FTIR spectral imaging, a curve-fitting procedure (method already used for data treatments in the first publication) was proposed to determine changes in the secondary structure of protein contents of VBM at the two stages of tumor growth. For largest blood capillaries of a diameter >20 microns, tumor growth had induced a decrease in triple-helix content (1638 cm^{-1}; $P<0.05$) and an increase in beta turns (1666 and 1615 cm^{-1}; $P<0.01$). These protein structure alterations, resulting from type IV collagen loss, reflected the high angiogenic stress of growing tumors. We could note also that for blood capillaries of

small diameter, < 20 µm, these differences were not observed. Therefore, our results clearly show that FTIR imaging has the potential to reveal the steps effects of tumor growth on blood capillaries formation. We thus propose to use these molecular markers of VBM protein alterations for gradation of solid tumors by FTIR spectral imaging.

Contribution to a "molecular histology of brain glioma": C6 tumors obviously mimick human glioma tumor phenotype. The subcutaneous (s.c.) space is essentially avascular. s.c. tumors will therefore be artificially selected to grow in an angiogenesis-dependent fashion. Tumor cells rapidly grow and form angiogenic tumor by presenting the histopathological features of human GBM. Our results support previous studies that reported the presence of collagen fibers irregularly disposed in blood capillaries of brain tumors. The collagen decrease may support the hypothesis that the angiogenesis stress increases with tumor growth. This study has shown that the triple helix and β-turn contents of the secondary structure of VBM proteins might be used as molecular markers for a functional FTIR spectral imaging of tumors. The result opens the way to the development of a molecular histopathology, which might become a useful analytical tool for neurosurgeons. Therefore, we later proposed to use these molecular markers on human glioma sections in order to see if same deviations will be obtained.

Anal Bioanal Chem (2008) 392:129–135
DOI 10.1007/s00216-008-2230-6

ORIGINAL PAPER

FT-IR spectral imaging of blood vessels reveals protein secondary structure deviations induced by tumor growth

Katia Wehbe · Raphael Pinneau · Michel Moenner · Gérard Déléris · Cyril Petibois

Received: 9 January 2008 / Revised: 3 June 2008 / Accepted: 4 June 2008 / Published online: 18 July 2008

Abstract Vascular basement membrane remodeling is involved in tumor angiogenesis to enable tumor invasion and growth. FT-IR spectral imaging was used to determine changes in tumor blood vessels to reveal protein secondary structure in Rag-gamma immuno-deficient mice sacrificed 14 and 21 days after subcutaneous glioma implantation. For the oldest blood capillaries (diameter >20 microns), tumor growth induced a decrease in triple-helix content (1638 cm^{-1}; −7.3%; $P<0.05$) and an increase in beta turns (1666 and 1615 cm^{-1}; +4%; $P<0.01$). These protein-structure alterations, mainly from type IV collagen, reflected the high angiogenic stress of growing tumors. We propose to use these molecular markers of vascular basement membrane protein alterations for gradation of solid tumors by FT-IR spectral imaging.

Keywords FT-IR spectral imaging · Cancer · Angiogenesis · Basement membrane proteins

Abbreviations

BM	Basement membrane
DMEM	Dulbecco's modified Eagle's medium
FBS	Fetal bovine serum
FT-IR	Fourier-transform infrared
MRI	Magnetic resonance imaging
PET	Positron-emission tomography
VBM	Vascular basement membrane

Electronic supplementary material The online version of this article (doi:10.1007/s00216-008-2230-6) contains supplementary material, which is available to authorized users.

K. Wehbe · G. Déléris · C. Petibois (✉)
Université de Bordeaux, CNRS UMR 5084, CNAB,
146 Rue Léo Saignat,
33076 Bordeaux-Cedex, France
e-mail: cyril.petibois@u-bordeaux2.fr

R. Pinneau · M. Moenner
Université Bordeaux 1, INSERM U920,
Avenue des Facultés,
33405 Talence-Cedex, France

Introduction

Malignant gliomas, the most common primary brain tumors, are very aggressive and highly invasive tumors which diffuse heterogeneously into the surrounding parenchyma [1]. To date, the "gold standard" for brain cancer diagnosis is histopathological examination, by experienced pathologists, using standard light microscopy-based techniques. In many cases, histopathologic examination is unable to provide a firm diagnosis because of tissue heterogeneity [2]. Thus, despite various therapeutic and diagnostic efforts, high-grade gliomas (grades III and IV) still represent an unsolved problem for neuro-oncologists [1].

Glioblastoma (GB) tumors can be difficult to remove due to the lack of defined tumor limits. The tumor may extend into normal-looking brain tissue and/or can be localized near critical areas of the brain. Determination of tumor limits and assessment of tumor grade is of clinical importance in improving patient prognosis. Imaging techniques such as PET or MRI can be helpful in diagnosing brain tumor occurrence [1] but are also characterized by a spatial resolution at the millimeter scale and/or mmol L^{-1} sensitivity [3]. Thus, with respect to human brain glioblastoma volumes, i.e. a few mm^3, these imaging modalities suffer from limitations.

Therefore, new approaches are required for rapid and objective classification of brain tumors and it is believed that ex vivo imaging techniques still have a critical role to play in the development of new molecular histopathology tools. Among the methods recently developed for disease pattern recognition in the field of cancer diagnosis, vibrational spectroscopy, mainly Fourier-transform infrared

(FT-IR) spectroscopy, could be applied with success, owing to the possibility of performing quantitative analysis of molecular composition of healthy and pathological tissues [4]. When applied to biological specimens, this technique reveals the vibrational modes of functional groups within the biomolecules present, i.e., mainly proteins, nucleic acids, lipids, and carbohydrates. Data-treatment methods enable correlation of the chemical information with biological features, enabling functional interpretation of histological structures [5]. Thus, changes in cell or tissue composition induced by any pathological process can be revealed by the chemical information contained in FT-IR spectra [6]. FT-IR spectroscopy may now be coupled to an optical microscope and a 2D array IR camera to enable FT-IR spectral imaging.

The advantage of using FT-IR spectral imaging to characterize biological substances lies in the very simple sample preparation [7], i.e., it does not require sample staining or fixation, and full spectral acquisition is done within only a few minutes for a 1-mm^2 tissue area. FT-IR spectral imaging may thus be used for examining extemporaneous biopsies to help give an answer to the neuro-oncologist with delays compatible with subsequent surgery. Using this technique, the metabolic status of cells has been analyzed within glioblastoma tissue sections [8], providing evidence that glucose content decreased linearly with the distance from blood vessels while lactic acid increased [9]. This metabolic pattern of change is representative of the ischemic condition of cells within the tumor mass and highlights the critical role played by tumor blood vasculature in this kind of tumor.

Recent experimental evidence has shown that angiogenesis is an essential phenomenon in tumor growth and progression beyond a few cubic millimeters in size [10]. Angiogenesis is the development of new blood vessels from preexisting ones [11]. The vascular basement membrane (VBM) is an amorphous, dense, sheet-like structure of 50–100 nm in thickness [12] that constitutes an insoluble structural wall of newly formed capillaries and undergoes sub-molecular changes during tumor-induced angiogenesis. Most of these protein structural changes are due to the unfolding, degradation, and refolding of collagen contents during the capillary sprouting process of angiogenesis. Collagen proteins (especially type-IV) are the main components of BM, comprising 50% of all BM proteins [12]. The triple helix forms 85% of the collagen IV sequence [13] and exhibits a characteristic IR band in the amide spectral range (1700–1500 cm^{-1}) [14]. On this basis, it has recently been proposed to use FT-IR spectral imaging to analyze molecular changes in BM of capillary blood vessels exposed to the angiogenic stress of growing tumors.

The aim of this study was to analyze the molecular structures of blood capillaries of astrocytic tumors at different stages by FT-IR spectral imaging. A reproducible animal model (Rag-gamma mice) was used to assess the potential of FT-IR spectral imaging for determining structural features in VBM protein contents at different moments of tumor growth (14 and 21 days). This approach offers the prospect of non-subjective grading of tumor malignancy.

Materials and methods

Cell culture

Rat C6 glioma cells were selected for the study as an established model for malignant gliomas that form highly vascularized tumors. Rat C6 glioma cells (ATCC, passage 24) were maintained in culture using Dulbecco's modified Eagle's medium (DMEM) with 10% FBS, l-glutamine (2 mmol L^{-1}), and antibiotics (penicillin 50 UI mL^{-1}, streptomycin 50 μg mL^{-1}). Cell culture was performed in a 37°C incubator with humidified atmosphere and 5% CO_2. Cells were grown to confluence, harvested after trypsinization, and re-suspended in serum-free DMEM for injection.

Animals

Six week-old male Rag-gamma immuno-deficient mice (n= 12) were randomly divided into two groups of six animals each with an average weight of 24 g. Animals were anesthetized using Imalgene 1000 (Ketamin 10 g/100 mL) injected intraperitoneally. C6 rat glioma cells (5×10^5 cells per animal) were suspended in 100 μL medium and implanted subcutaneously (s.c.) into the flanks of mice. S. c. xenografted tumors were removed from mice 14 and 21 days post-implantation (named Group-14 and Group-21, respectively). Tumor volume was determined for every animal. Because all tumors exhibited ellipsoid form, the formula used for volume (cm^3) determination was:

$$\text{Volume} = 4/3 \times \pi(0.5\ \text{W} \times 0.5\ \text{L} \times 0.5\ \text{H}) \quad (1)$$

where all axes are measured in cm, "W" is the width axis, "L" is the length axis, and "H" is the height axis. All tumors were washed in PBS solution and placed in tubes without fixatives before freezing in liquid N_2 and storage at –80°C until required.

Tissue samples

For every tumor specimen, frozen tissue was deposited on cooled glue (poly(vinyl alcohol) for cryostat, –20°C) to avoid tissue embedding. Additional glue was used to homogenize the sample intended for cryosections (Cryostat 3050-TM, Leica-Microsystems, France). Serial frozen

sections 10 and 20 μm thick (seven sections per tumor) were transferred, respectively, on to glass slides (SuperFrost) for immunohistochemistry assessment and on to ZnSe windows for FT-IR spectral imaging. All tissue sections were dried in air before further processing.

Immunohistochemistry

Immunohistochemistry was used to highlight all blood vessels of tumor sections and for further comparisons with FT-IR analyses. The antibody used for this technique was CD31 also designated PECAM-1 (platelet endothelial cell adhesion molecule 1). The 10-μm sections were fixed in paraformaldehyde 4%. Endogenous peroxidase was inhibited using 3% H_2O_2 in distilled water. Sections were then washed in phosphate-buffered saline (PBS 1× solution). Slides were incubated first with the primary antibody (purified rat anti-mouse monoclonal antibody; Pharmingen BD Biosciences), for CD31 (1:100 *v*/*v*). Incubation was performed for 2 h at room temperature in a humidified chamber. After washing, the slides were incubated with goat anti-rat biotinylated polyclonal antibody (1:200 *v*/*v*; Pharmingen BD Biosciences) for 1 h at room temperature. Sections were then washed and incubated with standard avidin-biotin complex (Vectastain Elite kit ABC; Vector Laboratories) for 30 min. Antibody binding was revealed using H_2O_2 as substrate and diaminobenzidine as chromogen. Counterstaining was performed with hematoxylin. Negative control slides were obtained by omitting the primary antibody.

FT-IR spectral imaging acquisition

Tumor sections 20 μm thick consecutive to immunohistological sections were used for FT-IR analyses using a Spotlight 300 FT-IR spectral imaging system equipped with a Spectrum One spectrometer (Perkin-Elmer, France). ZnSe windows were used for tissue section deposition. Once the visible image was obtained, capillary blood vessels were sought for spectral image acquisition, referring to the immunohistochemistry sections to locate all capillaries. Transmittance FT-IR spectra were obtained in image mode (spatial resolution of rebuilt image 6.25 μm, 16 pixels) using eight scans (4000–720 cm^{-1}) and a 4 cm^{-1} spectral resolution. All data acquisition, post-processing (atmospheric and baseline corrections, and normalization), and image construction were performed using sub-routines of Spotlight 1.0 (Perkin-Elmer, France).

Spectral data treatment

For every FT-IR image of blood capillary, the FT-IR spectra corresponding to the pixels covering the basal membrane were averaged and saved for further data treatment. All spectra representing all blood capillaries for each group were averaged to form model spectra (MS-group-14 and MS-group-21). The second-derivative spectrum of every MS was used to determine all absorption bands within the 1750–1480 cm^{-1} spectral range, with nine-point smoothing and 0.4% sensitivity (subroutine of Opus 4.2 software; Bruker). This spectral range shows the two major absorbance bands of proteins (1655 and 1545 cm^{-1} for amide I and II absorption, respectively) and may be used to determine the secondary structure of proteins. This step led to the generation of a calculation frame called "Report" which allows fixing of two kinds of data—the type of function (Lorentzian) and the wavenumbers corresponding to the maximum intensities for every band revealed from second derivative of MS. For every FT-IR spectrum corresponding to a blood capillary, all absorption bands were determined by

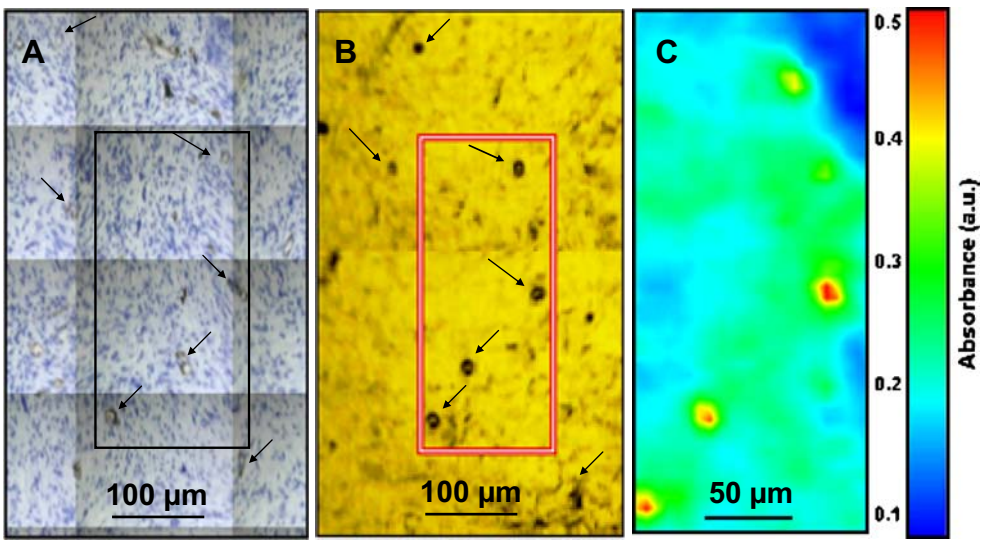

Fig. 1 **A** Optical image of immunohistochemistry section (10 μm) in which all blood vessels revealing tumor angiogenesis are marked with CD31 (*brown*). **B** Visible image of the consecutive tumor section (20 μm). Corresponding capillary blood vessels are shown (*arrows*). **C** Full spectral intensity (total absorbance for the 4000–720 cm^{-1} spectral range) image of capillaries in the selected area (*red square*)

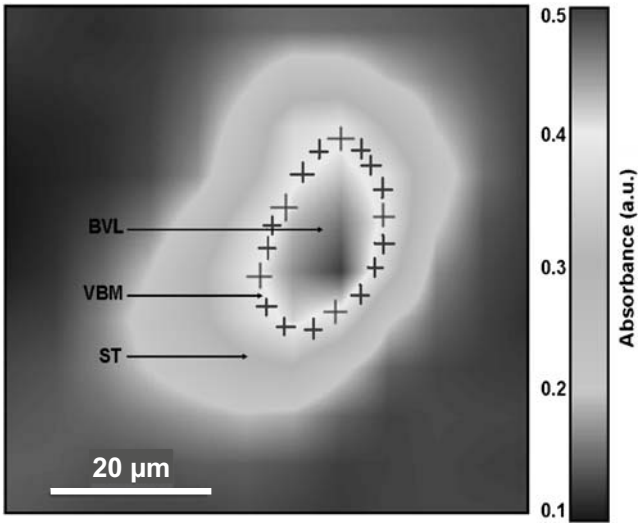

Fig. 2 Gray-scale representation of the full spectral image of a capillary blood vessel. The *white circle* in the center represents the vascular basement membrane (*VBM*) with the endothelial cells and pericytes. In the inside is the blood vessel lumen (*BVL*) and outside is the surrounding tissue (*ST*). Note the selected positions of different FT-IR spectra (*crosses*) to obtain an averaged FT-IR spectrum of the basal membrane

a curve-fitting procedure (another subroutine of Opus 4.2 software), by applying the "Report" obtained from MS given by the curve-fitting toolbox [15–18]. Each band was finally expressed as a percentage of the total amide I absorption area (covered by the bands between 1690 and 1615 cm^{-1}). Protein secondary structure parameters were further assessed using absorption bands assigned as α-helix, triple helix, β-sheets, β-turns, and unordered structure (% of total amide I absorption) as previously described [8, 14–17].

Statistics

All data (amide I absorption bands and secondary structure parameters) were used for comparisons between groups. All data were expressed as mean ± SD. A paired Student's *t*-test was used to determine differences between series of data between the two groups. *P*-values fixed at 0.01 and 0.05 were used to assess the significance of differences between series of data.

Results

Tumor description and data acquisition

All tumors were observed to grow rapidly after 10 to 13 days post-implantation. After resection, tumor volume of Group-21 mice (1.10±0.88 cm^3) was found to be five times larger than for Group-14 (0.22±0.19 cm^3; $P<0.05$). Xenografted tumors were removed and analyzed by FT-IR spectral imaging. Serial frozen sections of 20 µm thickness were used for FT-IR analyses.

Several capillary blood vessel locations were selected on every tissue section for FT-IR image acquisition referring to the immunohistochemistry sections (Fig. 1). Finally, 116 and 125 FT-IR images of capillary blood vessels, for Group-14 and Group-21 mice tissue sections, respectively, provided averaged spectra of sufficient quality for further data treatment (Supplementary material; Fig. S1).

Using second-derivative spectra to reveal all absorption bands within the 1750–1480 cm^{-1} spectral range, the curve-fitting procedure could be applied to every averaged FT-IR spectrum of each capillary blood vessel (Fig. 2). The absorption band exhibiting the highest intensity (Fig. 3)

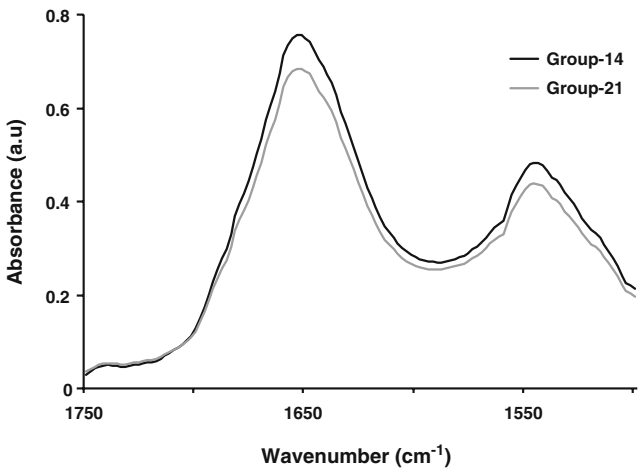

Fig. 3 Averaged FT-IR spectra of capillaries for group-14 and group-21 for the amide region 1750–1500 cm^{-1}

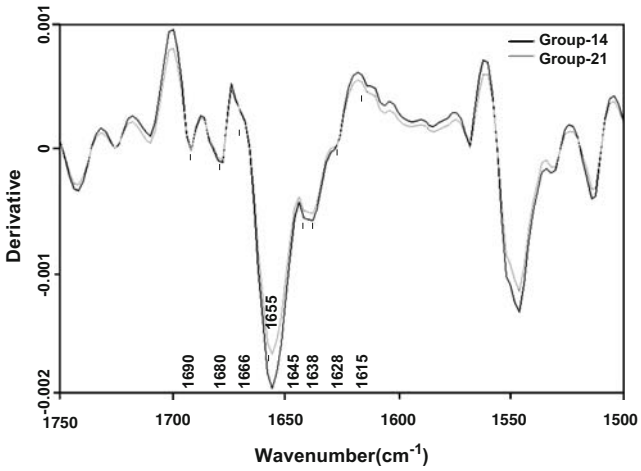

Fig. 4 Second-derivative of capillaries averaged FT-IR spectra for group-14 and group-21 for the amide region 1750–1500 cm^{-1} showing absorption bands to be used for curve fitting

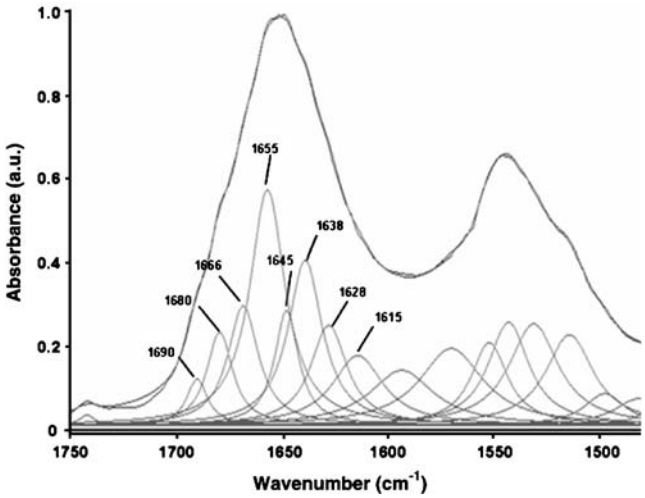

Fig. 5 Spectral curve fitting of the averaged spectrum of Fig. 2 showing the 1750–1480 cm^{-1} spectral range. Absorption bands of amide I are used for secondary structure determination: α-helix (1655 cm^{-1}), β-sheets (1690, 1680, and 1628 cm^{-1}), β-turns (1666 and 1615 cm^{-1}), unordered structure (1645 cm^{-1}), and triple helix (1638 cm^{-1})

was found to be centered at ~1655 cm^{-1} (amide I), which arises primarily from the ν(C=O) stretching vibrations of the amide groups of the protein backbone, while the absorption band centered at ~1545 cm^{-1} arises from the δ(N-H) bending vibrations (see also supplementary material, Fig. S1). Second-derivative MS (Fig. 4) of each group showed that all absorption bands within the amide I spectral range have very close wavenumbers (<2 cm^{-1} between groups), with differences only for maximum intensities per absorption band. The minimum values on second derivative spectra were at 1690, 1680, 1666, 1655, 1645, 1638, 1628, and 1615 cm^{-1} for the amide I spectral range. Spectral curve fitting could thus be performed after fixing bands at these values (Supplementary material; Table S1). To determine secondary structure parameters, as previously described [15, 16, 18], we assigned the bands centered at 1690 and 1625 cm^{-1} to parallel β-sheets, at 1680 cm^{-1} to anti-parallel β-sheets, and bands at 1666 and 1615 cm^{-1} were attributed to β-turns. The dominant band centered at 1655 cm^{-1} was assigned to the α-helix, the band centered at 1645 cm^{-1} was assigned to unordered structure, and the band centered at 1638 cm^{-1} to the triple helix of collagen (Fig. 5). Percentages of the three β-sheets bands were added together, and for the two β-turn bands.

Secondary structure of protein contents

Using the whole set of capillaries, curve fitting results showed that Group-21 had a higher percentage of the 1666 cm^{-1} absorption band (one of the β-turn absorption bands; 14.2±2.28 vs. 13.7±2.03%; $P<0.05$) but a lower percentage of the 1638 cm^{-1} absorption band (triple helix; 13.7±2.55 vs. 14.5±2.41; $P<0.05$). Capillary blood vessels were further divided into two groups, with respect to their diameter (∅ < and > 20 μm), to search for the category of capillary ("young" if ∅ < 20 μm; "old" if ∅ > 20 μm) that could be responsible for the differences obtained between groups. Sixty-four and fifty-one blood capillaries with diameter <20 μm were obtained for Group-14 and Group-21, respectively, and 52 vs. 74, respectively, for ∅ > 20 μm. For capillaries with ∅ < 20 μm, only the band at 1680 cm^{-1} (one of the three β-sheet bands) was significantly higher for group-21 than for group-14 (7.7±1.76 vs. 7.1±1.14; $P<0.05$). For capillaries with ∅ > 20 μm, only the percentage of the 1638 cm^{-1} absorption band was higher in Group-14 than Group-21 (15.1±2.41 vs. 14.0±2.64; $P<0.05$; see also Tables S3 and S4 in online supplementary material).

Secondary structure parameters for the whole set of capillaries (Table 1) showed that no significant difference ($P>0.05$) could be found for α-helix, β-sheets, and unordered structure. However, the percentage of β-turns was found to be significantly higher for Group-21 (28.8±3.21%) than for Group-14 (27.7±2.79%; $P<0.01$). This significant increase in β-turn content was ~4%. Conversely, the triple-helix content was lower for Group-21 than for Group-14 by ~−5.5%.

Only the capillaries of ∅ > 20 μm were significantly different between groups, for β-turn (27.3±2.84% vs. 28.8±3.24%; $P<0.01$; ~4% increase) and triple-helix (15.1±2.41% vs. 14.0±2.64%; $P<0.05$; ~7.3% decrease) content of secondary structure (Tables 2 and 3).

Finally, the secondary structure of proteins was compared with regard to tissue section location within the tumor (periphery vs. center). When considering the whole set of capillaries (all diameters), no significant difference could be

Table 1 Secondary structure determination of VBM protein contents for Group-14 and Group-21 mice

	α-Helix	β-Sheets	β-Turns	Unordered	Triple helix	Capillary diameter
Group-14	26.2±4.35	21.2±3.31	27.7±2.79	10.5±2.56	14.5±2.41	21.7±5.36
Group-21	25.6±4.10	21.2±3.11	28.8±3.21	10.7±2.44	13.7±2.55	22.9±5.02
t-test	0.244	0.942	0.005**	0.479	0.024*	0.067

Significant differences between groups: *$P<0.05$; **$P<0.01$. Absorption bands used for protein secondary structure determination: α-helix (1655 cm^{-1}), β-sheets (1690, 1680, and 1628 cm^{-1}), β-turns (1666 and 1615 cm^{-1}), unordered structure (1645 cm^{-1}), and triple helix (1638 cm^{-1}). n=116 and 125 spectra for Group-14 and Group-21 mice, respectively

Table 2 Secondary structure determination of VBM protein contents for Group-14 and Group-21 mice for all capillaries of diameter <20 μm

	α-Helix	β-Sheets	β-Turns	Unordered	Triple helix
Group-14	26.9±4.62	20.9±3.51	28.0±2.74	10.2±2.70	14.0±2.32
Group-21	26.9±3.55	20.6±3.09	28.7±3.20	10.4±2.27	13.4±2.40
t-test	0.988	0.546	0.182	0.739	0.234

n=64 and 51 spectra for Group-14 and Group-21 mice, respectively

found with regard to tissue section location (P>0.05 for all comparisons; data not shown). Again, no significant difference could be found when considering capillaries with ∅ < or > 20 μm (P>0.05 for all comparisons).

Discussion

Previous studies demonstrated that FT-IR spectroscopy is a useful complement to established histopathology methods for identification and classification of tumors [19]. It is now believed that FT-IR spectral imaging might play a central role in this context because ex-vivo analytical methods are still lacking to help neurosurgeons in the extemporaneous examination of tumor resection [17].

In recent studies, the metabolic status of cells could be determined by FT-IR spectral imaging within glioblastoma tissue sections [9]. Metabolic changes in tumors were due to the ischemic condition of cells within the tumor mass and highlighted high angiogenic stress [9]. However, the high heterogeneity of gliomas requires that other molecular markers are used to improve the diagnostic performance of FT-IR spectral imaging for such tumors. Thus, the aim of this study was to assess the potential of FT-IR spectral imaging as a molecular probe of tumor progression in highly angiogenic tumor specimens. It was used to analyze changes in capillary (probably VBM) protein content with tumor growth. We compared tumors removed on days 14 and 21 after tumor cell implantation from two groups of six mice. In every tumor approximately 20 blood capillaries were analyzed.

During angiogenesis, VBM is degraded and disassembled to be finally reorganized to a native state around a newly formed capillary. Collagens (especially type IV) are the main components of BM proteins (at least 50%) [12]. The VBM of tumor capillaries is characterized by variable diameter, swelling, vacuolization, and degeneration. These changes in collagen assembly and disposition in VBM exposed to the cancer angiogenic stress are now regarded as sub-molecular targets for tumor imaging and diagnostic [17].

To analyze capillary blood vessels by FT-IR spectral imaging, a curve-fitting procedure was proposed to determine the changes in the secondary structure of proteins at two moments of tumor growth (14 and 21 days). The second-derivative spectrum was used for positioning of amide I absorption bands, which were further fixed on the curve-fitting process. Furthermore, as collagen remodeling occurs through changes in their structure, more biological sense could be given to the data obtained by comparing the secondary structure results between tumor groups rather than by comparing results for every absorption band of the amide I spectral range. As an example, only one of the two β-turn absorption bands (1666 cm^{-1}) exhibited a significant difference between groups while comparing the whole set of capillaries. However, biological interpretation of this single β-turn absorption band change is not possible. One may also consider that "statistical" significance has no systematic biological sense. Conversely, when secondary structure results were used, i.e., with the combination of the two β-turn absorption bands, a significant difference (~4% increase) could be found between groups for capillaries with diameter >20 μm. This example illustrates the usefulness of using secondary structure parameters rather than individual bands of the amide I spectral range. A converse example was found for β-sheets absorption bands. Among the three bands of this secondary structure parameter, only one (1680 cm^{-1}) exhibited a significant difference between groups for capillaries with diameter <20 μm. One may question this peculiar (artifact?) result, because no other significant difference in the amide I absorptions counterbalanced this higher β-sheet content. Again, no result reinforced this β-sheet absorption difference while comparing groups using results in terms of secondary structure

Table 3 Secondary structure determination of VBM protein contents for Group-14 and Group-21 mice for all capillaries of diameter >20 μm

	α-Helix	β-Sheets	β-Turns	Unordered	Triple helix
Group-14	25.3±3.88	21.5±3.06	27.3±2.84	10.8±2.37	15.1±2.41
Group-21	24.6±4.21	21.7±3.05	28.8±3.24	10.9±2.54	14.0±2.64
t-test	0.343	0.746	0.007**	0.755	0.015*

Significant differences between groups: *P<0.05; **P<0.01. n=52 and 74 spectra for Group-14 and Group-21 mice, respectively

parameters. Finally, from the biological point-of-view, there is circumstantial evidence that young blood capillaries are globally comparable in structure and maturation, and this whatever the "age" of the tumor. It is usually on bigger blood capillaries that structural alterations appear due to angiogenic stress and ischemia [20].

Our results also showed a significant decrease in the 1638 cm^{-1} centered absorption with tumor growth. The triple-helix is certainly a major contribution to this band [14, 21], but the possibility that other structural motifs, for example β-turns, also contribute within this spectral range cannot be ruled out [13]. The decrease in triple helix absorption suggested the unfolding or degradation of collagen contents during the capillary sprouting process of angiogenesis and tumor growth. Thus, a decrease in the 1638 cm^{-1} absorption might be regarded as a molecular marker for functional FT-IR spectral imaging of angiogenic tumors. Conversely, a significant increase in β-turns contents was also found along tumor growth which counterbalanced the decrease in triple helix.

These results support previous studies [22] that reported the presence of collagen fibers irregularly disposed in blood capillaries of astrocytic tumors. This collagen decrease may support two hypotheses:

1. tumor necrosis induced degradation of proteins, or
2. the angiogenesis stress increased with tumor stage.

The decrease in triple helix content was not likely to be because of the formation of necrotic areas, because there was no significant difference in triple helix content for capillaries found at the center of the tumor, which area should also have been the most subject to necrosis. Besides, a 5.5% reduced level was found for the whole set of capillaries and 7.3% for "old" capillaries (diameter >20 μm). There is thus circumstantial evidence to support the hypothesis that angiogenic stress of tumors induced a high rate of degradation/remodeling of VBM proteins [12], which could be detected only on the biggest capillaries. One may also consider that, in biology, subtle changes in protein structure (a few percent in given conformational parameters) may result in major functional changes.

However, these small, although significant, differences observed between the two experimental groups in this work open two commentaries. First, these slight changes in VBM protein content with tumor growth could explain the lack of analytical studies on collagen structure changes during angiogenesis. Second, and as a consequence of the first commentary, FT-IR spectral imaging offers a unique opportunity to detect very subtle changes in protein structure during tumor formation. More analyses and comparisons with healthy capillaries, certainly with the same phenotypes of cells, could be useful to confirm the assumption and to assess these subtle changes detected in our study. Therefore, by combination of protein secondary structure markers with other molecular markers of tumor physiological status, notably metabolic [9], this functional imaging technique might be proposed as a useful diagnostic tool for surgeons and histologists. Although chemometric methods and data treatment are limited, because we cannot treat all the spectra of an image, methods based on FT-IR spectroscopy have emerged and developed rapidly during recent decades.

Conclusion

This study has shown that the triple helix and β-turn content of the secondary structure of VBM proteins might be used as molecular markers for functional FT-IR spectral imaging of tumor growth. This functional imaging appears as a promising technique to rapidly generate multi-parametric information on tumors, and opens the way to the development of a molecular histopathology, which might become a useful analytical tool for neurosurgeons.

References

1. Vajkoczy P, Menger MD (2000) J Neurooncol 50:99–108
2. Dukor RK (2002) In: Chalmers JM, Griffiths PR (eds) The handbook of vibrational spectroscopy, vol. 5. Wiley, Chichester, pp 3335–3361
3. McDonald DM, Choyke PL (2003) Nat Med 9:713–725
4. Crupi V, De Domenico D, Interdonato S, Majolino D, Maisano G, Migliardo P, Venuti V (2001) J Mol Struct 563–564:115–118
5. Li MJ, Hsu HS, Liang RC, Lin SY (2002) Ultrastruct Pathol 26:365–370
6. Neviliappan S, Fang KL, Tiang LWT, Arulkumaran S, Wong PT (2002) Gynecol Oncol 85:170–174
7. Yang Y, Sule-Suso J, Sockalingum GD, Kegelaer G, Manfait M, El Haj AJ (2005) Biopolymers 78:311–317
8. Petibois C, Drogat B, Bikfalvi A, Deleris G, Moenner M (2007) FEBS Lett 581:5469–5474
9. Petibois C, Gionnet K, Goncalves M, Perromat A, Moenner M, Deleris G (2006) Analyst 131:640–647
10. Sivridis E, Giatromanolaki A, Koukourakis MI (2003) J Pathol 201:173–180
11. Folkman J (1990) J Nat Cancer Inst 82:4–6
12. Kalluri R (2003) Nat Rev Cancer 3:422–433
13. Smith DJ, Roberts D (1994) Clin Biochem 27:435–440
14. Petibois C, Gouspillou G, Wehbe K, Delage JP, Deleris G (2006) Anal Bioanal Chem 386:1961–1966
15. Fabian H, Naumann D (2004) Methods, San Diego, Calif, 34:28–40
16. Troullier A, Reinstadler D, Dupont Y, Naumann D, Forge V (2000) Nat Struct Biol 7:78–86
17. Petibois C, Deleris G (2006) Trends Biotechnol 24:455–462
18. Goormaghtigh E, Ruysschaert JM, Raussens V (2006) Biophys J 90:2946–2957
19. Fernandez DC, Bhargava R, Hewitt SM, Levin IW (2005) Nat Biotechnol 23:469–474
20. Carmeliet P (2003) Nat Med 9:653–660
21. Lee SM, Lin SY, Liang RC (1995) Artif Cell Blood Substit Immobil Biotechnol 23:193–205
22. Arismendi-Morillo G, Castellano A (2005) J Neurooncol 73:211–217

Paper III

- PAPER 3-

Differentiation between normal and tumor blood vessels in xenografted brain tumors by FTIR spectral imaging

---

To be submitted

Purpose: FTIR spectral imaging was envisaged to get reliable molecular markers to differentiate between normal and tumor blood vessels. U87 pcDNA3 and U87 IRE1 DN human glioma cells were selected for the study as an established model for malignant glioma that form highly vs. poorly vascularized tumors, respectively. They were implanted intracranially in Rag-gamma mice for 28 days. Classical pathological examination and immunohistochemistry were performed in parallel to the FTIR imaging of brain tissues (with both healthy and tumor parts) for validation of FTIR results.

Background: Brain tumor formation and growth is accompanied by the sprouting and proliferation of blood capillaries towards the tumor cells for ensuring their nutrients and oxygen intake. Structural and functional abnormalities of the vascular microenvironment are contributory to pathophysiological characteristics of gliomas. Angiogenesis and functions of resultant vessels differ significantly between the same tumors grown in different host organs. With the presence of the blood brain barrier, a significantly higher amount of VEGF is required to induce vascular hyperpermeability in normal vessels in the cranial window than in the dorsal skin chamber. On the other hand, the cranial environment is more angiogenic and forms new vessels faster than the subcutaneous tissue in response to a given angiogenic factor. Therefore, for this study, we preferred to test intracranially implanted tumors to better present the histopathological environment of the human GB.

Main results: FTIR spectral imaging of tissues was followed by a hierarchical analysis (HA) of spectra corresponding to pixels covering blood capillaries. Two combined spectral intervals of fatty acyl (3020-2800 cm^{-1}) and carbohydrates (1180-950 cm^{-1}) of first derivative FTIR spectra allowed to obtain classification of blood capillaries, with one cluster of spectra corresponding to the healthy blood vessels and another cluster for the tumor blood vessels. High heterogeneity level (H = 2.22) could be obtained between clusters (h = 0.2 for cluster of healthy blood vessels and h = 0.1 for cluster of tumor blood vessels). The results outlined by the use of these spectral intervals in classification also suggest a higher unsaturation level of fatty acyl chains contained in phospholipids and a lower level of saccharidic residues than for normal BV. As an example, the ν=(CH)/$\nu_{as}(CH_3)$ ratio was increased for tumor BV with respect to normal ones, while a concomitant decrease was found for the $\nu_{as}(CH_2)/\nu_{as}(CH_3)$ ratio, thus providing evidence of larger unsaturation of fatty acyl chains in the cells of tumor BV. Concerning the carbohydrates spectral interval (1180-950 cm^{-1}) that also differentiated BV, an absorption band at ~ 1068 cm^{-1} was observed in normal BV spectra but not in tumor ones. Furthermore, we tested spectra from human endothelial cells from two different origins (cerebral and umbilical vein), and we confirmed the presence of the band in the first type. We have temptatively assigned this absorption band to the presence of mannosyl residues since comparison with spectra of some sugars pure products showed that only the mannose FTIR spectrum presents this absorption band. Moreover when this classification was applied on the invasive phenotype of tumors, it allowed define the tumor area by indicating the positions of tumor BV. So we can conclude that these two spectral intervals of BV FTIR spectra contain discriminant markers to distinguish healthy and tumor areas of brain tissues and thus to define the tumor limits.

Contribution to a "molecular histology of brain glioma": These findings demonstrate that FTIR spectral imaging was able to detect changes on a molecular level between healthy and pathological BV. Thus, it might become a valuable analytical method in molecular histopathology for brain tumor diagnosis.

Differentiation between normal and tumor blood vessels in xenografted brain tumors by FTIR spectral imaging

Katia Wehbe[1], Raphael Pineau[2], Michel Moenner[2], Cyril Petibois[1], and Gérard Déléris[1]

1: CNRS UMR 5084, CNAB, Université Victor Segalen Bordeaux 2, 146 Rue Léo Saignat, 33076 Bordeaux-Cedex, France

2: INSERM U 920, Université Bordeaux 1, Avenue des Facultés, 33405 Talence-Cedex, France

Corresponding author: Dr. Cyril Petibois, PhD.

Université Victor Segalen Bordeaux 2

CNRS UMR 5084, CNAB

146 rue Léo Saignat

F-33076 Bordeaux-Cedex, France

cyril.petibois@u-bordeaux2.fr

Abstract

Brain tumor growth is accompanied by the sprouting of new blood vessels (BV). Structural and functional abnormalities of the vascular microenvironment are contributory to pathophysiological characteristics of gliomas. Imaging the differences between healthy and tumor tissues on the basis of blood vessels would be helpful for a clear diagnosis and therapeutic follow-up of brain cancers. In this study, we used FTIR spectral imaging to differentiate between normal and tumor blood vessels from intracranialy xenografted tumors in Rag-gamma mice 28 days after implantation. Classification of the spectra corresponding to pixels covering the capillary blood vessels succeeded by using spectral intervals of fatty acyl (3050-2800 cm^{-1}) and carbohydrates (1180-950 cm^{-1}) absorptions, with the formation of two clusters. Heterogeneity between clusters (H = 2.22) was significantly higher than for every population of spectra (h = 0.2 and 0.1 for healthy and tumor BV spectra, respectively). Data treatment based on these two spectral intervals provided interpretative information about molecular contents involved in the differentiation between healthy and tumor BV, the later presenting higher fatty acyl chain unsaturation from phospholipids and an unexpected loss of absorption from saccharidic residues. These findings demonstrate that FTIR imaging could potentially serve to highlight molecular probes for differentiation between normal and tumor blood vessels, and might thus become a valuable tool for pathologic examination of brain tumors.

Abbreviations

FTIR: Fourier Transform Infrared ; BV : blood vessels ; DN : dominant negative ; HA : Hierarchical analysis

Keywords

FTIR spectral imaging, gliomas, angiogenesis, molecular markers, hierarchical analysis

Introduction

Many brain tumors are characterized by rapid growth and infiltration of healthy tissue [1]. Remodeling of the tumor microvasculature is essential for adequate tumor tissue oxygenation and nutrients supply. Thus, the vascular environment determines pathophysiology of gliomas, such as edema formation, and tumor cell invasiveness [2]. The resulting vessels are structurally and functionally abnormal, and contribute to a hostile microenvironment (low oxygen tension and high interstitial fluid pressure), leading to a more malignant phenotype with increased morbidity and mortality [3]. Moreover, the effectiveness of radiotherapy, chemotherapy, or immunotherapy critically depends upon the successful drugs delivery by blood transporters [2]. Thus, a better understanding of the molecular basis of vascular normalization may ultimately lead to more effective therapeutic follow-up not only for cancer but also for diseases with abnormal vasculature, in which the goal is to maintain a functionally normal vasculature [4]. Nevertheless, whatever the objective of the clinician's intervention, being able to image blood capillaries for discriminating healthy and tumor tissues is a major issue of brain cancer research.

Many articles have described and illustrated ultrastructural abnormalities in brain tumors such as fenestrations, endothelial gaps, pinocytotic vesicles, and trans-endothelial channels, but only a few have attempted to quantitate these changes in either experimental or human brain tumors, and only recently has anyone attempted to interrelate structure and function. The glioma vessel morphology is highly heterogeneous and different from the physiological microvasculature in brain tissue. Gliomas contain tortuous and sinusoidal vessels. Concerning their size, cerebral capillaries (~3–5 μm in diameter) are smaller than, those in gliomas (diameters ranging between 3 and 40 μm) due to endothelial cell hyperplasia [2, 5]. Pericytes and the basement membrane of tumor vessels also reveal significant abnormalities versus cerebral vessels.

Actually, the histological study of brain exereses uses conventional light microscopic studies and immunohistochemical staining for endothelial cell markers, such as factor VIII-related antigen (von Willebrand factor), as well as CD31 (PECAM) or CD34,

which allowed identifying high-grade gliomas as one of the most intensively vascularized tumors reflecting a high angiogenic activity of these tumors [2]. Although not usable in the clinical routine for diagnostic purposes, transmission electron microscopic analyses have also gained further insight into ultrastructural alterations of the glioma vessel wall and potential transvascular transport mechanisms [6, 7]. *In vivo* phage display was also used to analyze differences between the normal and diseased microvasculature in order to identify and localize novel vascular markers in cancer, and to characterize changes that occur during tumor progression [8]. All these techniques are limited for routine use, time consuming and also expensive. Moreover, they lack of molecular markers of tumor blood vessels. There is thus no reliable molecular marker to differentiate between normal and tumor blood vessels. Recently, Fourier transform infrared (FTIR) micro-spectroscopy has been proposed for the non-destructive determination of structural and chemical/physical properties of biological systems at the molecular level. In particular, new methodologies have been developed to examine and distinguish between normal and pathological tissues by FTIR means, spectroscopy, microscopy or imaging. Main advantages of this method include the global information provided about the sample molecular contents, its great sensitivity and reproducibility, and no sample contents modification is required before analysis.

A number of studies have utilized FTIR spectroscopy and chemometric based spectral data treatments for tumor detection and classification of tissue samples, including cervical [9], skin [10], prostate [11], colon [12], lung [13], and breast [14]. However, only a few studies focused on the brain tissue [15-18]. To our knowledge, there is no report of study on blood vessels characterization by FTIR spectral imaging. In this study, FTIR spectral imaging was used to differentiate between normal and tumor blood vessels of xenografted brain tumors in Rag-gamma mice 28 days after intracranial implantation. Two cell phenotypes were compared by FTIR spectroscopy after cell culture and also by FTIR spectral imaging after intracranial tumor formation.

Materials and methods

Cell culture

U87 pcDNA3 and U87 IRE1 DN human glioma cells were selected for the study as an established model for malignant glioma that form highly vs. poorly vascularized tumors, respectively [19]. Cells were grown in Dulbecco's modified Eagle's medium (DMEM), 1g/L glucose supplemented with 10% FBS, L-glutamine, and antibiotics. Cell culture was performed in a 37°C-incubator with humidified atmosphere and 5% CO_2. Cells were grown to confluence, centrifuged after trypsinization, and re-suspended in serum free DMEM for injection.

Endothelial cells (HCMEC and HUVEC) were grown on plastic tissue culture flasks in EGM-2 growth medium containing FBS and growth supplements. [20] EBM-2 medium was supplemented with VEGF, IGF-1, EGF, basic FGF, hydrocortisone, ascorbate, gentamycin and 2.5% fetal bovine serum (FBS) as recommended by the manufacturer. The cultures were maintained at 37°C in 5% CO2 and EGM-2 medium was replaced every 3 days until the cells reached confluence. After trypsinization and centrifugation, the pellets of cells were diluted 10 times in distilled water for lysates preparation in order to be analyzed by FTIR spectroscopy.

Intracranial tumors

Six to eight week-old male Rag-gamma immunodeficient mice (n=8) with an average weight of 26 g were used for this experiment (n=6 for the U87 pcDNA3 and n=2 for U87 IRE1 DN). Animals were anesthetized using Imalgene 1000 (Ketamin 10 g/100 ml) injected intraperitoneally. Their head was mounted into a stereotactic head holder in a flat-skull position. Cell implantations (in the left hemisphere) were at 2.2 mm lateral to the bregma and 3 mm in depth using U87 cells. U87 glioma cells ($5.6x10^5$ cells per animal) were suspended in 3 µl of free DMEM media. Twenty-eight days post-injection (average weight of mice was about 22 g), animals were sacrificed by cervical dislocation. Brains of the sacrificed mice were dissected from the cranial cavity and washed in PBS solution. Then, brains were placed individually in tubes without fixatives before to be frozen in liquid N_2 and stored at -80°C until analyses.

Tissue samples

Frozen brains were covered by cooled glue (polyvinyl alcohol for cryostat, -20°C) before slicing. Serial coronal sections (Cryostat 3050-TM, Leica-Microsystems, France) of 20 µm in thickness were transferred onto a ZnSe windows for FTIR spectro-imaging. All tissue sections were dried on air before further processing. For obtaining the highest comparison level of data, immunohistochemistry was performed on the same tissue sections (on ZnSe windows) after FTIR image acquisition. Finally, 5 tumors out of 6 samples were found to be formed for the U87 pcDNA3 phenotype were developed, and 2 sections per sample were analyzed. Comparisons were performed on formed tumors only.

FTIR spectral imaging acquisition

Spectral images were collected in transmission mode using a Spotlight 300 FTIR imaging system, equipped with a Spectrum One spectrometer (Perkin-Elmer). The imaging system was equipped with a liquid N_2-cooled MCT linear detector comprising 16 pixel elements. FTIR images were collected from samples in normal and tumor areas, in the 4000-720 cm^{-1} range using 8 scans with a spectral resolution of 4 cm^{-1} and a spatial resolution of 6.25*6.25 µm per pixel (4X magnification of the physical 25*25 µm dimension of detectors). Spectral intervals of interest in the tissue sections were selected referring to the immunohistochemical sections on slides.

Immunohistochemistry

Immunohistochemistry was used to highlight all blood vessels of tumor sections and for further comparisons with FTIR analyses. We used CD31 also designated as PECAM-1 (platelet endothelial cell adhesion molecule 1) as a marker for benign and malignant vascular tumors. The 20 µm sections were fixed in paraformaldehyde 4%. Endogenous peroxidase was inhibited using 3% H_2O_2 in distilled water. The sections were then washed in phosphate buffered saline. Slides were incubated first with the primary antibody (purified rat anti-mouse monoclonal antibody, pharmingen BD Biosciences), for CD31 (1:100). Incubation was performed for 2 hours at room temperature in a humidified chamber. After washing, the slides were then incubated with goat anti-rat biotinylated polyclonal antibody (1:200, pharmingen BD Biosciences) for one hour at room temperature. Sections were then washed and incubated with standard avidin–biotin complex (Vectastain Elite kit ABC, Vector

Laboratories) for 30 min. Antibody binding was revealed using H_2O_2 as a substrate and diaminobenzidine as chromogen.

Data processing and analysis

Once the visible image of the same area of IR images done on ZnSe windows was obtained after immunohistochemistry, capillary blood vessels were searched and one averaged spectrum was obtained per capillary. For each sample, 40 spectra were chosen from the 2 sections (20 spectra for normal blood vessels from cerebral cortex and 20 for tumor vessels from tumor region). After baseline correction, spectra were subjected to hierarchical analysis (HA) using Ward's algorithms of OPUS 4.2 software (Bruker, Germany). In such a classification method, all data points (absorbance values) from individual spectra are compared based on their Euclidean distance to the average of spectra included in the database. Calculation of distances leads to the classification of spectra under the form of a dendrogram, with the formation of clusters containing the most comparable spectra and heterogeneity levels between clusters. To be significant, heterogeneity value (referred to as *H*) between two clusters must be above the sum of the clusters' heterogeneity (referred to as *h*) values [21]. Classification was performed on the first derivatives of the spectra with 5-point smoothing on different spectral intervals.

FTIR spectrometry for cell lysates

Cells lysates were homogenized with an agitator. 35 µL of each was deposited on 96-well silicon-microplate (sample deposition area 7 mm in ∅). The microplate was placed in a drying vaccum to evaporate water (45 min), then it was finally put into the analysis compartment of a Bruker Tensor 27 spectrometer combined to a HTS-XT sample compartment and equipped with a Globar (MIR) source (7 V), a KBr beamsplitter, and a DTGS/B detector (18–28 °C). We used a resolution of 2.0 cm^{-1}, and acquisitions were performed using 32 scans. All analyses were performed in triplicate and spectra were averaged before data treatments [22].

Results

Spectra classification

For every brain sample, two tissue sections were used to select 20 healthy blood capillaries and 20 tumor blood capillaries ***(Figure 1)***. 15 out of 20 blood capillaries were randomly selected within each group for the classification and the 5 remaining blood capillaries were used to test and validate our method. Spectra classification with Ward's algorithm was used for data analysis on the first derivatives of the spectra with a 5-point smoothing. Classification was tested for the spectral intervals presenting the most important heterogeneity of absorbances between spectra, which could be selected using the second derivative of spectra. The spectral intervals used included absorptions of fatty acyl chains (3020-2800 cm^{-1}), lipid esters (1776-1720 cm^{-1}), proteins amide I and II (1712-1500 cm^{-1}), and carbohydrates (1180-950 cm^{-1}). Spectra classification was performed for every sample (n = 15 healthy + 15 tumor blood capillaries) and for the whole set of spectra (n = 5 samples; n = 75 healthy + 75 tumor blood capillaries). Spectra classification was found to provide two distinct clusters between healthy and tumor blood capillaries using fatty acyl chain (3020-2800 cm^{-1}) and carbohydrates (1180-950 cm^{-1}) spectral intervals with high hetereogeneity level between clusters **(*Table 1*)**. To test the classification method, we used the left 10 spectra for each sample (5 normal and 5 tumor blood capillaries), so in the global classification of all samples 50 spectra were added to the previous 150 spectra (as total, n = 100 healthy + 100 tumor blood capillaries) These added spectra were found to be inserted in their respective cluster, thus demonstrating the robustness of the classification method with an increase in heterogeneity level between clusters ***(Figures 2A, 2B, 3A and 3B)***.

Fatty acyl spectral interval

In order to interpret the spectral differences revealed by the spectra classification for fatty acyl chain absorptions, spectra were curve fitted for the spectral interval 3050-2800 cm^{-1}. The positions of each absorption band were determined using the second derivative spectrum corresponding for every blood capillary ***(Figure 4)***. The minimum values on second derivative spectra allowed to determine absorption bands at 3033, 3012, 2959, 2921, 2899, 2871, and 2851 cm^{-1}. Spectral curve fitting procedure could

thus be performed after fixing bands at these values ***(Figure 5).*** A model of curve fitting was first obtained for this spectral interval from the average of all spectra (n = 200). This model was then used to analyze all individual spectra. Spectral areas of the following absorption bands were extracted from curve fitting procedure: 3012 cm^{-1} for ν=(CH), 2959 cm^{-1} for $\nu_{as}(CH_3)$, and 2921 cm^{-1} for $\nu_{as}(CH_2)$. These absorptions are mainly due to the asymmetric stretching mode of the fatty acyl moieties of membrane phospholipids. Fatty acyl chain unsaturation may be appreciated using the following absorption band ratios: ν=(CH)/$\nu_{as}(CH_3)$ and $\nu_{as}(CH_2)/\nu_{as}(CH_3)$ [23]. The ν=(CH)/$\nu_{as}(CH_3)$ ratio increased in the tumor with respect to normal blood vessels (49% increase), a concomitant decrease being observed for the $\nu_{as}(CH_2)/\nu_{as}(CH_3)$ ratio (28% decrease; ***Tables 2 and 3***). A verification of this result was obtained by using also the symmetric bands of methyl $\nu_s(CH_3)$ and methylene $\nu_s(CH_2)$ groups ***(Table 4).***

Carbohydrates spectral interval

Spectra classification based on this spectral interval gave two clear clusters. Second derivatives of spectra highlighted a difference between healthy and tumor blood vessels for an absorption band centered at ~1068 cm^{-1}, which was not found in the spectra of tumor blood capillaries, and the band centered at 1025 cm^{-1} was found with reduced intensity with respect to spectra of healthy blood capillaries ***(Figure 6)***. As shown in table 1, the absorption of the band centered at 1068 cm^{-1} provided about most of the heterogeneity level in classification while using the carbohydrates spectral interval. Moreover, when combined with the fatty acyl chain spectral interval, the same heterogeneity level was obtained for each sample (n = 40 spectra) and for the whole set of samples (n = 200 spectra).

Application of the spectra classification model to a second type of tumors

U87 IRE1 DN tumors were characterized by their invasiveness and poor vascularization, so it was difficult to differentiate between healthy and tumor capillaries. After choosing randomly 100 BV spectra of U87 IRE1 DN derived tumors, they were inserted in the model of classification established on the first type of tumors (U87 pcDNA3 derived tumors) to be tested whereas they are normal or tumor. 34 and 26 spectra out of 100 for each of the two tumors of U87 IRE1 DN were

classified with the tumor class respectively. Referring to tissue sections of each tumor, the positions of capillaries for these spectra were exactly around the tumor area or inside the tumor ***(Figure 7)***.

Endothelial cells lysates spectra

Cell lysates were analyzed by FTIR spectroscopy to determine if endothelial cells of brain blood capillaries could be specific of the differentiation found between healthy and tumor blood capillaries by FTIR imaging. Second derivative spectra of cell lysates ***(Figure 8)*** revealed the presence of the band at 1068 cm^{-1} (carbohydrates region) in the HCMEC (brain phenotype) and its absence in HUVEC (umbilical phenotype).

Discussion

Most tumor capillaries have an irregular diameter and random branching, and they do not fit well into the usual classification of arterioles, capillaries or venules [24]. They show structural and functional abnormalities in all components of the blood vessel wall. These abnormalities, which are the product of soluble and matrix-associated factors from tumor and stromal cells, have physiological consequences. Much excitement has been generated by the idea of attacking and destroying tumors by exploiting abnormalities of their blood capillaries. More studies are necessary to better understand differences between normal and tumor blood capillaries at the molecular level; because this could provide the opportunity to destroy tumor vasculature without destroying that of normal tissues [3].

We suggested [25] that FTIR spectral imaging could be taken into consideration for the development of new molecular histopathology tools. The results obtained in this study using FTIR spectral imaging and spectroscopy allowed to highlight potential molecular markers differentiating healthy and tumor blood capillaries.

Spectra classification based on spectral region of lipids (1776-1720 cm^{-1}) discriminated healthy and tumor blood capillaries into two distinct clusters for several samples and with higher heterogeneity level than using the carbohydrate spectral

interval (0.81 *vs.* 0.31, respectively). However, this spectral interval exhibits very weak absorption intensity, and may be found null for spectra presenting small absorbance level. Thus, this spectral interval was not taken into consideration for establishing a classification model.

Spectra classification based on amide spectral interval (1712-1500 cm^{-1}) did not allow for a good discrimination between blood capillaries. We could expect that such result could not be obtained on this spectra classification, although it was previously demonstrated that this spectral interval could contain spectral markers for differentiating tumor blood capillaries at different tumor stages. These markers were mainly based on the secondary structure of protein contents found in vascular basement membranes and changed during angiogenesis [26]. They accounted for no more than a few % in terms of repartition between α-helix, β-sheets, triple helix…etc. contents. These changes were mainly due to different repartitions between collagen types I and IV [27]. Therefore, the classification using the whole spectral interval covered by amide absorptions is too large to distinguish between healthy and tumor blood capillaries on the sole basis of these subtle differences.

The spectra classification using the spectral interval 3020-2800 cm^{-1}, alone or combined with the carbohydrates spectral interval, provided the highest heterogeneity levels between the two spectra populations. The two clusters obtained did not presented overlap between spectra. Adding the carbohydrate spectral interval (1180-950 cm^{-1}) led also to the formation of two clusters with a comparable heterogeneity level. From the curve-fitting of the 3020–2800 cm^{-1} spectral interval, we could find that ν=(CH)/$\nu_{as}(CH_3)$ ratio increased for tumor blood capillaries spectra with a parallel decrease in the $\nu_{as}(CH_2)/\nu_{as}(CH_3)$ ratio. These changes in fatty acyl chain absorptions revealed that phospholipids of vascular cells (the most important source of fatty acyl chains in blood capillaries) could be more unsaturated in tumors than in healthy tissues. Therefore, one may consider that fatty acyl chain differentiation between healthy and tumor blood capillaries, is a valuable molecular and spectral marker for further functional FTIR imaging of brain tumors.

The molecular interpretation of classification model was also valid for the carbohydrates spectral interval (1180-950 cm^{-1}). In this spectral region, we found two discriminating bands especially that at 1068 cm^{-1}. This absorption band may be attributed to a saccharidic moiety, but comparison between pure product FTIR spectra of glucose, lactate, mannose, galactose, and glycogen would suggest that the bands centered at ~ 1068 and 1025 cm^{-1} should belong to a mannosyl residue [22]. Mannose considered as a free hexose is physiologically present in weak concentration in the brain. It is thus unlikely that the clear difference in the 1068 cm^{-1} absorption band intensity, would be due to the presence or not of mannose in this chemical form. It is also known that tumor cells are embedded in a network of protein-protein and protein-carbohydrate interactions mediated by a wide variety of glycoproteins, glycolipids, lectins and proteoglycans. Glycohistochemical analyses have shown that the binding capacity to saccharide epitopes in astrocytic tumors change protein-carbohydrate interactions in tumors [28]. This study has mentioned that markedly the level of binding site expression for α-D mannose decreases in the tumors, the perivascular tumor areas and the vessel walls. Moreover, the mannose receptor is a transmembrane glycoprotein mainly expressed by macrophages, dendritic cells, and endothelial cells that specifically binds to mannosylated molecules and mediates their endocytosis. Expression of the mannose receptor has recently been demonstrated in the brain. Astrocytes and microglia, two types of glial cells that can be turned into immune-competent cells, are the main sites of expression *in vivo* and *in vitro*. In a recent study, mannosylation of molecules and targeting of the mannose receptor have been used and tried successfully in antitumor response [29, 30]. Immunohistochemical studies revealed also a regional distribution of the mannose receptor varying with age, the site of the highest expression being the meninges and the cerebral cortex [30]. This may also explain the presence of mannosyl residues in normal cerebral capillaries and their absence in tumor blood capillaries. Furthermore, when cells lysates of two types of endothelial cells were studied by FTIR spectrometry, this discriminant band at 1068 cm^{-1} was present in the HCMEC originated from human cerebral microvasculature and absent in HUVEC originated from human umbilical vein, thus confirming the results obtained from brain tumors. Therefore, our results suggest that the absence of the band centered at 1068 cm^{-1} is another molecular and spectral marker of brain tumor blood capillaries with respect to their healthy counterpart.

In conclusion, our study has demonstrated that FTIR spectral imaging is a valuable analytical tool for determining the spectral and molecular differences between healthy and tumor blood capillaries. A classification model based on fatty acyl chain and carbohydrate absorptions could be obtained for discriminating 100% of the spectra representative of tumor and healthy blood capillaries. A basic molecular interpretation of these results could be obtained after curve fitting these spectral intervals. We could determine that fatty acyl chains of cell membranes phospholipids were probably more unsaturated in tumor samples. The absence of the 1068 cm^{-1} absorption band is probably related to the lack of a mannosyl residue in vascular endothelial cells of tumor blood capillaries. This study demonstrated that FTIR spectral imaging is a suitable imaging modality for developing molecular histology tools for brain tumor diagnostic purposes.

References

1. Unger RE, Oltrogge JB, von Briesen H, Engelhardt B, Woelki U, Schlote W, Lorenz R, Bratzke H & Kirkpatrick CJ (2002) Isolation and molecular characterization of brain microvascular endothelial cells from human brain tumors. *In vitro cellular & developmental biology* 38, 273-281.
2. Vajkoczy P & Menger MD (2000) Vascular microenvironment in gliomas. *Journal of neuro-oncology* 50, 99-108.
3. Jain RK, di Tomaso E, Duda DG, Loeffler JS, Sorensen AG & Batchelor TT (2007) Angiogenesis in brain tumours. *Nature reviews* 8, 610-622.
4. Jain RK (2005) Normalization of tumor vasculature: an emerging concept in antiangiogenic therapy. *Science (New York, NY* 307, 58-62.
5. Carmeliet P & Jain RK (2000) Angiogenesis in cancer and other diseases. *Nature* 407, 249-257.
6. Schlageter KE, Molnar P, Lapin GD & Groothuis DR (1999) Microvessel organization and structure in experimental brain tumors: microvessel populations with distinctive structural and functional properties. *Microvascular research* 58, 312-328.
7. Stewart PA, Farrell CL & Del Maestro RF (1991) The effect of cellular microenvironment on vessels in the brain. Part 1: Vessel structure in tumour, peritumour and brain from humans with malignant glioma. *International journal of radiation biology* 60, 125-130.
8. Pasqualini R, Arap W & McDonald DM (2002) Probing the structural and molecular diversity of tumor vasculature. *Trends in molecular medicine* 8, 563-571.
9. Neviliappan S, Fang Kan L, Tiang Lee Walter T, Arulkumaran S & Wong PT (2002) Infrared spectral features of exfoliated cervical cells, cervical adenocarcinoma tissue, and an adenocarcinoma cell line (SiSo). *Gynecologic oncology* 85, 170-174.
10. Crupi V, De Domenico D, Interdonato S, Majolino D, Maisano G, Migliardo P & Venuti V (2001) FTIR spectroscopy study on cutaneous neoplasie. *Journal of Molecular Structure* 563-564, 115-118.

11. Malins DC, Polissar NL & Gunselman SJ (1997) Models of DNA structure achieve almost perfect discrimination between normal prostate, benign prostatic hyperplasia (BPH), and adenocarcinoma and have a high potential for predicting BPH and prostate cancer. *Proceedings of the National Academy of Sciences of the United States of America* 94, 259-264.
12. Salman A, Argov S, Ramesh J, Goldstein J, Sinelnikov I, Guterman H & Mordechai S (2001) FTIR microscopic characterization of normal and malignant human colonic tissues. *Cellular and molecular biology (Noisy-le-Grand, France)* 47 Online Pub, OL159-166.
13. Yang Y, Sule-Suso J, Sockalingum GD, Kegelaer G, Manfait M & El Haj AJ (2005) Study of tumor cell invasion by Fourier transform infrared microspectroscopy. *Biopolymers* 78, 311-317.
14. Fabian H, Thi NA, Eiden M, Lasch P, Schmitt J & Naumann D (2006) Diagnosing benign and malignant lesions in breast tissue sections by using IR-microspectroscopy. *Biochim Biophys Acta* 1758, 874-882.
15. Bambery KR, Schultke E, Wood BR, Rigley MacDonald ST, Ataelmannan K, Griebel RW, Juurlink BH & McNaughton D (2006) A Fourier transform infrared microspectroscopic imaging investigation into an animal model exhibiting glioblastoma multiforme. *Biochim Biophys Acta* 1758, 900-907.
16. Amharref N, Beljebbar A, Dukic S, Venteo L, Schneider L, Pluot M, Vistelle R & Manfait M (2006) Brain tissue characterisation by infrared imaging in a rat glioma model. *Biochim Biophys Acta* 1758, 892-899.
17. Krafft C, Shapoval L, Sobottka SB, Schackert G & Salzer R (2006) Identification of primary tumors of brain metastases by infrared spectroscopic imaging and linear discriminant analysis. *Technol Cancer Res Treat* 5, 291-298.
18. Steiner G, Shaw A, Choo-Smith LP, Abuid MH, Schackert G, Sobottka S, Steller W, Salzer R & Mantsch HH (2003) Distinguishing and grading human gliomas by IR spectroscopy. *Biopolymers* 72, 464-471.
19. Drogat B, Auguste P, Nguyen DT, Bouchecareilh M, Pineau R, Nalbantoglu J, Kaufman RJ, Chevet E, Bikfalvi A & Moenner M (2007) IRE1 signaling is essential for ischemia-induced vascular endothelial growth factor-A expression and contributes to angiogenesis and tumor growth in vivo. *Cancer research* 67, 6700-6707.
20. Weksler BB, Subileau EA, Perriere N, Charneau P, Holloway K, Leveque M, Tricoire-Leignel H, Nicotra A, Bourdoulous S, Turowski P, Male DK, Roux F, Greenwood J, Romero IA & Couraud PO (2005) Blood-brain barrier-specific properties of a human adult brain endothelial cell line. *Faseb J* 19, 1872-1874.
21. Petibois C, Cazorla G, Gin H & Deleris G (2001) Differentiation of populations with different physiologic profiles by plasma Fourier-transform infrared spectra classification. *The Journal of laboratory and clinical medicine* 137, 184-190.
22. Petibois C, Rigalleau V, Melin AM, Perromat A, Cazorla G, Gin H & Deleris G (1999) Determination of glucose in dried serum samples by Fourier-transform infrared spectroscopy. *Clinical chemistry* 45, 1530-1535.
23. Petibois C & Deleris G (2004) Oxidative stress effects on erythrocytes determined by FTIR spectrometry. *Analyst* 129, 912-916.
24. Hashizume H, Baluk P, Morikawa S, McLean JW, Thurston G, Roberge S, Jain RK & McDonald DM (2000) Openings between defective endothelial cells explain tumor vessel leakiness. *The American journal of pathology* 156, 1363-1380.
25. Petibois C & Deleris G (2006) Chemical mapping of tumor progression by FTIR imaging: towards molecular histopathology. *Trends in biotechnology* 24, 455-462.

26. Wehbe K, Pinneau R, Moenner M, Deleris G & Petibois C (2008) FTIR spectral imaging of blood vessels reveals protein secondary structure deviations induced by tumor growth. *Anal Bioanal Chem* 392, 129-135.
27. Petibois C, Gouspillou G, Wehbe K, Delage JP & Deleris G (2006) Analysis of type I and IV collagens by FTIR spectroscopy and imaging for a molecular investigation of skeletal muscle connective tissue. *Anal Bioanal Chem* 386, 1961-1966.
28. Camby I, Decaestecker C, Gordower L, DeDecker R, Kacem Y, Lemmers A, Siebert HC, Bovin NV, Wesseling P, Danguy A, Salmon I, Gabius HJ & Kiss R (2001) Distinct differences in binding capacity to saccharide epitopes in supratentorial pilocytic astrocytomas, astrocytomas, anaplastic astrocytomas, and glioblastomas. *Journal of neuropathology and experimental neurology* 60, 75-84.
29. Apostolopoulos V, Barnes N, Pietersz GA & McKenzie IF (2000) Ex vivo targeting of the macrophage mannose receptor generates anti-tumor CTL responses. *Vaccine* 18, 3174-3184.
30. Regnier-Vigouroux A (2003) The mannose receptor in the brain. *International review of cytology* 226, 321-342.

Tables

Table 1. Heterogeneity levels of dendrograms done by hierarchical analyses (HA) for each sample using each band alone or combined

Sample	(1) 3020-2800	(2) 1776-1720	(3) 1712-1500	(4) 1180-950	(5) 1076-1056	(1)+(2)	(1)+(3)	(1)+(4)	(1)+(5)
S1 (n=30)	0.39	0.14	-	0.07	0.04	0.41	0.46	0.38	0.38
S2 (n=30)	0.35	0.13	-	0.04	0.02	0.38	0.41	0.35	0.35
S3 (n=30)	0.25	0.11	-	0.04	0.02	0.27	-	0.25	0.25
S4 (n=30)	0.40	0.14	0.34	0.05	0.03	0.42	0.52	0.39	0.39
S5 (n=30)	0.37	0.14	-	0.06	0.03	0.39	0.46	0.37	0.37
n=150	1.68	0.61	-	0.23	0.13	1.80	-	1.68	1.68
n=200	2.22	0.81	-	0.31	0.17	2.35	-	2.22	2.22

n=30 for each of the 5 samples (15 normal and 15 tumor BV); For all samples joined together, n=150. Then 50 spectra were added to the 150 spectra to test the classification. Five spectral interval were used for this HA, each interval alone and combination (mentioned as "+") of the first one of fatty acyl moieties with each of the other four. Spectral intervals are designated by a number: (1): 3020-2800 cm^{-1}, (2): 1776-1720 cm^{-1}, etc…

Table 2. Curve fitting results of fatty acyl chains spectral interval (3050-2800 cm^{-1}; n=100 for each set of BV).

	3012 cm^{-1} ν=(CH)	2959 cm^{-1} $\nu_{as}(CH_3)$	2921 cm^{-1} $\nu_{as}(CH_2)$	ν=(CH)/$\nu_{as}(CH_3)$	$\nu_{as}(CH_2)/\nu_{as}(CH_3)$
Normal BV (NBV)	**7.57 ± 1.41**	**17.91 ± 2.21**	**16.23 ± 1.90**	**0.43 ± 0.11**	**0.92 ± 0.13**
Tumor BV (TBV)	**8.16 ± 2.41**	**13.00 ± 2.80**	**8.33 ± 1.54**	**0.64 ± 0.17**	**0.66 ± 0.12**
TBV % NBV	**+8**	**-27**	**-49**	**+49**	**-28**

Values are designated by means ± SD. The percentage of variations between tumor blood vessels (TBV) versus normal BV (NBV) in the last line is mentioned by "+" if increase and "-" if decrease occurs.

Table 3. Ratios of asymmetric absorptions bands of the fatty acyl chains spectral interval for each tumor sample (n=40 for each sample, 20 NBV and 20 TBV)

	ν=(CH)/$\nu_{as}(CH_3)$		$\nu_{as}(CH_2)/\nu_{as}(CH_3)$		% variation (tumor/normal)	
Samples	**Normal BV**	**Tumor BV**	**Normal BV**	**Tumor BV**	ν=(CH)/$\nu_{as}(CH_3)$	$\nu_{as}(CH_2)/\nu_{as}(CH_3)$
S1	0.37	0.63	0.87	0.66	72.9	-23.5
S2	0.47	0.69	0.96	0.70	47.4	-27.6
S3	0.44	0.67	0.87	0.67	49.8	-22.9
S4	0.47	0.57	0.98	0.69	20.9	-29.0
S5	0.41	0.62	0.91	0.57	51.9	-37.5
Average	**0.43 ± 0.04**	**0.64 ± 0.05**	**0.92 ± 0.05**	**0.66 ± 0.05**	**49 ± 18.5**	**-28± 5.8**

Table 4. Curve fitting results of fatty acyl chains spectral interval with total symmetric and asymmetric absorptions bands (n=20 for each set of BV so 20% of the population).

	Asymmetric		Total (asymmetric+symmetric)	
20% of the total	ν=(CH)/$\nu_{as}(CH_3)$	$\nu_{as}(CH_2)/\nu_{as}(CH_3)$	ν=(CH)/$\nu_{as}+\nu_s(CH_3)$	$\nu_{as}+\nu_s(CH_2)/\nu_{as}+\nu_s(CH_3)$
Normal BV	**0.42 ± 0.13**	**0.87 ± 0.13**	**0.31 ± 0.09**	**0.82 ± 0.11**
Tumor BV	**0.63 ± 0.23**	**0.66 ± 0.15**	**0.45 ± 0.15**	**0.59 ± 0.13**
Tumor % normal	**51**	**-24**	**47**	**-28**

Figures legends

Figure 1

U87 pcDNA3 tumor shown in different ways: with immunohistochemistry (IHC) on slide, visible image by Spotlight, visible image after IHC on ZnSe window to locate all blood capillaries marked with CD31 (brown), FTIR image using 8 scans with a spectral resolution of 4 cm^{-1} and a spatial resolution of 6.25 µm /pixel. Scale bar represents 200 µm.

Figure 2

2A: Example of a dendrogram of a HA for one sample using the combination of the fatty acyl and carbohydrates spectral interval. N=30 where 15 are healthy blood capillaries (C) and 15 are tumor blood capillaries (T). Two clear clusters are shown separating the two populations.

2B: The same dendrogram of figure 2A when another 10 blood capillaries (marked with – for healthy and + for tumor blood capillaries) were added to test the classification. HA was performed using Ward's algorithms of OPUS 4.2 software.

Figure 3

3A: Dendrogram of the HA of all samples using the combination of the fatty acyl and carbohydrates regions. N=150 spectra where 75 are cerebral blood capillaries (.) and 75 are tumor blood capillaries (-). Two clear clusters are shown separating the two populations.

3B: The same dendrogram of figure 3A when 50 blood capillaries were added to test the classification. Totally we have 200 spectra in two clear clusters differentiating the two populations of the blood capillaries.

Figure 4

Second derivative of the average spectra of normal and tumor blood capillaries within the 3050-2800 cm^{-1} spectral interval. Minimum values at 3012, 2959, and 2921 cm^{-1} represent asymmetric bands of fatty acyl moieties.

Figure 5

Spectral curve fitting performed within the 3050-2850 cm^{-1} spectral interval. Absorption bands at 3012 cm^{-1} for ν=(CH), 2959 cm^{-1} for $\nu_{as}(CH_3)$, and 2921 cm^{-1} for $\nu_{as}(CH_2)$ were used to calculate the ν=(CH)/ $\nu_{as}(CH_3)$ and $\nu_{as}(CH_2)$/ $\nu_{as}(CH_3)$ ratios.

Figure 6

Second derivative of the average spectra of normal and tumor blood capillaries within the 1180-950 cm^{-1} spectral interval for carbohydrates determination. We can see the absence of the bands at 1068 and 1025 cm^{-1} which have been attributed to mannosyl residues.

Figure 7

Visible image of a U87 IRE1DN tumor after immunohistochemistry on ZnSe window. Crosses represent spectra chosen to test the classification method done with U87pcDNA3 sample. Arrows mark capillaries that were classified with tumor samples. The positions of those capillaries, shown precisely inside the tumor or around it, delimit very well the tumor area. Scale bar represents 100 µm.

Figure 8

Second derivative spectra of endothelial cells lysates spectra in the 1200-950 cm^{-1} region. The band at 1068 cm^{-1} was observed in HCMEC and not in HUVEC average spectrum.

Figure 1

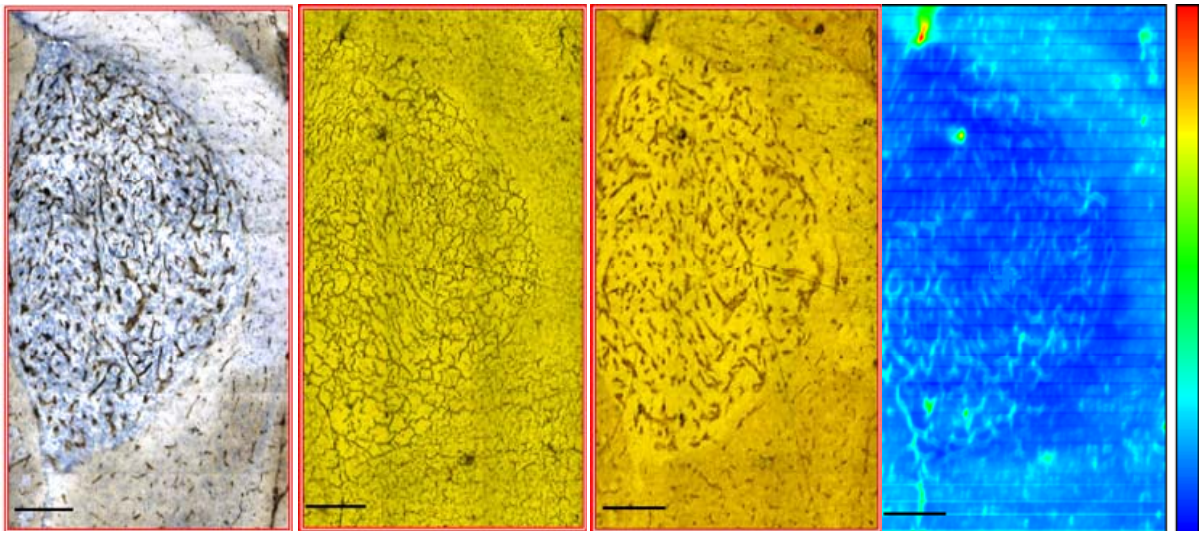

Figure 2.A

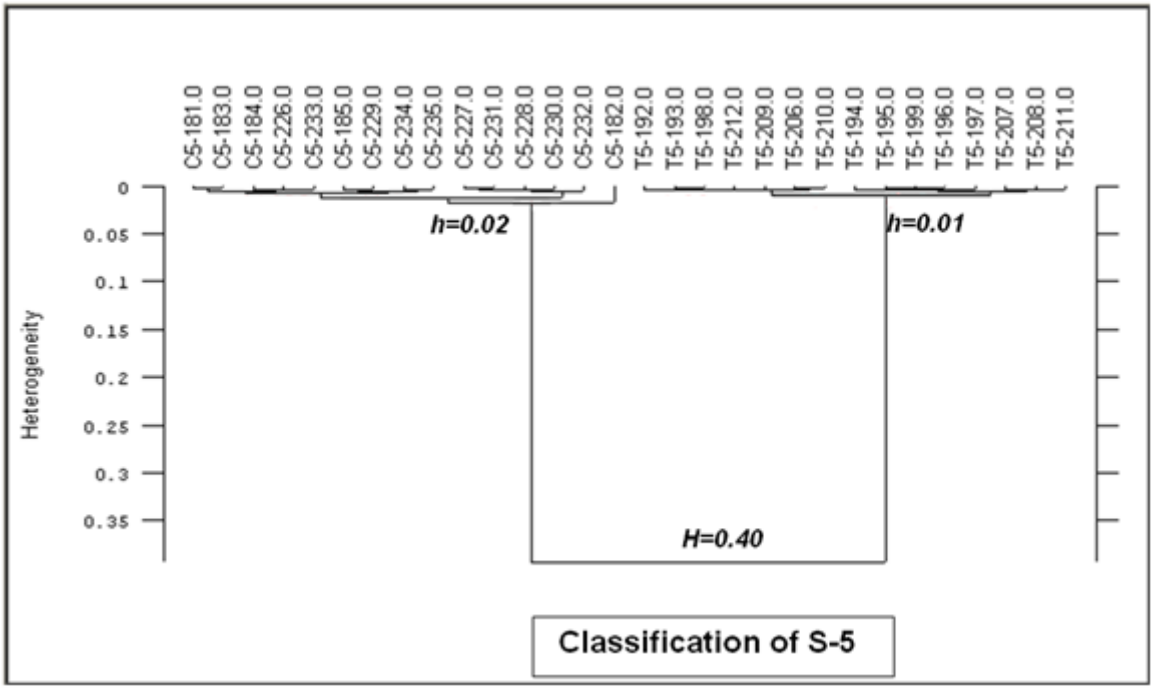

Figure 2.B

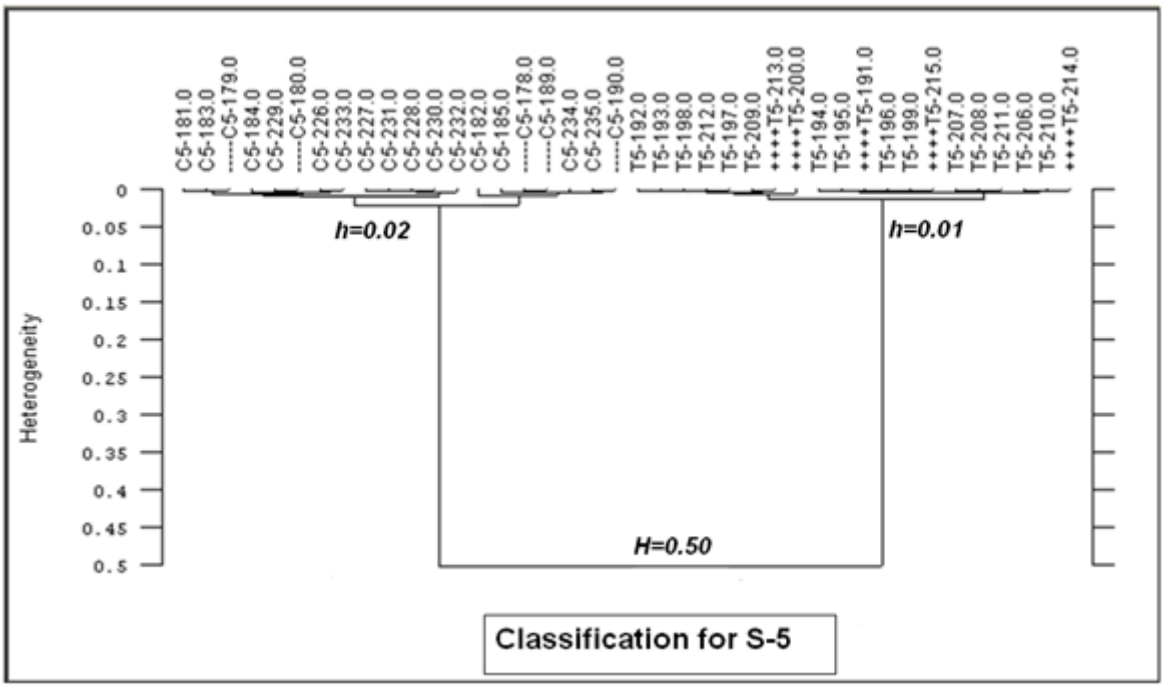

Figure 3.A

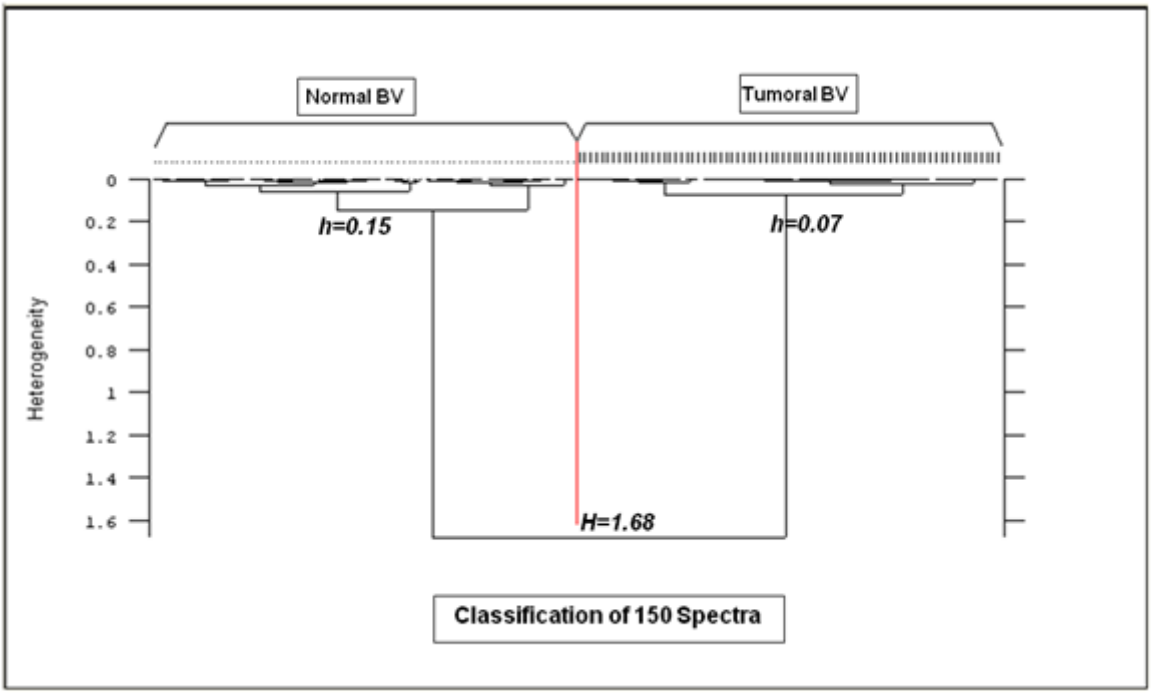

Figure 3.B

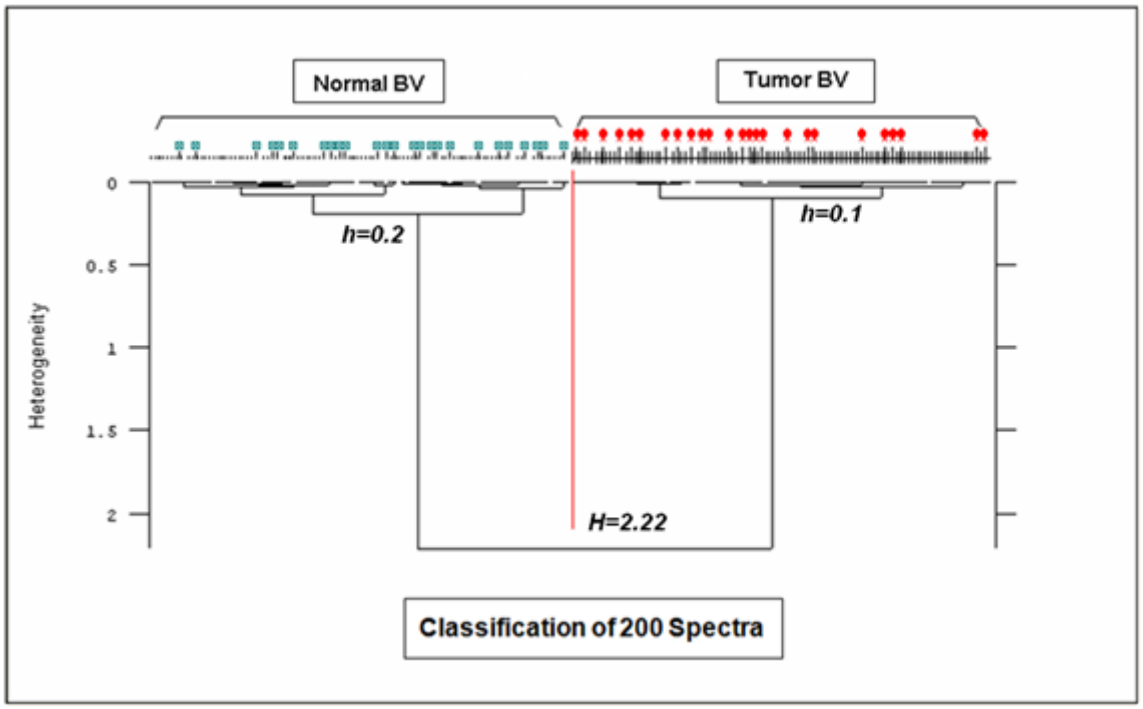

Figure 4

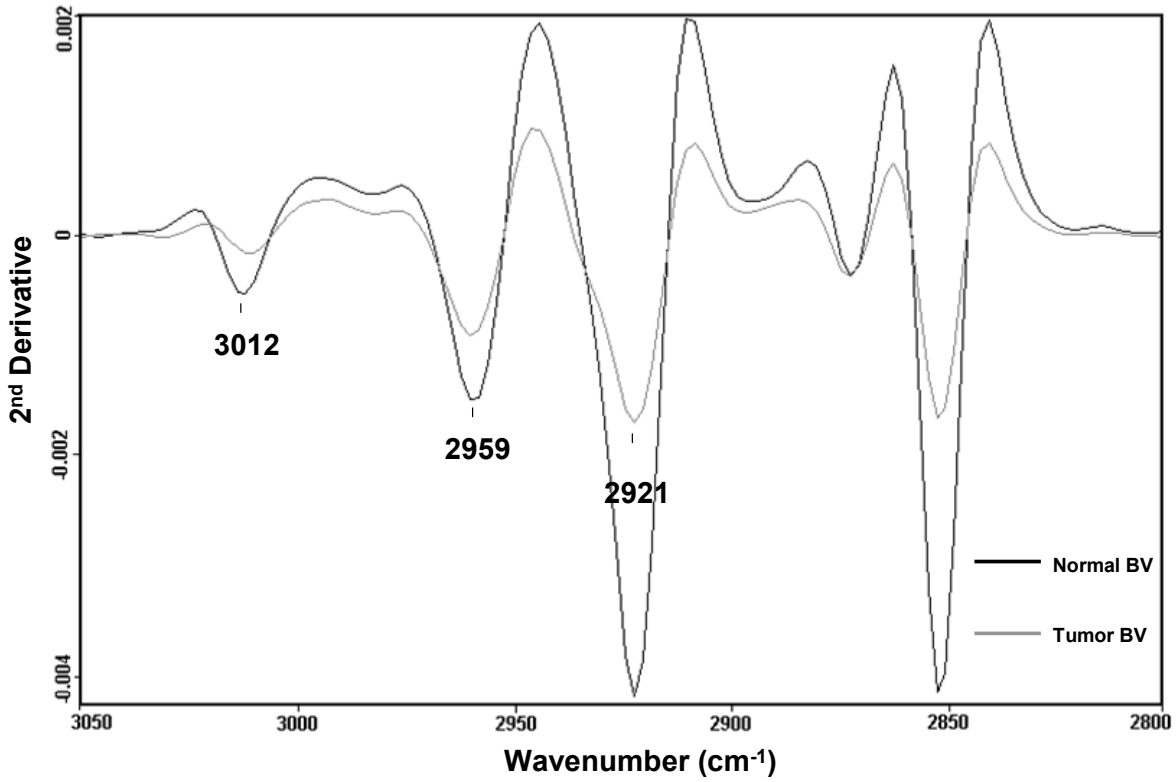

Figure 5

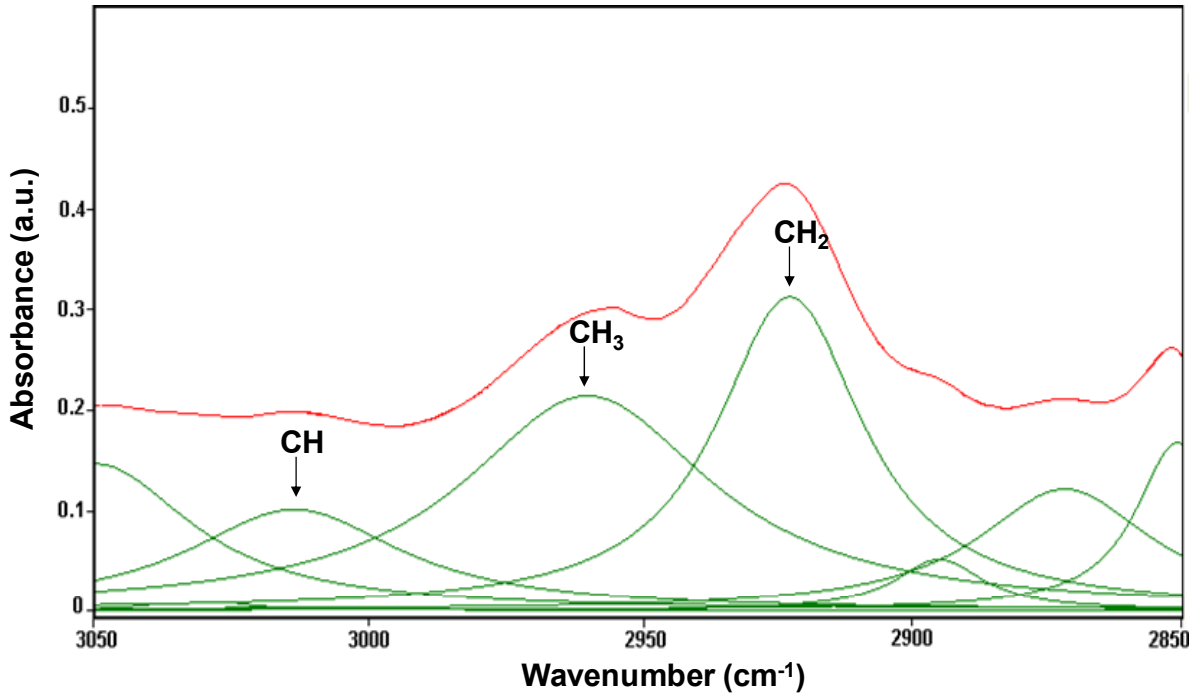

Figure 6

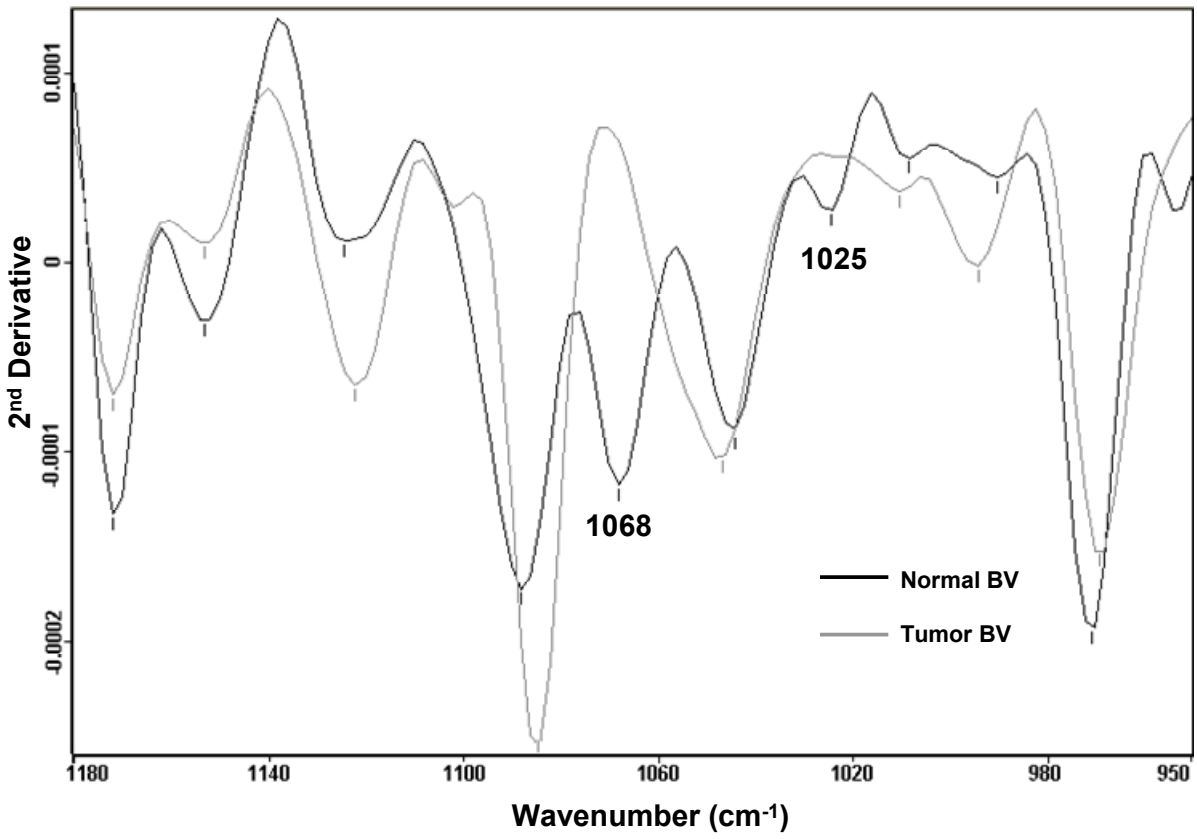
0.0001
0
-0.0001
-0.0002
2nd Derivative
1180
1140
1100
1060
1020
980
950
Wavenumber (cm-1)
1025
1068
Normal BV
Tumor BV

Figure 7

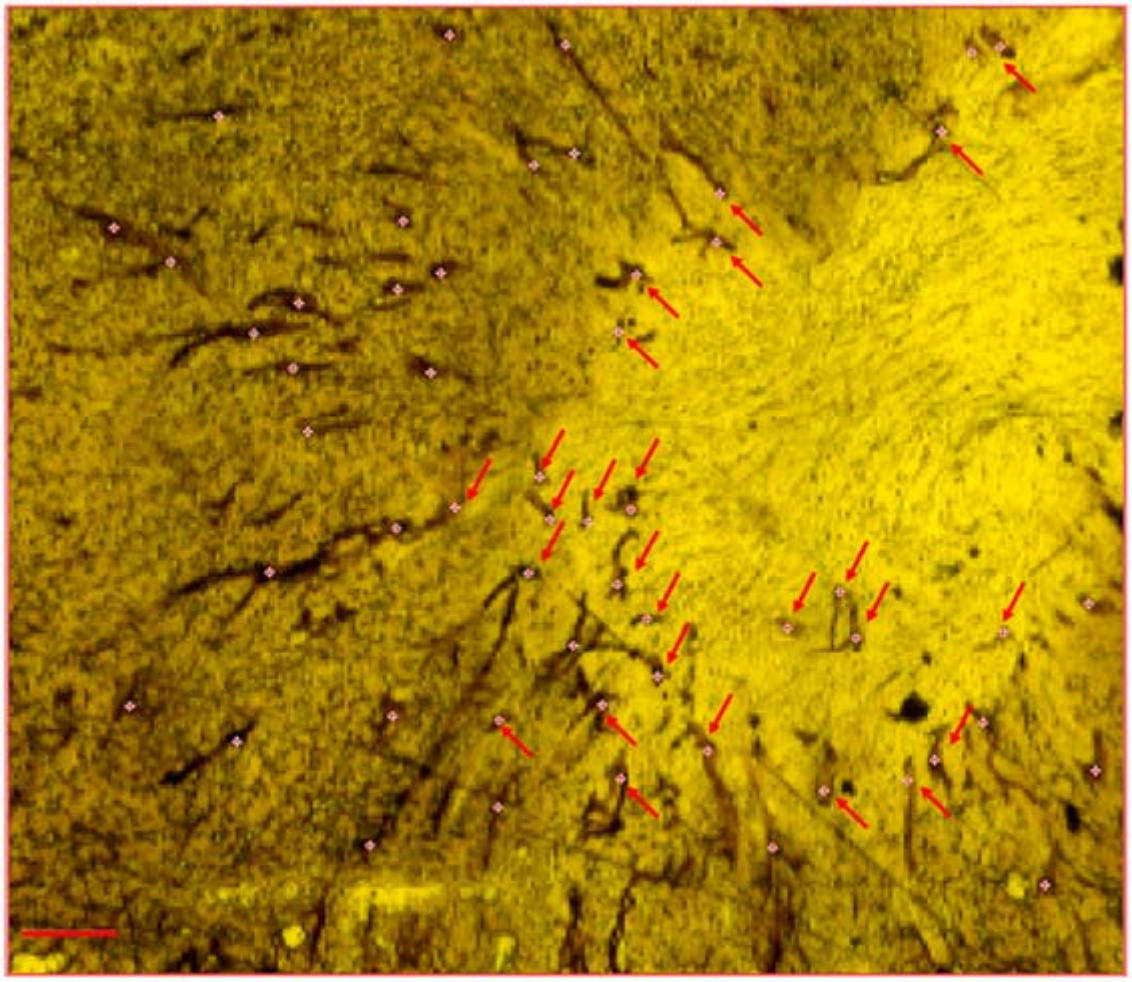

Figure 8

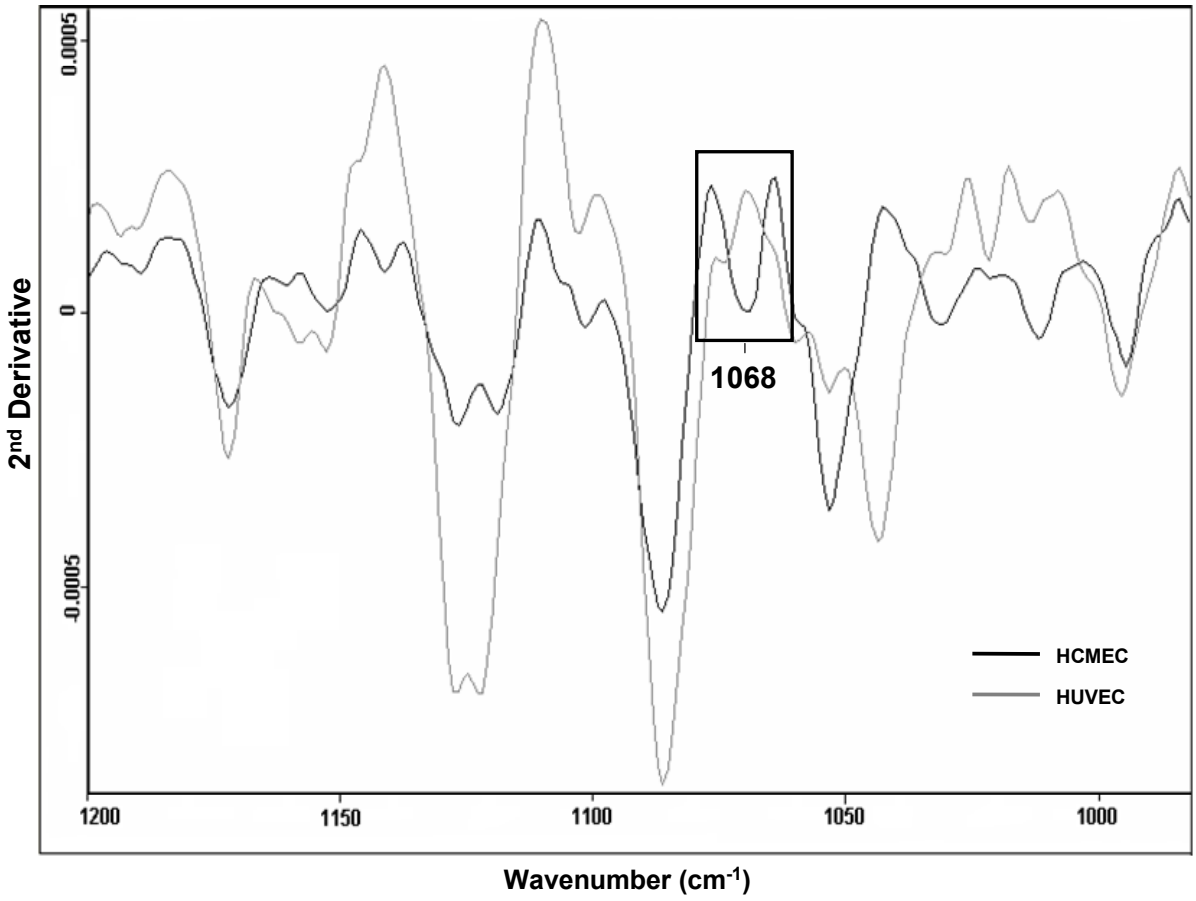
0.0005
0
-0.0005
2nd Derivative
1068
HCMEC
HUVEC
1200
1150
1100
1050
1000
Wavenumber (cm-1)

Research Report

- RESEARCH REPORT -

Application of FTIR spectral imaging to study alterations of blood vessels in human glioma

---

Purpose: The aim of the present work was to use FTIR spectral imaging to study biochemical changes in blood vessels from tissue sections of human glioma with different grades. Brain tumor specimens were obtained by the Service of Anatomopathology from patients undergoing neurosurgery. We applied the data treatment methods developed in previous studies (research report and papers) to test their transferability form animal models to human tissues.

Main results: Secondary structure of proteins was determined by using the curve-fitting of the amide I spectral interval (1700-1600 cm^{-1}). Changes in protein secondary structure of blood vessels could be identified between blood capillary spectra of healthy and tumor areas, with a decrease in triple helix content (~ 9 % decrease; $P < 0.01$) observed for tumor BV. This change in protein secondary structure was likely to be due to the abnormal arrangement (crosslinks) of collagen fibers in the vascular basement membrane during tumor growth. Moreover, hierarchical analysis of BV spectra based on two combined regions of fatty acyl (3020-2800 cm^{-1}) and carbohydrates (1200-900 cm^{-1}) formed two clusters discriminating normal and tumor BV with a small percentage of misclassification (5 and 18.2 %, respectively). Our study demonstrated that FTIR spectra of BV may reveal discriminant spectral markers to distinguish between healthy and tumor areas of brain tissues and thus may define the tumor limits. However, no correlation could be found between FTIR classification and pathological grading of grade III and IV tumors, i.e., no classification model could discriminate between grade III and IV sample FTIR spectra. This might be attributed to the high morphological heterogeneity usually observed in grade III and IV gliomas, thus potentially leading to misclassifications in pathological examinations.

In conclusion, FTIR imaging allowed establishing different molecular markers in the proteins, lipids, and carbohydrates spectral intervals to differentiate between tumor and normal blood vessels in human brain tissues. These markers should be developed and validated in further work by using a larger collection of human samples in order to help neurosurgeons to define tumor margins during glioma surgery. Nevertheless, the results obtained in this study indicate that FTIR imaging allows discriminating healthy and pathological features for discriminating tissue areas. Therefore, this work opens the way to a functional FTIR imaging for the development of a molecular anatomopathology of brain tumors.

Application of FTIR spectral imaging to study alterations of blood vessels in human glioma

Abstract

Distinction between tumor and normal brain blood vessels (BV) may be particularly important in neurosurgery to maximally resect tumor margins without affecting brain function. In the present work we used FTIR spectral imaging to study biochemical changes in blood vessels in human glioma sections of different grades. FTIR imaging was able to detect changes in protein secondary structure of blood vessels from healthy and tumor areas, a decrease in triple helix content (~ 9 % decrease; $P < 0.01$) was observed for tumor BV. Moreover, hierarchical analysis of BV spectra based on two combined regions of fatty acyl (3020-2800 cm^{-1}) and carbohydrates (1200-900 cm^{-1}) gives two clusters corresponding one to normal BV and the other to tumor BV with a little percentage of misclassification. The results outlined a lower level of lipids and saccharidic residues for tumor BV. Our study shows that FTIR spectra of BV contain discriminant markers to distinguish healthy and tumor areas of brain tissues and thus may define the tumor limits.

Abbreviations

BV: blood vessels; FTIR: Fourier Transform Infrared; GBM: glioblastoma multiforme; IHC: Immunohistochemistry; MPV: microvascular proliferation; VBM: Vascular basement membrane

Keywords

FTIR spectral imaging, gliomas, angiogenesis, blood vessels

Materials and methods

Tissue samples

Brain tumor specimens were obtained from 29 patients undergoing neurosurgery in the period going from November 2005 to October 2007. All specimens were provided from Bordeaux Hospital Center (CHU Pellegrin; Bordeaux) through the collaboration of the Department of Anatomy and Cytological Pathology. Samples were divided as follow: 1 specimen grade I, 1 astrocytoma grade II, 4 astrocytomas grade III, 17 glioblastomas grade IV, and 6 metastasis. Fresh samples were frozen in liquid nitrogen immediately after tumor resection without fixatives to perform cryosectioning. For each sample, a 10 µm tissue section was transferred onto a glass slide for immunohistochemistry assessment to be stained with CD34 (1:50 dilution, Immunotech, France). This antibody recognizes a cell surface antigen expressed on human vascular endothelium. A 20 µm following section was deposited onto an IR transparent silicon window for FTIR imaging in transmission mode. All tissue sections were dried on air before further processing. Pathological diagnosis was also obtained from experienced pathologists' observations of additional formalin-fixed and paraffin-embedded tissue sections using standard histological H&E staining.

Spectral data acquisition and processing

FTIR spectral imaging data were acquired in transmission mode using a Spotlight 300 FTIR imaging system, equipped with a Spectrum One spectrometer (Perkin-Elmer, France). The imaging system was equipped with a liquid nitrogen cooled Mercury Cadmium Telluride (MCT) linear detector of 16 pixel elements. FTIR images were collected from samples in the mid IR range (4000-720 cm^{-1}) using a spectral resolution of 4 cm^{-1} accumulating 8 scans for each data point. The spatial resolution used was 6.25 µm for each pixel. Regions of interest in the tissue sections were selected referring to the immunohistochemical and histological sections on slides to locate blood vessels. All data acquisition, post-processing (atmospheric and baseline corrections), and image construction were performed using sub-routines of the Spotlight 1.0 (Perkin Elmer, France). Then all data were analysed using OPUS 4.2 software (Bruker, Germany).

Spectral data analysis and treatments

For every FTIR image of a blood vessel, the FTIR spectra corresponding to the pixels covering the basal membrane were averaged and saved for further data treatment. A model spectrum for curve fitting procedure (previously described in [1]) was applied to each blood vessel averaged spectrum, for the determination of protein secondary structure changes between samples. Absorption bands within the 1750-1480 cm^{-1} spectral interval were localized from second derivative spectra with a 9-point smoothing (subroutine of OPUS 4.2 software, Bruker). This spectral interval shows the two major absorbance bands of proteins (1655 and 1545 cm^{-1} for amide I and II absorptions, respectively) and may be used to determine the secondary structure of proteins. Protein secondary structure parameters were assessed using absorption bands assigned as α-helix (centered at 1655 cm^{-1}), triple helix (centered at 1638 cm^{-1}), β-sheets (1690 and 1628 cm^{-1} to parallel β-sheets, and 1680 cm^{-1} to anti-parallel β-sheets), β-turns (1666 and 1615 cm^{-1}), and unordered structure (at 1645 cm^{-1}). Each band was calculated as a percentage of the total amide I absorption as we previously described [1, 2].

Moreover, spectra were subjected to hierarchical analysis (HA) using Ward's algorithms of OPUS 4.2 software (Bruker, Germany). In this analysis, data points from spectra were compared based on the Euclidean distances between them. These distances allowed the classification of all spectra within clusters creating a dendrogram giving a heterogeneity level between the two populations. As we demonstrated in a previous work that HA was able to differentiate between normal and tumor blood vessels using the fatty acyl and carbohydrate regions, we tried to apply this method on those human samples. HA was performed on the first derivatives of the spectra with 5-point smoothing of different blood vessels from normal areas and grade III and IV tumor areas.

Statistics

Data of protein secondary structure parameters were used for comparisons between grades. All data were expressed as mean ± SD. A paired Student's *t*-test was used to determine differences between series of data between groups. *P-values* were fixed at 0.01 and 0.05 to consider the significance level of differences.

Results and Discussion

Secondary structure of protein contents

After choosing blood vessels in visible images referring to the immunohistochemical section, ***(Figure 1)*** FTIR spectra corresponding to the pixels covering the basal membrane were averaged and one averaged spectrum was taken for each blood vessel. Using the whole set of blood vessels, 48, 125, and 73 blood vessels were analyzed for grade III, grade IV and metastasis sections groups, respectively. We exclude samples of Grade I and II since there was an insufficient number for the study. Secondary structure parameters obtained from the curve fitting procedure of the amide I region ***(Figure 2)*** were compared between each 2 of 3 groups ***(see Table 1 for more information)***. Comparison between all blood vessel spectra of grade III and grade IV tumor sections showed a significant decrease in α-helix and increase in unordered structure in grade IV with respect to grade III. No significant differences were shown between grade III and metastasis or between grade IV and metastasis. These results may not be very informative because all blood vessels were taken together mixed between normal and tumor for the different grades.

In other term, we divided blood vessels in tumor and normal groups according to the diagnosis made by the pathologists when identifying tumor and healthy regions in tissue sections. For these statistics we only took into consideration samples where these regions were clearly identified in the two consecutive sections of IHC and IR to be more accurate in choosing blood vessels. For tumor blood vessels, we add spectra from grade III and grade IV samples together (n=66) to differentiate their protein secondary structure with normal blood vessels from healthy regions (n=40). Results showed that only significant difference ($P < 0.01$) could be found in triple helix secondary structure, it decreases in tumor BV with respect to normal BV (14.5 ± 2.31 % vs. 13.2 ± 2.24 %; $P < 0.01$; ~ 9 % decrease) ***(Table 2).*** These results on human samples agreed well with our previous work obtained on animal model [1]. We have already described this change as a molecular marker that may be due to the conformational changes of collagen fibers in the vascular basement membrane (VBM) during tumor growth; since the collagen (especially collagen IV) is a main component of the VBM and it is mainly constituted of triple helix.

Moreover, when we divided the tumor blood vessel group to compare the protein secondary structure between grade III and grade IV, we found significant differences in α-helix and β-sheets amounts. There was a decrease in the percentage of α-helix in grade IV with respect to grade III (30.7 ± 2.43 vs. 27.1 ± 3.46 %; $P < 0.01$). Inversely, there was an increase in the percentage of β-sheets in grade IV with respect to grade III (18.6 ± 2.36 % vs. 21.5 ± 2.70; $P < 0.01$) ***(Table 3).*** Here again, we couldn't be certain of this deviation since we haven't sufficient number of data for interpretation.

Hierarchical analysis

HA was used for data analysis to classify normal and tumor blood vessels using the first derivatives of the spectra with 5-point smoothing. We used the two spectral regions of fatty acyl chains (3020-2800 cm^{-1}) and carbohydrates (1180-950 cm^{-1}) in order to get a better discrimination between the two sets of data. In a first time, we made a classification between normal (15 BV spectra from one sample) and tumor (18 BV spectra from one sample of glioblastoma G IV) based on these two spectral regions. As we can see in ***Figure 3,*** the two sets of data were correctly classified without any overlapping. After collecting all data we tried the same IR based classification to see the robustness of the method if we increase the number of samples. As total data we had 40 spectra of normal blood vessels (issued from different samples in healthy regions identified by histological observations) and 66 spectra of tumor blood vessels (from grade III and IV samples). We obtained two clusters with a misclassification of a few spectra ***(Figure 4).*** Only 5 % of normal BV spectra were misclassified with tumor and 18.2 % of tumor BV spectra misclassified with normal.

We should also note that a comparison between grade III and grade IV samples show an apparent disagreement between the IR-predicted classification and the histopathological grade (results not shown). This could be attributed to the high heterogeneity within glioblastoma multiforme of grade IV. Although the IR based classification was not entirely consistent with conventional histopathology in grading the tumors of grade III and IV, the IR based classification shows no great confusion between tumor and normal blood vessels even with a little percentage of

misclassification. This may be due to the invasiveness of gliomas into the surrounding tissue, where on these limits we can confuse between normal and tumor; hence the idea to search for molecular markers able to differentiate between normal and tumor blood vessels in these areas to help neurosurgeons for defining the tumor margins.

Second derivatives comparison

Moreover, a careful examination of second derivative of the averaged spectra of normal, grade III and grade IV samples indicates that most of the variability is in the regions of fatty acyl and carbohydrates (3050–2800 and 1200–950 cm^{-1} respectively) ***(Figures 5 and 6).*** Concerning the fatty acyl chain regions, there is a clear difference in peaks on 3012 cm^{-1}, 2959 cm^{-1} and 2921 cm^{-1} corresponding respectively to the asymmetric stretching vibrations of ν=(CH), $\nu_{as}(CH_3)$ and $\nu_{as}(CH_2)$. These peaks are of smaller intensities in tumor BV spectra than in normal. The absorptions in question arise from the lipid constituents (e.g., phospholipids and possibly others). The observed trend is in accordance with studies suggesting that an increase in malignancy is accompanied by a reduction of total lipids and that normal tissue contains more components of long-chain C-H and C=O bonds that decrease and even disappear in the spectra of malignant tissues. This difference may be interpreted by the fact that fat in the region of malignant tissue is consumed because of the necessary nutritional and energy requirement in the development of carcinoma (because triglyceride contains a large proportion of methyl, methylene and carbonyl).

A second prominent spectral trend is the difference in certain absorptions in the 1200–950 cm^{-1} region. Figure 6 shows the second derivative of the average spectra of the three tissue classes (normal, tumor of grade III and grade IV). In this region occur absorption bands due to sugar moieties as well as to deoxyribose C–O and PO^{2-} groups of DNA. We can obviously see the difference between the averaged spectra especially in the region of 1050–1085 cm^{-1}. Moreover, we, in the previous work, found a discriminating band in the carbohydrates region at 1068 cm^{-1} present in normal murine BV and absent in tumor BV. This band was also present in spectra of endothelial cells of human cerebral origin. Here again in this study this absorption band is present only in normal BV although shifted to 1072 cm^{-1}.

References

1. Wehbe K, Pinneau R, Moenner M, Deleris G & Petibois C (2008) FTIR spectral imaging of blood vessels reveals protein secondary structure deviations induced by tumor growth. *Anal Bioanal Chem* **392**, 129-135.
2. Petibois C, Gouspillou G, Wehbe K, Delage JP & Deleris G (2006) Analysis of type I and IV collagens by FTIR spectroscopy and imaging for a molecular investigation of skeletal muscle connective tissue. *Anal Bioanal Chem* **386**, 1961-1966.

Tables

Table 1: Secondary structure determination of VBM protein contents for all blood vessels (BV) of Grade III, Grade IV and metastasis sections

	α helix	β sheets	β turns	Unord. Struc	Triple helix
Grade III (G III)	**28.7 ± 5.95**	**20.1 ± 4.78**	**28.9 ± 5.43**	**8.7± 4.20**	**13.6 ± 4.25**
Grade IV (G IV)	**26.9 ± 4.40**	**21.3 ± 3.64**	**27.7 ± 3.50**	**10.0 ± 3.03**	**13.9 ± 2.73**
Metastasis (M)	**27.1 ± 5.44**	**21.1 ± 3.69**	**27.8 ± 3.39**	**10.0 ± 3.52**	**14.0 ± 2.32**
***t* test G III vs. IV**	**0.032 ***	**0.066**	**0.115**	**0.025 ***	**0.564**
***t* test G III vs. M**	**0.137**	**0.172**	**0.177**	**0.076**	**0.578**
***t* test G IV vs. M**	**0.745**	**0.712**	**0.963**	**0.927**	**0.966**

* P<0.05: Significant difference between groups. n = 48, 125 and 73 BV spectra for Grade III (G III), Grade IV (G IV) and metastasis (M) sections, respectively. Absorption bands used for proteins secondary structure determination: α-helix (1655 cm^{-1}), β-sheets (1690, 1680, and 1628 cm^{-1}), β-turns (1666 and 1615 cm^{-1}), unordered structure (1645 cm^{-1}), and triple helix (1638 cm^{-1})

Table 2: Secondary structure determination of VBM protein contents for normal and tumor blood vessels (BV) of Grade III and IV together

	α helix	β sheets	β turns	Unord. Struc	Triple helix
Normal BV	**25.6 ± 6.45**	**21.2 ± 4.85**	**28.2 ± 3.88**	**10.5 ± 4.00**	**14.5 ± 2.31**
Tumor BV G III + G IV	**27.5 ± 3.54**	**21.2 ± 2.81**	**28.7 ± 3.15**	**9.4 ± 2.31**	**13.2 ± 2.24**
***t* test Tumor BV vs. Normal BV**	**0.051**	**0.982**	**0.460**	**0.066**	**0.005 ****

** P<0.01: Significant difference between groups. n = 40 and 66 spectra for normal and tumor BV, respectively.

Table 3: Secondary structure determination of VBM protein contents for Grade III and Grade IV blood vessels

	α helix	β sheets	β turns	Unord. Struc	Triple helix
Grade III BV	**30.7 ± 2.43**	**18.6 ± 2.36**	**29.6 ± 2.87**	**8.7 ± 2.86**	**12.4 ± 1.62**
Grade IV BV	**27.1 ± 3.46**	**21.5 ± 2.70**	**28.6 ± 3.20**	**9.5 ± 2.23**	**13.3 ± 2.30**
***t* test Grade IV vs. Grade III**	**0.006 ****	**0.006 ****	**0.410**	**0.343**	**0.302**

** P<0.01: Significant difference between groups. n = 8 and 58 spectra for Grade III and Grade IV blood vessels, respectively.

Figures Legends

Figure 1: A: optical image of immunohistochemistry section (10 µm) where blood vessels were marked with CD34 (brown). **B:** visible image of the consecutive tumor section (20 µm) deposited on silicon window where corresponding blood vessels are shown. **C:** full spectral image of blood vessels done with a spatial resolution of 6.25 µm corresponding to the size of a pixel. Scale bar represents 100 µm.

Figure 2: Spectral curve fitting for the 1750-1500 cm^{-1} spectral interval. Absorption bands of amide I are used for the protein secondary structure determination: α-helix (at 1655 cm^{-1}), β-sheets (1690, 1680, and 1628 cm^{-1}), β-turns (1666 and 1615 cm^{-1}), unordered structure (1645 cm^{-1}), and triple helix (1638 cm^{-1}).

Figure 3: Classification between normal (15 BV spectra from one sample) and tumor (18 BV spectra of G IV from one sample) based on fatty acyl (3020-2800 cm^{-1}) and carbohydrates (1200-900 cm^{-1}) spectral regions.

Figure 4: Classification between normal (40 spectra) and tumor (66 spectra from G IV and G III) blood vessels based on fatty acyl (3020-2800 cm^{-1}) and carbohydrates (1200-900 cm^{-1}) spectral regions. The percentage of normal BV spectra misclassified with tumor is 5 %, and the percentage of tumor BV spectra misclassified with normal is 18.2 %.

Figure 5: Second derivative spectra of normal, grade III and grade IV averaged blood vessel (used for the classification in figure 4) within the 3050-2800 cm^{-1} spectral interval. Absorption bands at 3012 cm^{-1}, 2959 cm^{-1} and 2921 cm^{-1} correspond to the stretching vibrations of ν=(CH), $\nu_{as}(CH_3)$ and $\nu_{as}(CH_2)$, respectively.

Figure 6: Second derivative spectra of normal, grade III and grade IV averaged blood vessel within the 1200-950 cm^{-1} spectral interval for carbohydrates determination. As we can see, the absorption band at 1072 cm^{-1} is present only in normal BV.

Figure 1

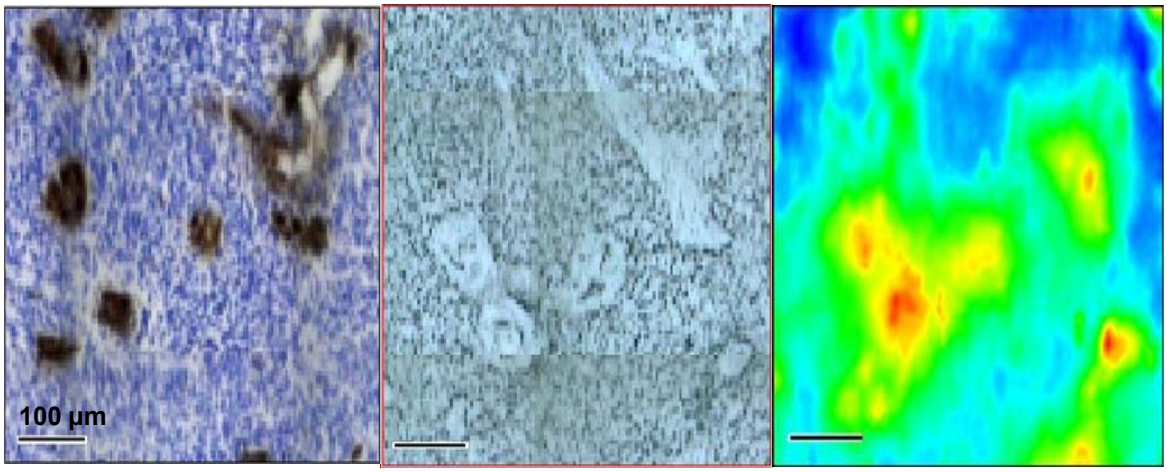

A: IHC (CD34) B: Visible (Si) C: IR (6.25 µm)

Figure 2

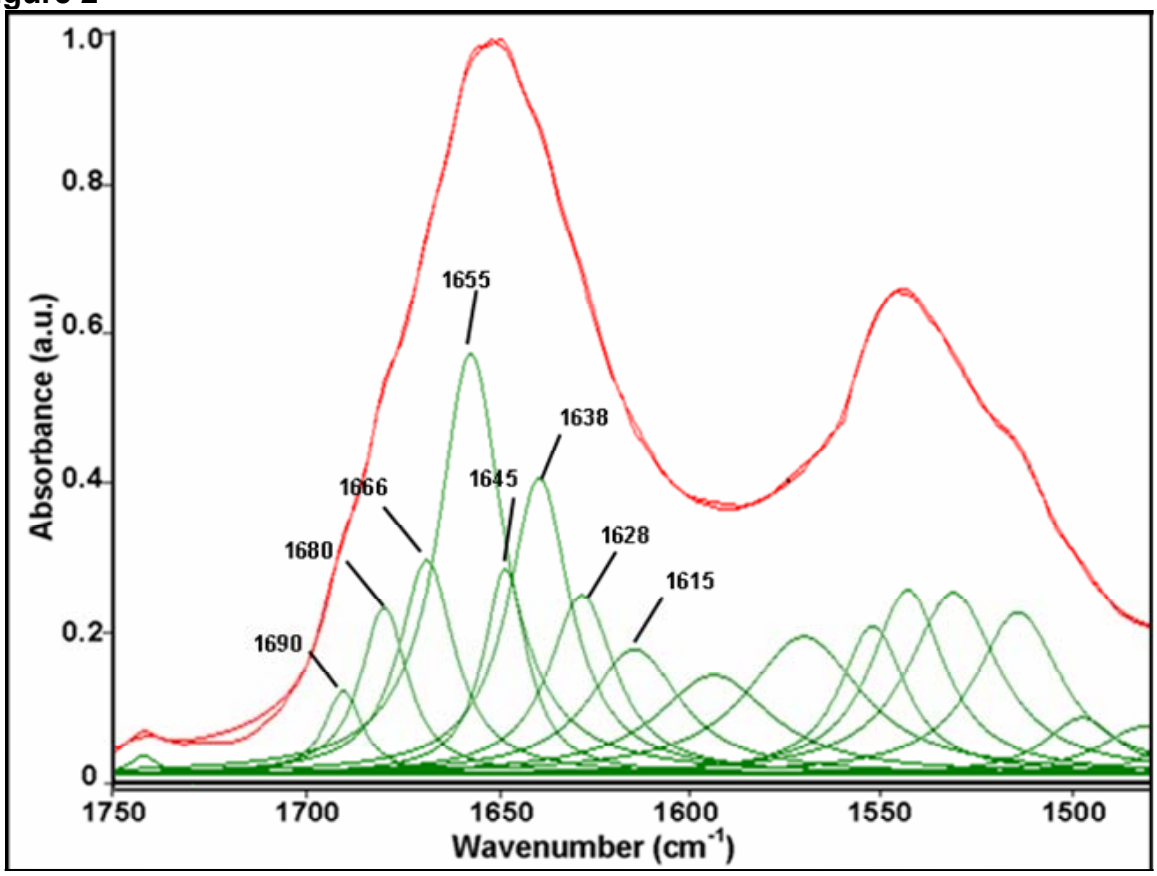

Figure 3

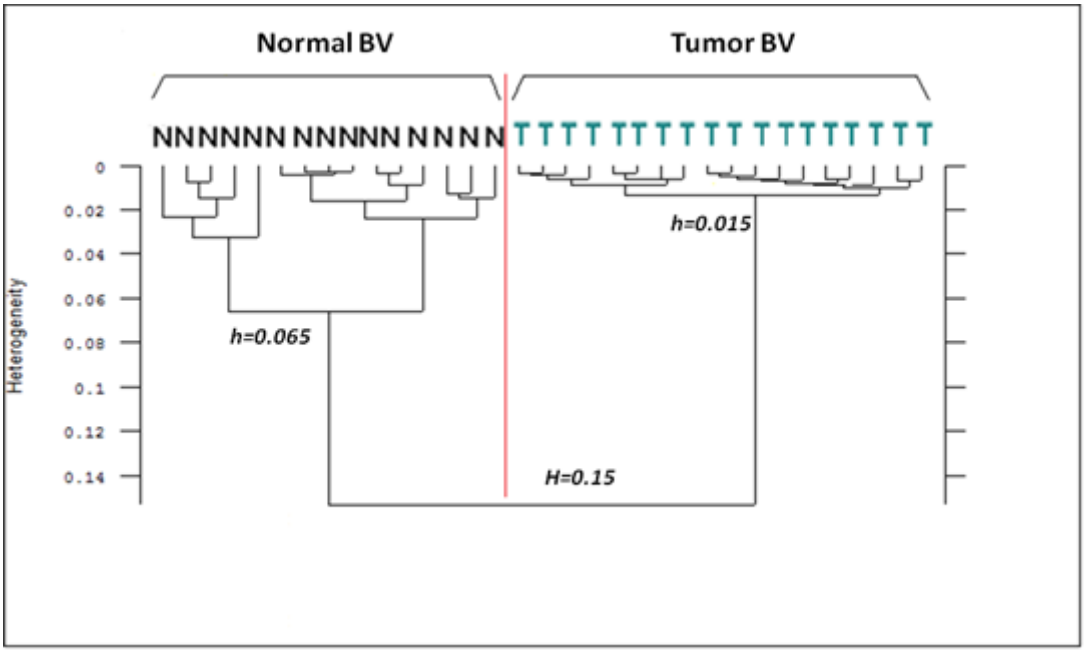

Figure 4

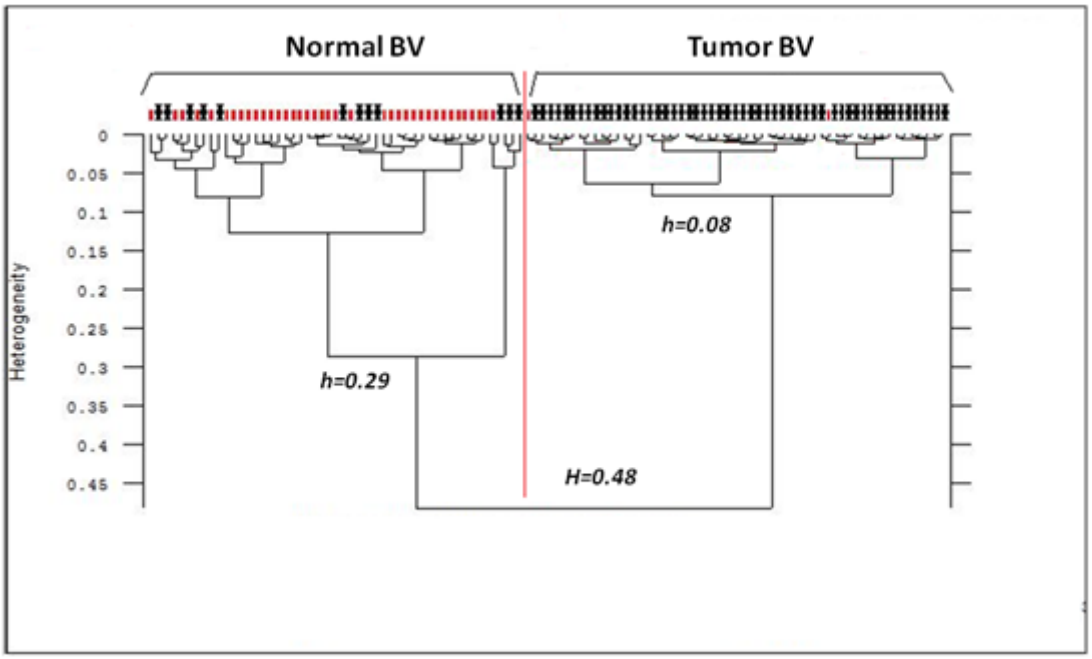

Figure 5

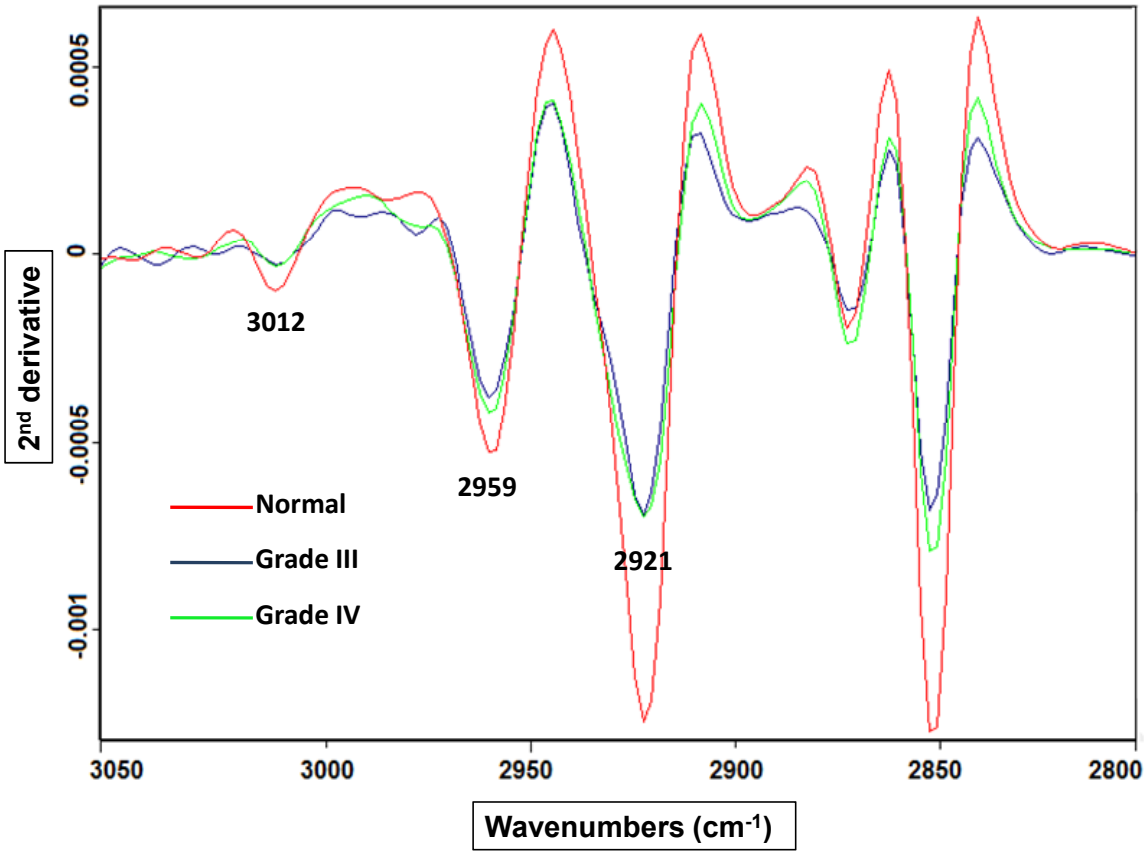

Figure 6

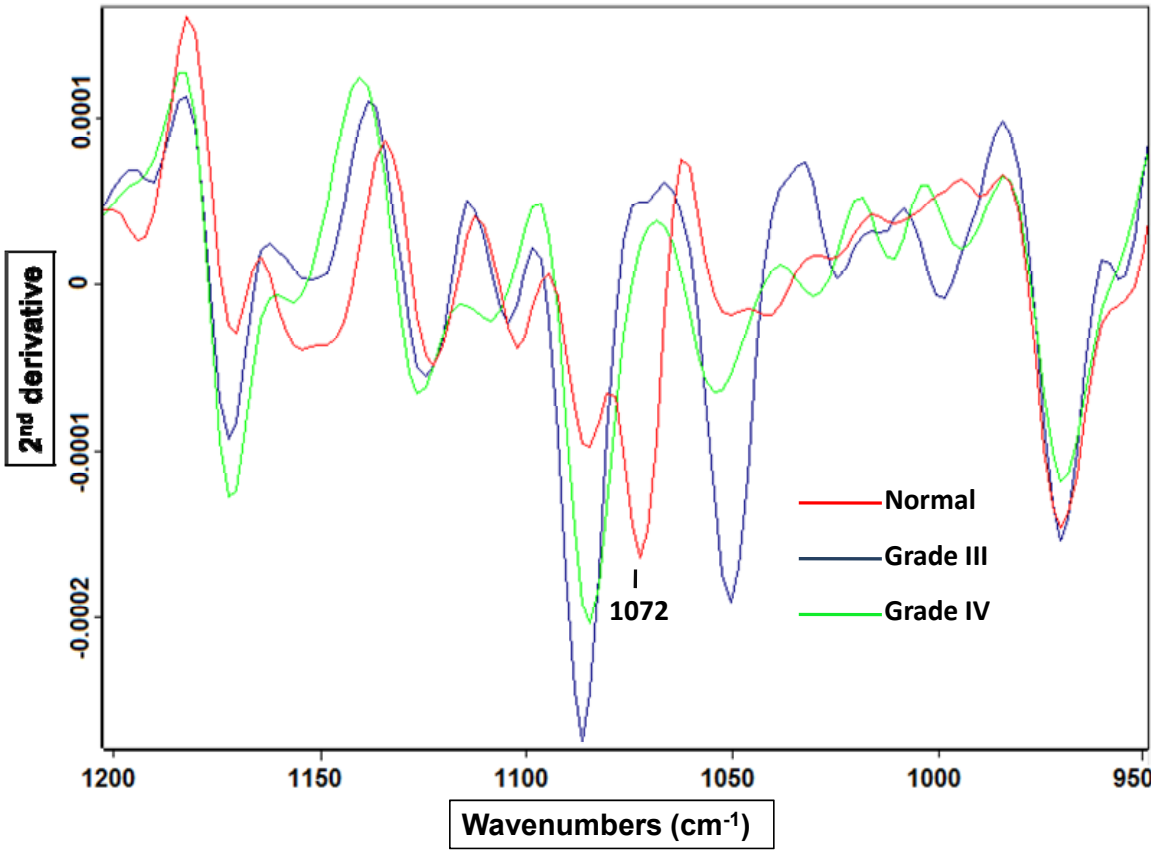


Conclusion
&
Perspectives

Dans ce travail nous avons exploré une nouvelle méthodologie pour étudier les vaisseaux sanguins angiogéniques des tumeurs cérébrales (en particulier des gliomes). Ces tumeurs richement vascularisées et agressives s'infiltrent dans le parenchyme cérébral sain, ce qui rend difficile l'exérèse complète de la tumeur malgré les outils de diagnostic actuels. Cette méthodologie a été fondée sur l'imagerie fonctionnelle infrarouge à transformée de Fourier (IRTF). L'utilisation de cette spectro-imagerie vibrationnelle peut trouver un intérêt dans de nombreuses pathologies tel que le cancer et plus particulièrement les gliomes. En tenant compte du rôle de l'angiogenèse dans les gliomes, des limites des techniques actuelles d'imagerie, et des informations moléculaires disponibles par le biais de l'IRTF, nous avons effectué cette recherche pour apporter une comparaison moléculaire aux techniques histologiques utilisées pour le diagnostic des gliomes.

La comparaison de cette technique avec les modalités d'imagerie de routine met en évidence de nombreux avantages : (i) c'est une technique caractérisée par sa haute résolution spatiale (~6 µm) ce qui en fait une modalité d'imagerie *ex vivo* très performante, (ii) elle est rapide vis-à-vis de l'acquisition des données spectrales qui peuvent être collectées et interprétées en quelques minutes ; (iii) elle exige un minimum de préparation des échantillons, vu sa capacité en tant que spectroscopie vibrationnelle d'identifier la composition chimique des tissus sans l'utilisation de marqueurs ; et (iiii) elle est non destructive, de sorte que l'échantillon puisse être soumis à d'autres analyses telle que l'immunohistochimie dans le but de confirmer les conclusions. De plus tous les moyens actuels d'identification moléculaire de l'angiogenèse sont laborieux en comparaison avec la spectro-imagerie infrarouge qui présente à la fois un gain du temps et d'argent.

La plupart des paramètres pertinents qui ont été mis en évidence lors de cette étude sont les suivants:

- La détermination des altérations de la structure secondaire des protéines des vaisseaux sanguins au cours de la croissance de la tumeur. Ces protéines contenues dans la membrane vasculaire (tel le collagène) ont été modifiées au cours de la progression tumorale lors du stress angiogénique. La modification au niveau de la

triple hélice, par exemple, pourrait être utilisée comme un marqueur moléculaire de la gradation tumorale.

- L'évaluation des modifications des phospholipides membranaires dans les vaisseaux sanguins. Ceci a été traduit par un niveau plus haut d'insaturation des chaînes d'acides gras dans les vaisseaux tumoraux et plus particulièrement dans les tumeurs plus agressives.

- La discrimination rigoureuse entre une vasculature saine et tumorale. Celle ci a été basée sur une méthode efficace de classification (algorithme de Ward) qui a permis de différencier les capillaires sanguins cérébraux de souris des capillaires angiogéniques de la tumeur après une implantation intracrânienne de cellules tumorales de gliomes. Cette classification fondée sur les contenus moléculaires du tissu, notamment glucidiques et lipidiques, a permis de bien délimiter la zone tumorale dans un autre phénotype invasif imitant l'infiltration des gliomes humains dans le tissu sain.

Une combinaison de ces paramètres a été mise à profit pour assurer une histopathologie moléculaire solide pour l'étude angiogénique des gliomes dans des tumeurs de xénogreffe. Par conséquent, nous avons ensuite utilisé ces marqueurs moléculaires sur des échantillons de gliomes humains afin de valider leur application. En prenant un seul grade de tumeur, les vaisseaux ont été parfaitement classés; par contre en prenant un nombre d'échantillons plus grand avec deux grades différents, il y a eu un faible pourcentage d'erreur de classification (mais inférieur à celui de l'histopathologie). Ceci est probablement dû à la forte hétérogénéité des gliomes ou au problème de reproductibilité de la classification anatomopathologique de l'OMS. Malgré ce faible pourcentage d'erreur, les résultats ont démontré la faisabilité de différencier la vasculature tumorale de la vasculature saine sur ces gliomes humains. Ce qui pourrait être utilisable pour délimiter la zone tumorale vis-à-vis de la zone saine lors d'une intervention chirurgicale. Les résultats ouvrent alors la voie à l'élaboration d'une histopathologie moléculaire, qui pourrait devenir un outil analytique rapide, fiable et utile pour les neurochirurgiens avec une durée compatible avec la chirurgie.

Nous avons ainsi montré que la spectro-imagerie IRTF est une technique prometteuse qui pourrait servir comme un outil clinique de diagnostic des gliomes afin de compléter les méthodes existantes. En raison de son potentiel d'étudier les tissus au niveau moléculaire, et sa capacité d'étudier les variations chimiques entre l'état physiologique et pathologique, cette technique a mis en évidence plusieurs marqueurs spectraux des vaisseaux sanguins. Un plus grand nombre d'échantillons et une amélioration des techniques de traitement de données spectrales permettront ensuite de valider cette méthodologie. Aussi, il serait approprié d'étudier d'une manière approfondie les modifications identifiées lors de cette étude comme les altérations glucidiques et lipidiques des vaisseaux liées aux facteurs angiogéniques ; ce qui pourrait mettre en place des outils thérapeutiques pour l'angiogenèse tumorale.

Le développement de cette méthodologie, pour la rendre plus avantageuse vis-à-vis d'autres techniques de diagnostic et notamment compatible avec la durée de l'acte chirurgical, necessitera la conception de logiciels experts pour une optimisation automatique de différenciation et plus de rapidité d'acquisition des images. A terme, il sera alors envisageable de l'appliquer sur d'autres types de tumeurs malignes.

Résumé

Utilisation de la spectro-imagerie IR-TF pour le développement d'une anatomo-pathologie moléculaire des tumeurs cérébrales

Les gliomes sont des tumeurs agressives de mauvais pronostic, très angiogéniques et infiltrantes ce qui rend leur exérèse particulièrement difficile. Vu les limites des techniques actuelles d'imagerie, nous avons proposé la spectro-imagerie Infrarouge à Transformée de Fourier (IRTF), d'une résolution spatiale de 6 µm, pour apporter une information moléculaire à l'examen histologique actuel des gliomes. Nos travaux ont été fondés sur la recherche de paramètres moléculaires des vaisseaux sanguins, notamment sur la base des contenus de leur membrane basale. Celle-ci subit des altérations dûes au stress angiogénique tumoral. Nous avons mis en évidence des altérations de la structure secondaire des protéines (tels les collagènes) des vaisseaux sanguins au cours de la croissance de la tumeur. Nous avons aussi évalué les modifications des chaines d'acides gras des phospholipides membranaires, qui révélent un degré d'insaturation plus important pour les vaisseaux tumoraux. Ensuite, sur un modèle de gliome murin, nous avons établi une méthode efficace de classification des capillaires sanguins sur la base d'absorptions de leurs contenus glucidiques et lipidiques, permettant de discriminer totalement les capillaires sains et tumoraux. La combinaison de ces paramètres a été mise à profit pour assurer une histopathologie moléculaire des gliomes humains. Nos résultats ont démontré qu'il est possible de différencier entre la vasculature saine et tumorale sur ces gliomes humains, ce qui permet une bonne délimitation des zones tissulaires correspondantes. Cette technique pourrait devenir un outil analytique fiable, rapide d'une durée compatible avec la chirurgie et donc très utile pour les neurochirurgiens.

Mots Clés : Imagerie IRTF, Gliomes, Angiogenèse, Marqueurs moléculaires, Classification

Usage of FT-IR spectro-imaging for the development of a molecular anatomo-pathology of cerebral tumors

Malignant gliomas are very aggressive tumors with poor prognosis, highly angiogenic and invasive into the surrounding brain parenchyma, making their resection very difficult. Regarding the limits of current imaging techniques, we have proposed Fourier Transform Infrared (FTIR) spectro-imaging, with a spatial resolution of 6 µm, to provide molecular information for the histological examination of gliomas. Our work was based on the research of molecular parameters of blood vessels, notably on the basis of the contents of their basement membrane, which undergoes changes due to tumor angiogenic stress. We have identified alterations of the secondary structure of proteins (such as collagen) in blood vessels during tumor growth. We have also assessed the changes in fatty acyl chains of membrane phospholipids, which revealed a higher unsaturation level in tumor vessels. Then, on a murine glioma model, we have established an efficient method of blood vessels classification based on their carbohydrates and fats contents, allowing the differentiation between healthy and tumor blood vessels. The combination of these parameters was used to provide a molecular histopathology for the study of human gliomas. Our results have demonstrated the feasibility of differentiating between healthy and tumor vasculature in these human gliomas, which help delimitating areas of corresponding tissue. This technique could become a reliable and fast analytical tool, with duration compatible with the surgery and thus very useful for neurosurgeons.

Keywords : FTIR Imaging, Gliomas, Angiogenesis, Molecular markers, Classification

Katia WEHBE

Utilisation de la spectro-imagerie IR-TF pour le développement d'une anatomo-pathologie moléculaire des tumeurs cérébrales

Les gliomes sont des tumeurs agressives de mauvais pronostic, très angiogéniques et infiltrantes ce qui rend leur exérèse particulièrement difficile. Vu les limites des techniques actuelles d'imagerie, nous avons proposé la spectro-imagerie Infrarouge à Transformée de Fourier (IRTF), d'une résolution spatiale de 6 µm, pour apporter une information moléculaire à l'examen histologique actuel des gliomes. Nos travaux ont été fondés sur la recherche de paramètres moléculaires des vaisseaux sanguins, notamment sur la base des contenus de leur membrane basale. Celle-ci subit des altérations dûes au stress angiogénique tumoral. Nous avons mis en évidence des altérations de la structure secondaire des protéines (tels les collagènes) des vaisseaux sanguins au cours de la croissance de la tumeur. Nous avons aussi évalué les modifications des chaines d'acides gras des phospholipides membranaires, qui révélent un degré d'insaturation plus important pour les vaisseaux tumoraux. Ensuite, sur un modèle de gliome murin, nous avons établi une méthode efficace de classification des capillaires sanguins sur la base d'absorptions de leurs contenus glucidiques et lipidiques, permettant de discriminer totalement les capillaires sains et tumoraux. La combinaison de ces paramètres a été mise à profit pour assurer une histopathologie moléculaire des gliomes humains. Nos résultats ont démontré qu'il est possible de différencier entre la vasculature saine et tumorale sur ces gliomes humains, ce qui permet une bonne délimitation des zones tissulaires correspondantes. Cette technique pourrait devenir un outil analytique fiable, rapide d'une durée compatible avec la chirurgie et donc très utile pour les neurochirurgiens.

Mots Clés : Imagerie IRTF, Gliomes, Angiogenèse, Marqueurs moléculaires, Classification

Katia WEHBE

Usage of FT-IR spectro-imaging for the development of a molecular anatomo-pathology of cerebral tumors

Malignant gliomas are very aggressive tumors with poor prognosis, highly angiogenic and invasive into the surrounding brain parenchyma, making their resection very difficult. Regarding the limits of current imaging techniques, we have proposed Fourier Transform Infrared (FTIR) spectro-imaging, with a spatial resolution of 6 µm, to provide molecular information for the histological examination of gliomas. Our work was based on the research of molecular parameters of blood vessels, notably on the basis of the contents of their basement membrane, which undergoes changes due to tumor angiogenic stress. We have identified alterations of the secondary structure of proteins (such as collagen) in blood vessels during tumor growth. We have also assessed the changes in fatty acyl chains of membrane phospholipids, which revealed a higher unsaturation level in tumor vessels. Then, on a murine glioma model, we have established an efficient method of blood vessels classification based on their carbohydrates and fats contents, allowing the differentiation between healthy and tumor blood vessels. The combination of these parameters was used to provide a molecular histopathology for the study of human gliomas. Our results have demonstrated the feasibility of differentiating between healthy and tumor vasculature in these human gliomas, which help delimitating areas of corresponding tissue. This technique could become a reliable and fast analytical tool, with duration compatible with the surgery and thus very useful for neurosurgeons.

Keywords : FTIR Imaging, Gliomas, Angiogenesis, Molecular markers, Classification